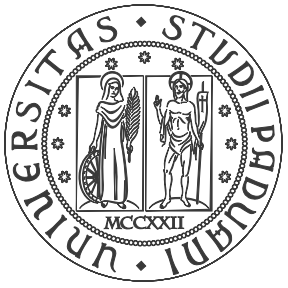

UNIVERSITÀ
DEGLI STUDI
DI PADOVA

UNIVERSITÀ DEGLI STUDI DI PADOVA

Dipartimento di Ingegneria Industriale

Scuola di Dottorato di Ricerca in Ingegneria Industriale
Indirizzo in Ingegneria Elettrotecnica
Ciclo XXXI

Disturbance Suppression in PMSM Drives

Physical Investigation, Algorithm Design and Implementation

Direttore della Scuola:
Ch.mo Prof. Paolo Colombo

Coordinatore d'Indirizzo:
Ch.mo Prof. Roberto Turri

Supervisore:
Ch.mo Prof. Silverio Bolognani

Dottorando: Ing. Milo De Soricellis

30 Settembre 2018

Contents

Acknowledgments

I would like to express my best gratitude to Prof. Silverio Bolognani, direct supervisor of my work, who, regardless the topic of my research, was always open to engage theoretical discussions, bringing delightful explanations and ideas on complicated technical details.

I am also very grateful to have worked with Mosè, technician of the Electric Drive Laboratory of Padova, who was always ready to explain complex phenomenon in simple and practical concepts, easy to visualize and remember.

Many thanks go also to the supporters and contacts I had through my experience at Robert Bosch GmbH, in particular to Holger Rapp, who guided me on the right path during the early stage of my research and helped me to develop methodologies for tackling systematically engineering problems. I express my gratitude also to Maximilian Manderla and Florian Malchow, for being enthusiastic researchers always ready to engage discussions and open to support new ideas.
Further, I would especially like to thank Henning Hansen for his precious technical hints on hardware problems.
I thank Thomas Boeker for his availability in providing me what I needed to complete this voyage and again, David, Dominik, Philipp for their friendship and support.

I am immensely grateful to my family for believing in me and for their support, encouragement on my decisions and for allowing me to complete the study with Ph.D. course.
Lastly, but definitely not the least, I like to express my greatest love to my girlfriend, who tooks the most difficult and important decision of following me in this life-through experience.

Padova, 30 September 2018 Milo De Soricellis

As far as the laws of mathematics
refer to reality, they are not certain,
and as far as they are certain,
they do not refer to reality.

A. EINSTEIN

Preface

This thesis is submitted to the University of Padova, Department of Industrial Engineering, Italy, as partial fulfillment of the requirements for the degree of Doctor of Philosophy (Ph.D.) in Electrical Engineering. The research carried out during the 3-years period of this Ph.D school is summarized in this thesis.

Background

Nowadays the shift in the paradigm of our transportation systems from pure combustion engine to hybrid and always more electrical traction systems is bringing new challenges in the field of electrical machine drives, in fact due to the race for designing extremely efficient electrical power-trains, different challenging issues into the research are arising.
Permanent magnet synchronous machines (PMSMs) have been used in many applications due to their outstanding advantages such as high torque/power density, high efficiency, light weight and good reliability. These machines, together with new winding manufacture technologies acquired interest from industries especially for traction application, since with their compact design can fit extremely well in an integrated hybrid or full electrical power-train.
Therefore, PMSMs play an important role in this context where high power density and peak torque are required. However pushing these kind of motors to their physical limits, often leads to cope with undesired effects, for example in order to increase the power density per unit volume the exhibition of harmonic content in the air-gap flux distribution waveform becomes quiet relevant and so an additional disturbance in the induced voltage and torque. High machine ripple, from the other side, reduces the overall performances of the machine, in fact it leads to the production of NVH[1] emissions as well as higher losses, which obviously cannot be completely managed at the design stage.
Although, accepted practical methods for electrical drives control are available, the opportunity of integrating new features in the industrial softwares, such as the active vibration reduction, motivates the research for more advanced control functionalities. Further, the latter is also enabled by the continuos development of the industrial hard-

[1] Noise, Vibration, Harshness

ware in terms of computational performances, which directly contributes to the relevance and the growth of embedded control softwares at a fast pace. In this context the investigation and the design of effective compensation methods for harmonics as well as noise is of great significance.
The classical control of a PMSM is composed of a simple field-oriented PI structure which ensures the correct tracking of the reference nominal speed and torque. However it is rather challenging for this kind of controllers to achieve adequate harmonic disturbance rejection.
In general the opportunities for the software correction of undesired motor harmonics belongs to two categories: iterative feed-back methods, in which the disturbance is not directly gathered through sensors, but rather indirectly observed and compensated through the measurement of other magnitudes and feed-forward methods for which the disturbance is known in advance and a compensating action can be predetermined.
Although, the methodologies for the active compensation of undesired disturbances are not really spread in the field of drive applications for the industrial sector, there is an established number of research scores related to the field of the acoustic noise cancellation. Least mean square algorithms and adaptive notch filters are commonly used for suppressing broad-band noise. Furthermore, quiet efficient methods based on the knowledge of the system's frequency response are used for the adaptive narrow-band sinusoidal disturbance suppression.
Inspired from the techniques present in literature in different branches, the aim of this PhD thesis is the development, simulation and application of advanced control methods for the reduction of constant and periodic disturbances present in PMSM and their application to electrical drives in particular.
The final goal is to suggest affordable and reliable methodologies, which can be ready to use in pre-existing controllers and safe enough to be deployed on real-industrial drives.

Abstract

The work of this Ph.D. focuses on the investigation of advanced control algorithms for the control of constant and periodic disturbances in Permanent Magnet Synchronous Machines (PMSMs), with the discussion of different methods for improving their negative influence on the machine current and the torque produced at the shaft.

The discussion of the disturbances from a control perspective starts with the study of the parameter uncertainties effect on the dynamical performances of the current control and after the detailed analysis in the frequency domain, simple methods for improving the state-of-art decoupling network are given and validated on the test-bench. Thanks to the feature of the introduced estimator, the transient behavior of the proposed strategy results in a consistent fast and precise performance. The control scheme allows to avoid the implementation of anti-windup mechanisms in the current control, making the overall controller less sensitive to parameter mismatch. Further, due to the low computational burden, the algorithm is suitable for low cost hardware.

Subsequently, the more complex issue of periodic disturbances has been deeply investigated. The theoretical model proposed is validated by comparing the real measured torque with an estimation based on the recovered disturbance affecting the observed voltages and currents. The results are clearly acceptable and further, the experimental

validation stresses out the fact that few terms have a predominant role in producing the harmonic disturbances, compared to the others. This consideration lets develop two strategies for suppressing the different harmonic orders present in the machine torque at low-speed operation. One strategy relies on on-line adaptive policies, where the estimated information is passed through a sequence of optimization algorithms with different objectives. In this context, hints on the guaranteed stability are also provided in order to confirm the practical feasibility of the algorithm. The other strategy is based on the off-line generation of some pre-determined functions, limiting the on-line burden to the computation of look-up tables. Both methods brought satisfactory results during the experimental validation, confirming the validity of our approximations made on the original complex model.

Although the hardware testbed setup limited the opportunity to validate the methodologies at low speed, this represents a realistic scenario, in fact at higher speed the artificial injection of harmonics within the machine current becomes challenging due to the high electrical rotational speed and it brings more negative effects, in terms of losses and audible noise than benefits on the shaft stress, in fact, the machine inertia acts as a natural filter for the high frequencies harmonics.

In summary, it can be said that the research work on advanced control algorithms for the disturbance suppression in PMSM drives has produced affordable and reliable methodologies, which can be of practical implementation for various industrial drives.

Sommario

Il lavoro di questo dottorato verte sullo studio di algoritmi di controllo avanzati per la riduzione dell'impatto negativo sia delle incertezze parameriche di sistema, che di disturbi armonici, nelle macchine elettriche sincrone a magneti permanenti. In particolare, l'obbiettivo si traduce nel miglioramento della qualitá dei segnali di corrente e di coppia prodotta all'albero.

La discussione inizia con l'analisi dell'impatto dei disturbi, quali la saturazione magnetica e le variazioni di temperatura, sulla dinamica di corrente e a seguito di uno studio delle funzioni di trasferimento del sistema nel dominio della frequenza, vengono proposti e validati sperimentalmente alcuni metodi per migliorare l'anello di disaccoppiamento degli assi del motore in riferimento rotorico. Grazie alle caratteristiche positive dello stimatore introdotto, la dinamica di corrente viene migliorata sia in precisione che velocitá. Inoltre, lo schema di controllo proposto permette di eliminare il ricorso al meccanismo di anti-windup dell'integratore sull'anello di corrente principale, rendendo il complessivo schema meno sensibile alle variazioni parametriche lente, come la saturazione magnetica e la sensibilitá alla temperatura. Infine, la strategia di controllo proposta risulta di facile implementazione anche su hardware dotati di risorse contenute.

Successivamente, viene approfondito il problema dei disturbi di natura periodica. Il modello analitico proposto e dettagliato nella parte introduttiva della tesi, viene validato sperimentalmente confrontando misure di coppia reali con dei segnali ricostruiti digitalmente tramite la stima del disturbo armonico presente sulla tensione e corrente di macchina. I risultati si dimostrano validi ed inoltre, permettono di dedurre che

alcuni termini sono predominanti rispetto ad altri nella produzione della componente di disturbo di coppia. Questa considerazione ha permesso di sviluppare due strategie differenti atte alla soppressione di tali armoniche presenti nella coppia.

La prima metodologia si basa sull'utilizzo di algoritmi adattativi in tempo reale, con i quali, la componente di disturbo di coppia stimata viene iterativamente minimizzata attraverso una serie di funzioni che generano rispettivamente i profili di corrente e tensione necessari per ridurre la grandezza armonica stimata. Nel proporre questi algoritmi, viene anche argomentata la stabilitá, analizzando come i parametri opzionali di design debbano essere scelti, affinché sia garantita la convergenza asintotica nel tempo.

La seconda strategia, invece, a differenza della prima, basa i suoi presupposti sulla generazione off-line di specifici profili di corrente e tensione, attraverso l'informazione della tensione indotta a vuoto dalla macchina. Questo permette di ridurre lo sforzo computazionale in tempo reale alla sola valutazione di alcune look-up tables, rendendo l'algoritmo molto efficiente dal punto di vista dell'utilizzo delle risorse hardware.

Entrambi gli schemi proposti sono validati sperimentalmente e attraverso il loro confronto si riesce a visualizzare come, partendo da presupposti diversi, entrambi portino alla medesima soluzione finale, che attua la soppressione armonica desiderata. Inoltre, benché le sperimentazioni vengono proposte a velocitá di rotazione ridotte, si ritiene che questo sia uno scenario realistico di funzionamento, infatti alle alte velocitá l'inerzia del motore tende a filtrare eventuali vibrazioni di coppia presenti all'albero, rendendo non necessaria l'iniezione armonica per la compensazione.

In conclusione, si puó affermare che questo lavoro di ricerca sull'analisi di algoritmi di controllo avanzati per la soppressione dei disturbi nei drive sincroni a magneti permanenti, ha prodotto degli algoritmi di controllo affidabili, alcuni dei quali possono essere facilmente implementati all'interno di uno schema di controllo per azionamenti industriali di varia tipologia.

Outline of the thesis

Hereafter, the contents of each Chapter of the thesis are briefly described:

Chapter 1 In the first chapter the Permanent Magnet Synchronous Machine is introduced and theoretical foundation on its operation are given. Model equations are developed starting from ideal consideration and focusing later on physical details of the non ideal behavior of these electrical machines, in particular the harmonics and their influence. The latter will constitute the core problem focus of this research.

Chapter 2 This part introduces the concept of observer and discusses different variations of the classical linear current controllers of a PMSM, in order to improve the decoupling against parameter uncertainties and produce a fast and precise tracking control.

Chapter 3 The last chapter is the core section of the thesis and is devoted on the analysis of the harmonic disturbances inside the machine. First a general discussion on the topic of periodic disturbances is provided and after a literature review,

methods for the active harmonic cancellation are proposed and investigated experimentally. Different approaches are proposed, enabling either complex on-line estimation techniques and more simpler model-based considerations for finely shaping the machine voltage and currents.

List of publications

Several parts of this Ph.D. thesis have been presented by the author during his Ph.D. course in international conferences and journals. Hereafter the publications are listed in a chronological order.

- **De Soricellis M.** , Da Ru' D. and Bolognani S., " *A robust current control based on proportional-integral observers for permanent magnet synchronous machines*". In IEEE Energy Conversion Congress and Exposition (ECCE), Milwaukee, WI, 18-22 Sep, 2016, p. 1-8, DOI: 10.1109/ECCE.2016.7854768.
- **De Soricellis M.** , Da Ru' D. and Bolognani S., " *Real-time disturbance compensation algorithm for the current control of PMSM drives*". In IEEE Energy Conversion Congress and Exposition (ECCE), Cincinnati, OH, 1-5 Oct, 2017, p. 3987-3986, DOI: 10.1109/ECCE.2017.8096697.
- **De Soricellis M.** , Da Ru' D. and Bolognani S., " *A Robust Current Control Based on Proportional-Integral Observers for Permanent Magnet Synchronous Machines*". In IEEE Transactions on Industry Applications, 2018, Volume 54 Issue 2 p. 1437-1447, DOI: 10.1109/TIA.2017.2772171.
- **De Soricellis M.** , Rapp H., " *Current and Voltage Shaping Method via Modified d-q Transformation for the Torque Ripple Compensation in PMSMs* ". In Power Electronics, Machines and Drives (PEMD), Liverpool, UK, 17-19 Apr, 2018.
- **De Soricellis M.** , Rapp H., " *Current and Voltage Shaping Method via Modified d-q Transformation for the Torque Ripple Compensation in PMSMs* ". In IET Power Electronics., DOI: 10.1049/iet-pel.2018.5585
- Toso F., **De Soricellis M.** , Bolognani S., " *Simple and Robust Model Predictive Control of a PMSM with Moving Horizon Estimator for Disturbance Compensation* ". In Power Electronics, Machines and Drives (PEMD), Liverpool, UK, 17-19 Apr, 2018.
- Toso F., **De Soricellis M.**, Preindl M., Bolognani S., " *Moving Horizon Estimator of PMSM Nonlinearities* ". In the 44th Annual Conference of the IEEE Industrial Electronics Society (IECON), Washington DC, USA, 21-23 Oct. 2018.

Chapter 1

Electrical drive

The fundamental components governing an electrical drive are presented. The synchronous electrical machine working principles are reported. The basic transformations from stationary to rotating reference frame and vice versa of a three-phase system of quantities are defined. A compact state-space description of the motor dynamical equation is derived and since modern control is almost exclusively implemented on sampled digital hardware, the systems are transformed into discrete time. Finally, in order to introduce the core of the thesis a more general and extended mathematical model of the machine is proposed accounting for the inherited disturbances arising in the real manufactured machines.

1.1. Permanent Magnet Synchronous Machines

PERMANENT magnet synchronous machines are AC machines with 3-phase stator windings usually star-connected and displaced $\frac{2}{3}\pi$ electrical radiants in space. The stator windings consist of individual coils connected and wounded in different slots as to approximate a sinusoidal distribution of the ideal PMSM. This configuration can be repeated p times around the circumference, where $z_p = \frac{p}{2}$ indicates the number of pole pairs. The stator configuration is shown in Fig. 1.1. On the rotor side are placed

(a) Physical disposition of the coils

(b) Star connection of the 3-phase windings.

Figure 1.1: Stator configuration of a PMSM for $z_p = 1$.

the permanent magnets, matching the number of stator poles. The magnets produce a

constant magnetic action. The PMSM gained popularity with the development of high performance permanent magnets, mainly the rare-earth magnets, i.e. the Neodymium (NeFeB) and Samarium-Cobalt (SmCo) magnets. These permanent magnets allow an extremely compact design to be obtained and the resulting machines have a particularly high torque density. For the latter reasons these kind of machines are particularly suitable for traction applications, either for Plug-in-Hybrid vehicles (PHEVs) or Electric vehicles (EV). The interaction between the armature current flowing into the 3-phase stator windings and the air-gap field, produces the machine torque. To this aim the air-gap field density must be displaced in space with respect to the current distribution. An example is illustrated in Fig. 1.2 for a PMSM, where it is represented a machine with $z_p = 1$ and for simplicity only the coil of the first phase is reported.

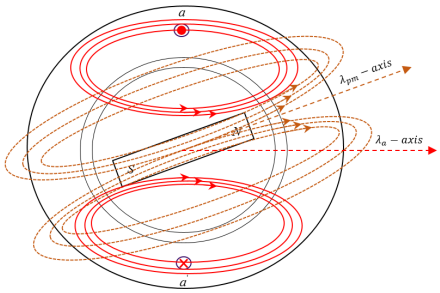

Figure 1.2: Interaction between stator and rotor fluxes in the PMSM.

Mainly the PMSM can be distinguished in two categories: the surface mounted PMSM (SPMSM) and the interior PMSM (IPMSM). The first type exhibits that the magnets attached on the surface of the rotor and since their magnetic differential permeability is considered close to the one of the air ($\mu_r \sim 1$), the air-gap is uniform along the full circumference of the machine (isotropic air-gap). At the contrary, for the IPMSM, where the magnets are inserted within the rotor iron, the resulting air-gap is not uniform (anisotropic air-gap). The magnetic reluctance seen from the stator changes according to the rotor position alternating thicker iron-paths with thinner iron-paths upon the magnet's surface. The machine is said to present a saliency and this phenomenon is exploited for producing the so-called "reluctance effect", which can add a beneficial contribution to the total torque produced by the machine, as it will be shown later in the section. The two main types of PMSM are illustrated in Fig. 1.3.

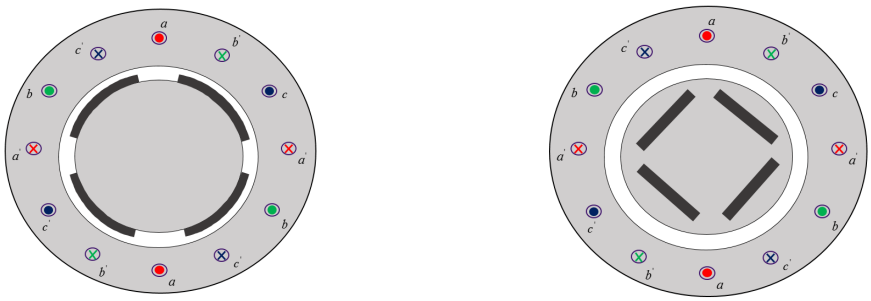

(a) Surface mounted PMSM

(b) Interior PMSM

Figure 1.3: Two different PMSMs rotor configuration for $z_p = 2$.

1.2. Mathematical Description of an Ideal PMSM

In order to give some introductory mathematical description of the electrical machine behavior, we will consider hereafter the following:

Proposition 1.2.1. *A permanent magnet synchronous machine is considered ideal in the case of a slot-less sinusoidal stator winding distribution, a linear iron behavior and a magnetic field at the air-gap assumed sinusoidally distributed.*

This allows us to derive a clean model of the machine, which will serve also as a premise for the development of our control algorithms. It is important at this stage to introduce the fundamental coordinate transformations which help us to obtain a compact description of the electrical dynamics of the machine. The overall machine coordinates systems are represented in Fig. 1.4. Looking at the complete machine

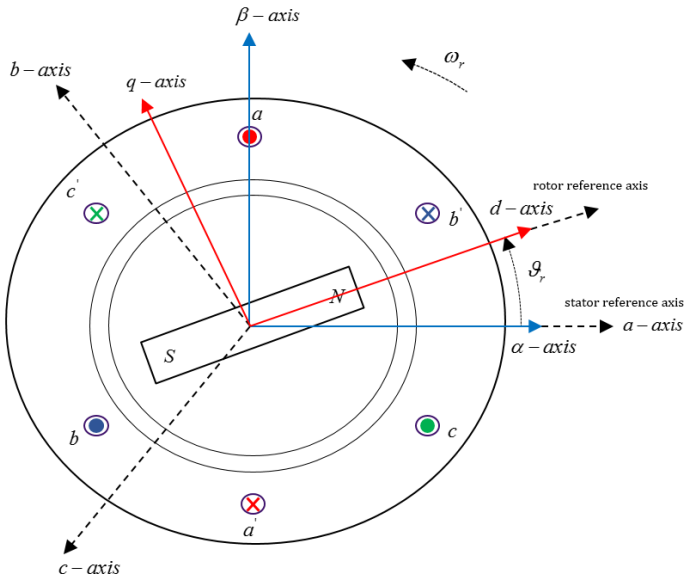

Figure 1.4: Overview of the stator and rotor coordinates systems commonly used to describe PMSM. Simplified machine with $z_p = 1$.

model with rotor and stator together, different reference axes have to be defined; respectively the rotor reference axis (d-axis), pointing in the direction of the magnet's north pole and the stator reference axis (α-axis), aligned with the peak of the air-gap magnetomotive force (MMF) distribution due to the phase a, as per Figure 1.2 .

Assumption 1.2.1. *The angle θ_r is defined by the instantaneous displacement between the rotor reference and the stator reference axis. This assumption can be generalized to machines which have a number of pole-pairs > 1, defining the electrical angle θ_e and the pole-pairs number z_p, holds the following*

$$\vartheta_e = z_p \vartheta_r \tag{1.1a}$$

$$\omega_e = z_p \omega_r \tag{1.1b}$$

where the relationship from electrical angular speed and position is given by

$$\omega_e = \frac{d}{dt}\vartheta_e \tag{1.2}$$

1.2.1. Stator Reference Frame

In general the physical three phase winding system distributed with $\frac{2}{3}\pi$ electrical radiants between each phase can be simplified with a linear transformation, leading to an equivalent two phase system $\frac{\pi}{2}$ radiants shifted. The transformation from three-phase to two-phase quantities can be written in matrix form as:

$$\begin{bmatrix} s_\alpha(t) \\ s_\beta(t) \\ s_0(t) \end{bmatrix} = \frac{2}{3} \begin{bmatrix} 1 & -\frac{1}{2} & -\frac{1}{2} \\ 0 & \frac{\sqrt{3}}{2} & -\frac{\sqrt{3}}{2} \\ \frac{1}{2} & \frac{1}{2} & \frac{1}{2} \end{bmatrix} \begin{bmatrix} s_a(t) \\ s_b(t) \\ s_c(t) \end{bmatrix} \tag{1.3}$$

where $\underline{s}_{abc}(t) = [s_a(t), s_b(t), s_c(t)]^\top \in \mathbb{R}^3$ denote a general signal in the original 3-phase system, while $\underline{s}_{\alpha\beta}(t) = [s_\alpha(t), s_\beta(t)]^\top \in \mathbb{R}^2$ are the two-phase transformed quantities in the space orthogonal phases after the transformation. The underscore symbol abbreviates the matrix notation. The choice of the constant $\frac{2}{3}$ in (1.3) is intended for maintaining unaltered the signal's magnitude across the transformation, although from a power perspective, in order to be consistent, the constant need to be added as a reciprocal factor. The homopolar component $s_0(t)$ is hereafter neglected due to the star-connection assumption of the 3 phase windings, in fact in a star-connected system holds for the current that

$$s_a(t) + s_b(t) + s_c(t) = 0 \tag{1.4}$$

while the homopolar component of the voltages has not any effect.
Therefore the usual reduced transformation can be written as

$$\begin{bmatrix} s_\alpha(t) \\ s_\beta(t) \end{bmatrix} = \frac{2}{3} \begin{bmatrix} 1 & -\frac{1}{2} & -\frac{1}{2} \\ 0 & \frac{\sqrt{3}}{2} & -\frac{\sqrt{3}}{2} \end{bmatrix} \begin{bmatrix} s_a(t) \\ s_b(t) \\ s_c(t) \end{bmatrix} \tag{1.5}$$

The inverse relationship is written as:

$$\begin{bmatrix} s_a(t) \\ s_b(t) \\ s_c(t) \end{bmatrix} = \begin{bmatrix} 1 & 0 \\ -\frac{1}{2} & \frac{\sqrt{3}}{2} \\ -\frac{1}{2} & -\frac{\sqrt{3}}{2} \end{bmatrix} \begin{bmatrix} s_\alpha(t) \\ s_\beta(t) \end{bmatrix} \tag{1.6}$$

Transformation (1.5) and (1.6) are also known as Forward and Inverse Clarke-transformations. We can compactly write them, respectively as

$$\underline{s}_{\alpha\beta}(t) = [\mathrm{T}]_{\alpha\beta} \cdot \underline{s}_{abc}(t) \tag{1.7a}$$

$$\underline{s}_{abc}(t) = [\mathrm{T}]^\top_{\alpha\beta} \cdot \underline{s}_{\alpha\beta}(t) \tag{1.7b}$$

where the underscore symbol abbreviates the matrix notation.

1.2.2. Rotor Reference Frame

The idea behind the rotor reference frame transformation is to attach the rotating position-dependent signals in the $\alpha - \beta$ coordinate, to a system which rotates with the same rotor position angle. As a consequence, the electrical equations of the machine lose their position dependency, resulting in constant quantities over time and therefore improving the tractability of the problem from a control perspective. In order to obtain this, the variables are transformed into a reference frame rotating at the electrical angular speed ω_e and with position ϑ_e. The relationship between rotor and stator reference frames is described as follow:

$$\begin{bmatrix} s_d(t) \\ s_q(t) \end{bmatrix} = \begin{bmatrix} cos(\vartheta_e) & sin(\vartheta_e) \\ -sin(\vartheta_e) & cos(\vartheta_e) \end{bmatrix} \begin{bmatrix} s_\alpha(t) \\ s_\beta(t) \end{bmatrix} \tag{1.8}$$

where s_d, s_q form the $d-q$ two-phase orthogonal components in the rotating reference frame. The elimination of position dependency from the machine components is the main advantage. The inverse rotation, to transform from the rotating to the stationary reference frame is straight-forward:

$$\begin{bmatrix} s_\alpha(t) \\ s_\beta(t) \end{bmatrix} = \begin{bmatrix} cos(\vartheta_e) & -sin(\vartheta_e) \\ sin(\vartheta_e) & cos(\vartheta_e) \end{bmatrix} \begin{bmatrix} s_d(t) \\ s_q(t) \end{bmatrix} \tag{1.9}$$

Transformation (1.8) and (1.9) are also known as Forward and Inverse Park-transformations. We can compactly write them, respectively as

$$\underline{s}_{dq}(t) = [\mathrm{T}]_{dq} \cdot \underline{s}_{\alpha\beta}(t) \tag{1.10a}$$

$$\underline{s}_{\alpha\beta}(t) = [\mathrm{T}]_{dq}^{\top} \cdot \underline{s}_{dq}(t) \tag{1.10b}$$

Proposition 1.2.2. *The Forward Park transformation is an orthogonal transformations, in fact it holds that*

$$[\mathrm{T}]_{dq}^{-1} = [\mathrm{T}]_{dq}^{\top} \tag{1.11}$$

Proof.

$$[\mathrm{T}]_{dq}^{-1} = \frac{1}{det([\mathrm{T}]_{dq})} \cdot \begin{bmatrix} cos(\vartheta_e) & -sin(\vartheta_e) \\ sin(\vartheta_e) & cos(\vartheta_e) \end{bmatrix} \tag{1.12}$$

The determinant of matrix (1.8) is clearly equal to one, therefore (1.12) reduces to be in the same form of (1.9). □

1.2.3. Fundamental Voltage Equations

The machine sketched in Figure 1.4 can be schematically represented with an equivalent electrical phase circuit shown in Figure 1.5. The voltage presents on the terminal of each phase winding is the contribution of the resistance voltage drop due to the current flowing in the coil and the induced voltage generated by the time-varying flux linkage. The fundamental voltage equation over each stator winding, sum of the resistive voltage drop and the voltage induced from the time varying flux linkage is

$$\underline{u}_s(t) = \mathrm{R}_s \underline{i}_s(t) + \frac{d}{dt}\underline{\lambda}_s(t) \tag{1.13}$$

where $\underline{u}_s(t) = [u_a(t), u_b(t), u_c(t)]^\top$ is the vector of the terminal voltages, $\underline{i}_s(t) = [i_a(t), i_b(t), i_c(t)]^\top$ is the vector of the 3-phase currents and $\underline{\lambda}_s(t) = [\lambda_a(t), \lambda_b(t), \lambda_c(t)]'$ represent the flux linkages at the stator. The stator windings are wounded with the same number of turns so the resistance is equal in all three windings, $R_a = R_b = R_c = R$, therefore the matrix R_s becomes

$$\mathrm{R}_s = \begin{bmatrix} R & 0 & 0 \\ 0 & R & 0 \\ 0 & 0 & R \end{bmatrix} \tag{1.14}$$

The voltage induced by the time-varying flux is described by the Faraday's law of induction, which states

$$e_{coil}(t) = \frac{d}{dt}\lambda_{coil}(t) \tag{1.15}$$

where $e_{coil}(t)$ is the electromotive force and $\lambda_{coil}(t)$ is the flux linkage, that is, the amount of flux passing through the closed surface traced by the coil. Moreover, if the considered coil is composed by $N_{coil} \in \mathbb{N}$ turns of a thin wire in an uniform magnetic field with flux $\varphi_{coil}(t)$, the flux linkage is $\lambda_{coil}(t) = N_{coil}\varphi_{coil}(t)$, where $\varphi_{coil}(t)$ is the magnetic flux in the cross section of the winding.
In the case of a PMSM, the total flux linkage crossing each phase winding is a superposition of the self and mutual flux linkage produced by the current flowing in the stator coils itself and the rotor permanent magnet (magnetic) flux, that is ψ_{pm}. The winding

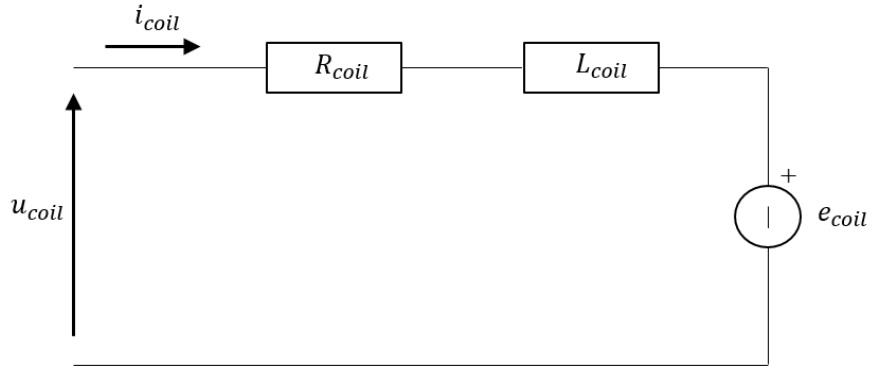

Figure 1.5: Equivalent electrical circuit for a general phase winding ($x_{ph} \in [a, b, c]$).

flux linkage can be further decomposed in its two stator and rotor contributions

$$\underline{\lambda}_s(t) = \underline{\varphi}_i(\underline{i}_s) + \underline{\psi}_{pm}(t) \tag{1.16}$$

where $\underline{\varphi}_i(\underline{i}_s) = [\varphi_i(i_a), \varphi_i(i_b), \varphi_i(i_c)]^\top$ are the fluxes produced by the respective phase currents, while $\underline{\psi}_{pm}(t) = [\psi_{pm,a}(t), \psi_{pm,b}(t), \psi_{pm,c}(t)]^\top$ expresses the rotor permanent magnet flux over the 3-phases and ϑ_e is the electrical position. In a linear and isotropic magnetic circuit, the flux linkage, contribution just of the phase currents, is defined by the product of the self, mutual inductance and the currents, hence (1.16) can be written as

$$\underline{\lambda}_s(t) = \mathrm{L}_s \underline{i}_s(t) + \underline{\psi}_{pm}(\vartheta_e) \tag{1.17}$$

with

$$\mathrm{L}_s = \begin{bmatrix} L_{aa} & M_{ab} & M_{ac} \\ M_{ba} & L_{bb} & M_{bc} \\ M_{ca} & M_{cb} & L_{cc} \end{bmatrix} \tag{1.18}$$

The inductance is the constant of proportionality that defines the relationship between the voltages induced by a time rate of change in current that produced a magnetic field. In simpler terms, inductance is the flux linkage per unit current. It must be made clear that inductance is a passive element and is purely a geometric property.
Substituting the flux expression (1.17) in (1.13), the full equation becomes

$$\underline{u}_s(t) = \mathrm{R}_s \underline{i}_s(t) + \mathrm{L}_s \frac{d}{dt} \underline{i}_s(t) + \underline{e}_s(t) \tag{1.19}$$

where $\underline{e}_s(t) = \frac{d}{dt}\underline{\psi}_{pm}(t)$ refers to the induced voltage as a reaction of the time-varying stator flux linkage produced by the rotor magnets. This component for the PMSM it is often referred as back electromotive force (BEMF).
The matrix L_s is symmetric because of the reciprocal property of the mutual inductances, moreover, it is possible to demonstrate that when two windings belonging to two different phases have the same geometrical characteristics, the mutual inductive effect behaves the same as the self inductive effect of both windings, thus for example for phase a and b holds $M_{ab} = M_{ba} = -\frac{1}{2}L_{aa}$.

Now, we should remark that in order to generalize to the IPMSM, the self and mutual inductances are not constant, but rotor position dependent; in fact, referring to Fig. 1.3b, it is possible to identify some lower reluctance path, along the magnetic field axis, and other higher reluctance path, in the correspondence of the inter-polar axis. In order to account for this phenomenon we should model the self and mutual inductive behavior of the three phases windings opportunely: L_{aa} varies periodically with twice the angular speed of the rotor, since when the rotor has rotated π radians, the same magnetic characteristics are restored, hence we can define a *minimum* value for the inductance which occurs when $\theta_e \in [0,\ \pi,\ 2\pi]$ and a *maximum* value at $\theta_e \in [\frac{\pi}{2},\ \frac{3\pi}{2},\ 2\pi]$. Consequently, extending the reasoning to all the 3 phase self and to the mutual inductances, the position dependent behavior of matrix L_s is described by the following set

of equations:

$$L_{aa}(\theta_e) = L_1 - L_2 cos(2\theta_e) \tag{1.20a}$$

$$L_{bb}(\theta_e) = L_1 - L_2 cos(2(\theta_e - \frac{2}{3}\pi)) \tag{1.20b}$$

$$L_{cc}(\theta_e) = L_1 - L_2 cos(2(\theta_e - \frac{4}{3}\pi)) \tag{1.20c}$$

$$M_{ab}(\theta_e) = -\frac{L_1}{2} - L_2 cos(2(\theta_e - \frac{\pi}{3})) \tag{1.20d}$$

$$M_{bc}(\theta_e) = -\frac{L_1}{2} - L_2 cos(2\theta_e) \tag{1.20e}$$

$$M_{ca}(\theta_e) = -\frac{L_1}{2} - L_2 cos(2(\theta_e + \frac{\pi}{3})) \tag{1.20f}$$

where L_1 is the average value of the magnetizing inductance and L_2 the amplitude of the sinusoidal varying magnetizing inductance. For completeness, the full inductance matrix is reported in (1.21).

$$\mathrm{L}_s(\theta_e) = \begin{bmatrix} L_1 - L_2 cos(2\theta_e) & -\frac{L_1}{2} - L_2 cos(2(\theta_e - \frac{\pi}{3})) & -\frac{L_1}{2} - L_2 cos(2(\theta_e + \frac{\pi}{3})) \\ -\frac{L_1}{2} - L_2 cos(2(\theta_e - \frac{\pi}{3})) & L_1 - L_2 cos(2(\theta_e - \frac{2}{3}\pi)) & -\frac{L_1}{2} - L_2 cos(2\theta_e) \\ -\frac{L_1}{2} - L_2 cos(2(\theta_e + \frac{\pi}{3})) & -\frac{L_1}{2} - L_2 cos(2\theta_e) & L_1 - L_2 cos(2(\theta_e - \frac{4}{3}\pi)) \end{bmatrix} \tag{1.21}$$

Once the angular dependency is stated, due to the high complexity of the system, we would conveniently consider to transform the voltage equations in the rotor reference frame, reducing the system's order and getting rid of the mutual coupling terms in the flux linkage equations (1.17) together with the angular dependency (1.21).

Thanks to the $d-q$ rotating transformation the inductance matrix reduces to a diagonal scalar matrix, namely L_s. In order to derive the fundamental voltage equation in the more convenient rotor reference frame, we can first express eq. (1.13) in $d-q$ coordinates as

$$\underline{u}_s(t) = \mathrm{R}_s \, [\mathrm{T}]^\top_{\alpha\beta} \, [\mathrm{T}]^\top_{dq} \, \underline{i}^s_{dq}(t) + \frac{d}{dt} \left([\mathrm{T}]^\top_{\alpha\beta} \, [\mathrm{T}]^\top_{dq} \, \underline{\lambda}^s_{dq}(t) \right) \tag{1.22}$$

where $\underline{i}^s_{dq}(t) = [i_d(t), i_q(t)]^\top$ are the $d-q$ axis stator currents and $\underline{\lambda}^s_{dq}(t) = [\lambda^s_d(t), \lambda^s_q(t)]^\top$ are the transformed fluxes.
Now multiplying both sides of (1.22) with $[\mathrm{T}]_{dq} \, [\mathrm{T}]_{\alpha\beta}$, $\underline{u}_s(t)$ can be expressed in $d-q$ coordinates as follow

$$\underline{u}^s_{dq}(t) = [\mathrm{T}]_{dq} \, [\mathrm{T}]_{\alpha\beta} \, \mathrm{R}_s \, [\mathrm{T}]^\top_{\alpha\beta} \, [\mathrm{T}]^\top_{dq} \, \underline{i}^s_{dq}(t) + [\mathrm{T}]_{dq} \, [\mathrm{T}]_{\alpha\beta} \, \frac{d}{dt} \, [\mathrm{T}]^\top_{\alpha\beta} \, [\mathrm{T}]^\top_{dq} \, \underline{\lambda}^s_{dq}(t) \tag{1.23}$$

where $\underline{u}^s_{dq}(t) = [u_d(t), u_q(t)]^\top$ are the $d-q$ axis stator voltages.
The resistance matrix R_s remains unaltered through each transformation, in fact it is a simple diagonal and scalar matrix, therefore it holds

$$\mathrm{R}_s = [\mathrm{T}]_{\alpha\beta} \, \mathrm{R}_s \, [\mathrm{T}]^\top_{\alpha\beta} = [\mathrm{T}]_{dq} \, [\mathrm{T}]_{\alpha\beta} \, \mathrm{R}_s \, [\mathrm{T}]^\top_{\alpha\beta} \, [\mathrm{T}]^\top_{dq} \tag{1.24}$$

Making use of a simple property of the derivative operator and considering the results shown in (1.24), we can develop equation (1.23) through the following steps

$$\begin{aligned}
\underline{u}^s_{dq}(t) &= \left([\mathrm{T}]_{dq}\,[\mathrm{T}]_{\alpha\beta}\,\mathrm{R}_s\,[\mathrm{T}]^\top_{\alpha\beta}\,[\mathrm{T}]^\top_{dq}\right)\underline{i}^s_{dq}(t) + [\mathrm{T}]_{dq}\,[\mathrm{T}]_{\alpha\beta}\,\frac{d}{dt}\left([\mathrm{T}]^\top_{\alpha\beta}\,[\mathrm{T}]^\top_{dq}\,\underline{\lambda}^s_{dq}(t)\right)\\
&= \mathrm{R}_s\underline{i}^s_{dq}(t) + [\mathrm{T}]_{dq}\,[\mathrm{T}]_{\alpha\beta}\,[\mathrm{T}]^\top_{\alpha\beta}\,\frac{d}{dt}\left([\mathrm{T}]^\top_{dq}\,\underline{\lambda}^s_{dq}(t)\right)\\
&= \mathrm{R}_s\underline{i}^s_{dq}(t) + [\mathrm{T}]_{dq}\,\frac{d}{dt}\left([\mathrm{T}]^\top_{dq}\,\underline{\lambda}^s_{dq}(t)\right)\\
&= \mathrm{R}_s\underline{i}^s_{dq}(t) + [\mathrm{T}]_{dq}\,[\mathrm{T}]^\top_{dq}\,\frac{d}{dt}\underline{\lambda}^s_{dq}(t) + [\mathrm{T}]_{dq}\,\frac{d}{dt}\left([\mathrm{T}]^\top_{dq}\right)\underline{\lambda}^s_{dq}(t)\\
&= \mathrm{R}_s\underline{i}^s_{dq}(t) + \frac{d}{dt}\underline{\lambda}^s_{dq}(t) + [\mathrm{T}]_{dq}\,\frac{d}{d\vartheta_e}\left([\mathrm{T}]^\top_{dq}\right)\frac{d}{dt}\theta_e\;\underline{\lambda}^s_{dq}(t)\\
&= \mathrm{R}_s\underline{i}^s_{dq}(t) + \frac{d}{dt}\underline{\lambda}^s_{dq}(t) + \omega_e\,[\mathrm{T}]_{dq}\,[\mathrm{T}]^\top_{dq}\,\mathbf{J}\underline{\lambda}^s_{dq}(t)
\end{aligned} \tag{1.25}$$

where $\mathbf{J} = \begin{bmatrix} 0 & -1 \\ 1 & 0 \end{bmatrix}$ is obtained from the derivative of the $d-q$ transformation. Since the $\alpha-\beta$ transformation is time-invariant it is threated as a constant and can be left out from the derivative operator. Re-arranging eq. (1.25), the fundamental voltage equation in the rotor reference frame can be stated as

$$\underline{u}^s_{dq}(t) = \mathrm{R}_s\underline{i}^s_{dq}(t) + \frac{d}{dt}\underline{\lambda}^s_{dq}(t) + \omega_e\mathbf{J}\underline{\lambda}^s_{dq}(t) \tag{1.26}$$

Finally, the fluxes $\underline{\lambda}^s_{dq}(t) = [\lambda_d(t), \lambda_q(t)]^\top$ need to be expressed, therefore following the same procedure of (1.23) and (1.25), it is possible to write (1.17) as

$$[\mathrm{T}]_{dq}\,[\mathrm{T}]_{\alpha\beta}\,\underline{\lambda}^s_s(t) = [\mathrm{T}]_{dq}\,[\mathrm{T}]_{\alpha\beta}\,\mathrm{L}_s(\vartheta_e)\,[\mathrm{T}]^\top_{\alpha\beta}\,[\mathrm{T}]^\top_{dq}\,\underline{i}^s_{dq}(t) + [\mathrm{T}]^\top_{\alpha\beta}\,[\mathrm{T}]^\top_{dq}\,\underline{\psi}_{pm}(t) \tag{1.27}$$

Although, the result claimed in (1.24) does not hold for the inductance matrix $\mathrm{L}_s(\theta_e)$ since it is a nonlinear and cross-coupled system, the transformation leads to relevant simplification of the original position dependent matrix (1.21). The overall matrix complexity reduction is resumed in eq. (1.28).

$$\begin{aligned}
&\boldsymbol{a}\text{–}\boldsymbol{b}\text{–}\boldsymbol{c} \quad \mathrm{L}_s(\vartheta_e)\\
&\boldsymbol{\alpha}\text{–}\boldsymbol{\beta} \quad [\mathrm{T}]_{\alpha\beta}\,\mathrm{L}_s(\vartheta_e)\,[\mathrm{T}]^\top_{\alpha\beta} = \begin{bmatrix} \frac{3}{2}(L_1 + L_2 cos(2\theta_e)) & \frac{3}{2}L_2 sin(2\theta_e) \\ \frac{3}{2}L_2 sin(2\theta_e) & \frac{3}{2}(L_1 - L_2 cos(2\theta_e)) \end{bmatrix} = \mathrm{L}^s_{\alpha\beta}\\
&\boldsymbol{d}\text{–}\boldsymbol{q} \quad [\mathrm{T}]_{dq}\,[\mathrm{T}]_{\alpha\beta}\,\mathrm{L}_s(\vartheta_e)\,[\mathrm{T}]^\top_{\alpha\beta}\,[\mathrm{T}]^\top_{dq} = \begin{bmatrix} L_{sd} & 0 \\ 0 & L_{sq} \end{bmatrix} = \mathrm{L}_s
\end{aligned} \tag{1.28}$$

where

$$L_{sd} = \frac{3}{2}(L_1 + L_2) \qquad L_{sq} = \frac{3}{2}(L_1 - L_2) \tag{1.29}$$

Aware of (1.28) and of the fact that the $d-q$ rotating transformation is for convention chosen with the d-axis pointing in the direction of the positive rotor permanent magnet

flux, equation (1.27) can be simplified obtaining

$$\underline{\lambda}^s_{dq}(t) = \mathrm{L}_s \underline{i}^s_{dq}(t) + \underline{\psi}^s_{dq} \tag{1.30}$$

where

$$\underline{\psi}^s_{dq} = [\psi_{pm} \qquad 0]^\top \tag{1.31}$$

is the contribution of the permanent magnet flux to the stator flux linkage and $\psi_{pm} \in \mathbb{R}_+$ is the constant flux produced by the PM expressed in [Vs].
The rotor reference transformation is also called "field-oriented" transformation and it is at the basis of the so-called *field-oriented control*.

Definition 1.2.1. *The field-oriented control (FOC) considers the rotating coordinate system, produced by the Park transformation, rigidly aligned with the rotating rotor permanent magnet flux vector, namely* $\underline{\psi}_{pm}(t)$.

The idea is sketched in Fig. 1.6.

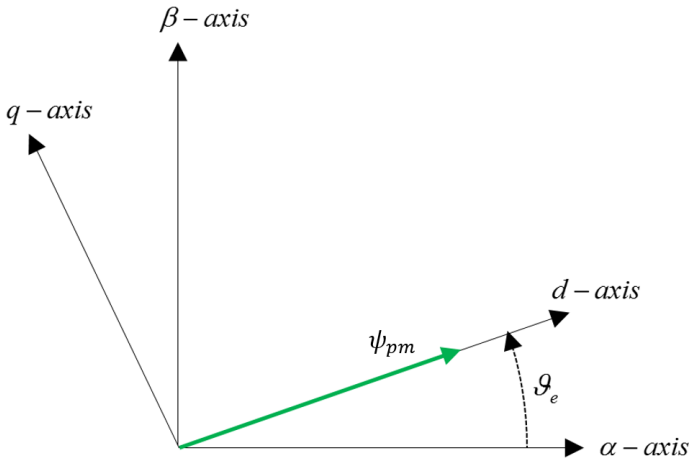

Figure 1.6: Rotor oriented coordinate transformation aligned with the PM flux.

1.2.4. Fundamental Torque Expression

Finally, in order to complete the treatise about the ideal PMSM, an expression for the electromechanical torque should be given. The reasoning will be developed hereafter introducing, from the classical theory, the concept of energy in a simplified electromechanical system.

Definition 1.2.2. *The stored energy is the energy which can be transferred to or from a conservative electromechanical coupling field via mechanical or electrical terminals. This system can be referred to a domain defined under the generalized assumptions 1.2.1 in which are present and coupled the following parts:*

- *excited single winding*
- *ferromagnetic material (e.g. iron)*
- *non-isotropic linear air-gap region*
- *rotational displacement between the electrical and mechanical part*

Further, it is assumed that the iron is selected as to have negligible hysteresis and eddy current losses and that almost all the energy of the system is stored within the air-gap region.

This system could be obtained through a model reduction of a standard IPMSM shown in Fig. 1.4, in particular imagining to keep only one single coil and pole pair, as shown in Fig 1.7.

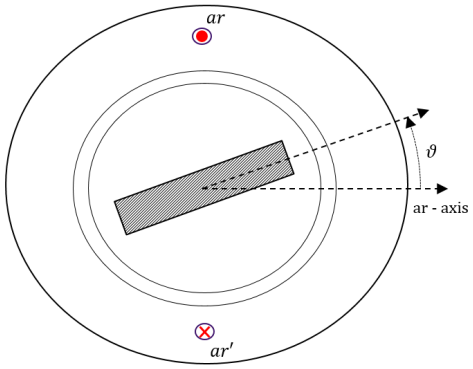

Figure 1.7: Representation of a single coil conservative electromechanical system.

Under the assumption 1.2.2 and considering for instance a given rotor position, it is shown in Fig. 1.8 the linear magnetic characteristic of the idealized system, in particular the figure shows how the energy, W_e, and coenergy, W_c, are defined, supposing that the current is i_{ar} and the flux is λ_{ar}. Therefore, from 1.8, considering a general flux and current, it holds

$$\begin{aligned} W_e + W_c &= \lambda i \\ W_e = W_c &= \frac{1}{2}\lambda i \end{aligned} \tag{1.32}$$

The λi relationship of Fig. 1.8 needs not be linear, it need only be single-valued, a property which is characteristic to a conservative or lossless field. For instance, the same relationship expressed for the magnet or the iron material has intrinsic non linearity, but we assume that the system's energy is mostly stored within the linear region (the air-gap), which highly simplify the reasoning. The rotational displacement between the PM and the winding, defined with a generic angle ϑ_r defines completely the influence of the mechanical system upon the coupling field; however, since λ and i are related, only one is needed in addition to ϑ_r in order to describe the state of the electromechanical system. Thus, choosing to develop the argument upon the current and the position, for the singly excited magnetically linear system, it holds

$$\lambda(i, \vartheta) = L(\vartheta) i \tag{1.33}$$

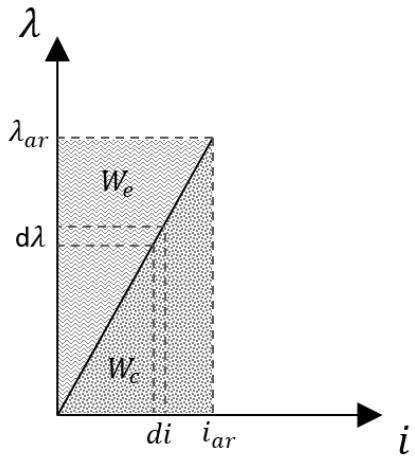

Figure 1.8: Stored energy and coenergy in a linear magnetic field of a singly excited electromagnetic system.

where $L(\theta)$ represents the winding inductance, which may vary with the position due to the non isotropic assumption.
From (1.32) and (1.33), the energy may be expressed as

$$W_e(i,\vartheta) = \frac{1}{2}L(\vartheta)i^2 \tag{1.34}$$

The field energy is a state function and the expression describing the field energy in terms of the current and position is valid regardless of the variations in the system variables.
The result in (1.34) can be proved to be valid also for an electromechanical system which presents multiple excited coils [1], for which it is possible to obtain that

$$W_e(i,\vartheta) = \int_0^{\lambda_j} \sum_{j=1}^{C} i_j d\lambda_j(i,\vartheta) \tag{1.35}$$

with C the number of coils.
This result is important and helps us to define the total stored energy in a system which as more then one electrical system, as the case of a PMSM. As an example, considering a region where there are two excited electrical coils, with the inductance matrix as

$$\mathrm{L}(\vartheta) = \begin{bmatrix} L_{11}(\vartheta) & L_{12}(\vartheta) \\ L_{21}(\vartheta) & L_{22}(\vartheta) \end{bmatrix} \tag{1.36}$$

the total stored energy can be written as

$$W_e(i,\vartheta) = \frac{1}{2}L_{11}(\vartheta)i_1^2 + L_{12}(\vartheta)i_1 i_2 + \frac{1}{2}L_{22}(\vartheta)i_2^2 \tag{1.37}$$

for which the mutual inductance L_{12} and L_{21} has been considered equal.
Now, we consider that the mechanical part can move itself and therefore, the energy is allowed to be also converted in mechanical energy. From the power conservation

principle of a conservative electrical system, in which we assume to neglect the Joule losses, it holds

$$\frac{d}{dt}W_e(i,\vartheta) = i\frac{d}{dt}\lambda(i,\vartheta) - m\frac{d}{dt}\vartheta \tag{1.38}$$

where the first term represents the time variation of the stored energy, which is equal to the difference between respectively the electrical input power and the mechanical output power, for which m indicates the electromechanical torque.
The differential energy is given by

$$dW_e(i,\vartheta) = id\lambda(i,\vartheta) - md\vartheta \tag{1.39}$$

Therefore, from (1.39) the torque is obtained from the energy by the classical result

$$m = i\frac{\partial}{\partial\vartheta}\lambda(i,\vartheta) - \frac{\partial}{\partial\vartheta}W_e(i,\vartheta) \tag{1.40}$$

where the partial derivative is obtained considering the current i as a constant.
In according with (1.32), supposing a linear region, one may also define the torque as the coenergy variation

$$m = \frac{\partial}{\partial\vartheta}W_c(i,\vartheta) \tag{1.41}$$

Keeping in mind the principles described above, they can directly be extended and applied to the IPMSM. In order to keep the calculation simple, the 3-phase system is transformed in the equivalent stationary two phase system, thus from the flux expression of (1.17), considering the anisotropic rotor and the position-dependent inductance matrix (1.21), we have

$$\underline{\lambda}^s_{\alpha\beta}(\underline{i}_{\alpha\beta},\vartheta_e) = \mathrm{L}^s_{\alpha\beta}(\vartheta_e)\underline{i}^s_{\alpha\beta}(t) + \underline{\psi}^s_{\alpha\beta}(\vartheta_e) \tag{1.42}$$

where $\underline{i}^s_{\alpha\beta}(t) = [i_\alpha(t), i_\beta(t)]^\top$ are the $\alpha-\beta$ stator currents, $\underline{\lambda}^s_{\alpha\beta} = [\lambda_\alpha, \lambda_\beta]^\top$ are the total stator fluxes, $\underline{\psi}^s_{\alpha\beta}(\vartheta_e) = [\psi_\alpha(\vartheta_e), \psi_\beta(\vartheta_e)]^\top$ are the flux linkage due to the rotor permanent magnets and $\mathrm{L}^s_{\alpha\beta}(\vartheta_e)$ is the transformed inductance matrix, namely $\mathrm{L}^s_{\alpha\beta}(\vartheta_e) = [\mathrm{T}]_{\alpha\beta}\,\mathrm{L}_s(\vartheta_e)\,[\mathrm{T}]^\top_{\alpha\beta}$.
While the coenergy can be defined as

$$W_c(\underline{i}_{\alpha\beta},\vartheta_e) = \frac{1}{2}\underline{i}^{s\top}_{\alpha\beta}(t)\mathrm{L}^s_{\alpha\beta}(\vartheta_e)\underline{i}^s_{\alpha\beta}(t) + \underline{i}^{s\top}_{\alpha\beta}\underline{\psi}^s_{\alpha\beta}(\vartheta_e) \tag{1.43}$$

Now substituting (1.42) and (1.43) in (1.40), the torque can be expressed as

$$m = z_p\left(\frac{1}{2}\underline{i}^{s\top}_{\alpha\beta}(t)\frac{d}{d\vartheta_e}\mathrm{L}_s(\vartheta_e)\underline{i}^s_{\alpha\beta}(t) + \underline{i}^{s\top}_{\alpha\beta}(t)\frac{d}{d\vartheta_e}\underline{\psi}^s_{\alpha\beta}(\vartheta_e)\right) \tag{1.44}$$

where the pole-pair factor is appeared transforming the variation of energy of the rotor position to the electrical one.
Now, similar to what have been done with the fundamental voltage and flux equation, the torque expression is projected onto the rotor reference frame, in order to obtain a much simple expression. In particular, similar to 1.22, we can write 1.44 as

$$\begin{aligned} m &= z_p\left(\frac{1}{2}\left([\mathrm{T}]^\top_{dq}\,\underline{i}^s_{dq}(t)\right)^\top\frac{d}{d\vartheta_e}\mathrm{L}^s_{\alpha\beta}(\vartheta_e)\,[\mathrm{T}]^\top_{dq}\,\underline{i}^s_{dq}(t) + \left([\mathrm{T}]^\top_{dq}\,\underline{i}^s_{dq}(t)\right)^\top\frac{d}{d\vartheta_e}\,[\mathrm{T}]^\top_{dq}\,\underline{\psi}^s_{dq}\right) \\ &= z_p\left(\frac{1}{2}\underline{i}^{s\top}_{dq}(t)\,[\mathrm{T}]_{dq}\,\frac{d}{d\vartheta_e}\mathrm{L}^s_{\alpha\beta}(\vartheta_e)\,[\mathrm{T}]^\top_{dq}\,\underline{i}^s_{dq}(t) + \underline{i}^{s\top}_{dq}(t)\,[\mathrm{T}]_{dq}\,\frac{d}{d\vartheta_e}\,[\mathrm{T}]^\top_{dq}\,\underline{\psi}^s_{dq}\right) \end{aligned} \tag{1.45}$$

Applying the transformation to the position derivative respectively for the inductance matrix and the rotor flux linkage, the following is obtained

$$\begin{aligned}[\mathrm{T}]_{dq}\frac{d}{d\vartheta_e}\mathrm{L}^s_{\alpha\beta}(\vartheta_e)\,[\mathrm{T}]^\top_{dq} &= \frac{3}{2}\begin{bmatrix}0 & L_{sd}-L_{sq}\\ L_{sd}-L_{sq} & 0\end{bmatrix}\\ [\mathrm{T}]_{dq}\frac{d}{d\vartheta_e}\,[\mathrm{T}]^\top_{dq} &= \mathbf{J} = \begin{bmatrix}0 & -1\\ 1 & 0\end{bmatrix}\end{aligned} \tag{1.46}$$

Therefore, re-arranging (1.45) with (1.46) and considering $\underline{\psi}^s_{dq}$ expressed as per (1.31), it is possible to write the final torque expression as

$$m = \frac{3}{2}z_p\left(\psi_{pm}i_q + (L_{sd}-L_{sq})i_d i_q\right) \tag{1.47}$$

Equation (1.47) expresses in the $d-q$ reference frame the electromagnetic torque produced by an ideal IPMSM, derived from the energy principle. It is possible to notice that the torque is composed by a component due to the interaction between the stator and rotor PM flux linkage and a reluctance component due to the anisotropy of the machine, which directly depends from the $d-q$ current product. In case of a SPMSM, $L_{sd} \equiv L_{sq}$, thus reluctance components becomes negligible.

1.3. Electromagnetic Non Ideal Machine Behavior

In Sec. 1.2.3 the voltage equation of a general synchronous machine has been reported. The model was presented under some assumptions of machine ideality (prop. 1.2.1), however, the spatial distribution of rotor magnets and stator windings, the rotor and stator geometry and the stator slots make the air gap flux density not being perfectly sinusoidal.
This can be intuitively deduced by figure. 1.9, where a simplified machine section has been represented. From the rotor to the stator, the magnet flux distribution is assumed to be quite uniform upon its surface, therefore the flux density distribution crossing the stator coils is far from the ideal condition of sinusoidal shape. The latter directly influence the BEMF produced on the stator side: in Fig. 1.9a, for the sack of simplicity the 3-phases are drawn in the way that the resulting winding factor is equal to one. This means that each phase coil captures the full flux linkage distribution while the rotor is moving and the resulting induced voltage appears itself not sinusoidal. Again, from the stator perspective, the anisotropy of the rotor due to the magnetic reluctance variation over the position, is not sinusoidally distributed due to the combination of non ideal rotor magnet geometry and the stator slots. Therefore the excitation flux linkage acquires space harmonics as well. As a result, harmonics appear in the air gap flux density, the flux linkage in $d-q$ axes is not constant anymore but it varies with the rotor electrical position, ϑ_e. Hence, the classic $d-q$ axis model (1.26) is no longer suitable for an accurate description of the machine behavior, instead it is valid in the case we consider the only fundamental component of a magnitude. The purpose of this section is to extend the equations of the PMSM including these non ideal effects. This allow us to understand how they propagate into the machine and which are the issues may arise in a real machine.

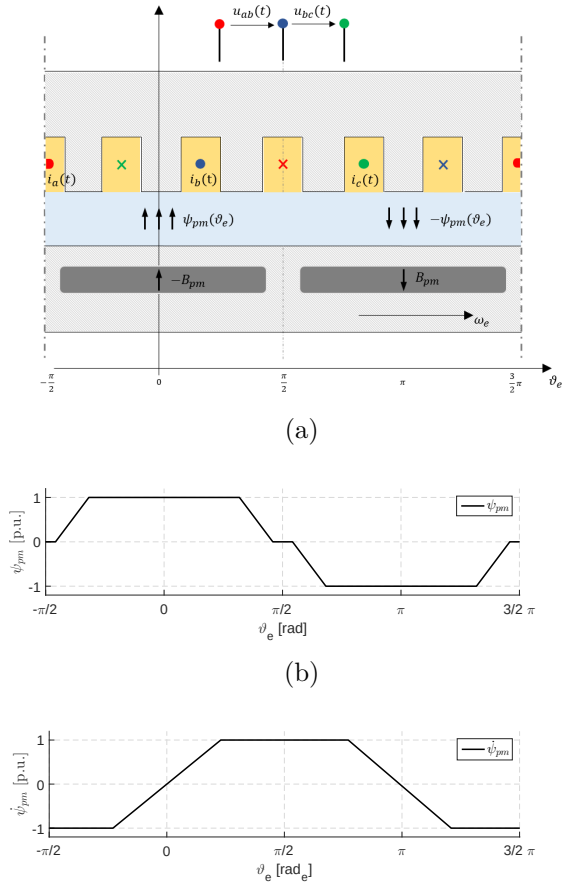

Figure 1.9: Qualitative representation of the machine non idealities: (a) pole pair linearized section of a PMSM; (b) air-gap flux density contribution of the rotor magnets, (c) electromotive force produced by the time-varying magnet flux linkage.

The extension is intended to start from (1.26) in the $d-q$ reference frame, since it helps us to reduce the complexity of the calculation and also because the control strategies developed later refer always to the $d-q$ axis.

1.3.1. Extended Fundamental Voltage Equation

Fig. 1.10 shows a general representation of a three phase permanent magnet machine transformed in the equivalent two-phase doubly fed machine. In particular, both the stator windings and the rotor magnets are represented with a two phase system.

Assumption 1.3.1. *Let the rotor magnets be represented by an equivalent DC excitation current I_{pm} in the two phase rotor system, where the fictitious coils are excited only on the conventional d-axis, defined in Fig. 1.6. Therefore the rotor current vector in the $d-q$ reference frame is $\underline{i}^r_{dq} = \begin{bmatrix} I_{pm} & 0 \end{bmatrix}^\top$.*

In what follow, the superscript and subscript r is introduced for distinguishing

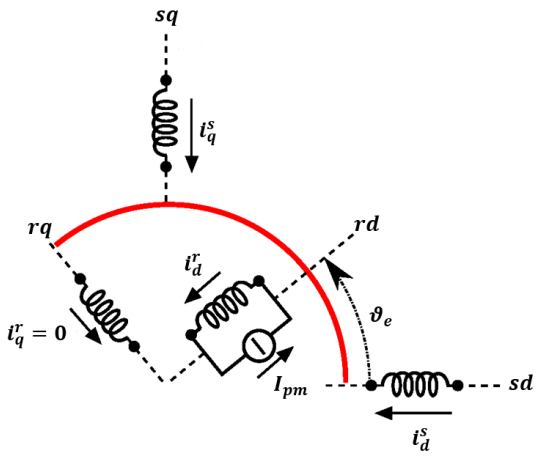

Figure 1.10: General representation of the equivalent doubly fed machine.

respectively stator and rotor magnitudes. In order to reduce overwhelming notation, the current vector $\underline{i}_{dq}^{sr}(t) = \left[\underline{i}_{dq}^{s}(t) \quad \underline{i}_{dq}^{r}\right]^{\top}$ is used to indicate stator and rotor current all together. The stator flux linkage vector, $\underline{\lambda}_{dq}^{s}(\vartheta_e, \underline{i}_{dq}^{sr}) = [\lambda_d^s(\vartheta_e, \underline{i}_{dq}^{sr}) \; \lambda_q^s(\vartheta_e, \underline{i}_{dq}^{sr})]^{\top}$, can be thought as a combination of a constant component, related to the fundamental value of the real physical quantity and a rotor position dependent one, related to the non sinusoidal spatial distribution inside the machine. The fundamental stator voltage equation (1.26) can be rewritten as follow

$$\underline{u}_{dq}^{s}(t) = \mathrm{R}\underline{i}_{dq}^{s}(t) + \frac{d}{dt}\underline{\lambda}_{dq}^{s}(\vartheta_e, \underline{i}_{dq}^{sr}) + \omega_e \mathbf{J}\underline{\lambda}_{dq}^{s}(\vartheta_e, \underline{i}_{dq}^{sr}) \tag{1.48}$$

$$\underline{\lambda}_{dq}^{s}(\vartheta_e, \underline{i}_{dq}^{sr}) = \mathrm{L}_s(\vartheta_e)\underline{i}_{dq}^{s}(t) + \mathrm{L}_{sr}(\vartheta_e)\underline{i}_{dq}^{r} \tag{1.49}$$

And for the rotor side, considering the fictitious electrical circuit representing the permanent magnets, the voltage equation can be deduced from the Faraday's law as

$$\underline{u}_{dq}^{r}(t) = \frac{d}{dt}\underline{\lambda}_{dq}^{r}(\vartheta_e, \underline{i}_{dq}^{sr}) \tag{1.50}$$

$$\underline{\lambda}_{dq}^{r}(\vartheta_e, \underline{i}_{dq}^{sr}) = \mathrm{L}_r(\vartheta_e)\underline{i}_{dq}^{r}(t) \tag{1.51}$$

where for the assumption 1.3.1, the voltage on the rotor q-axis is negligible.
Therefore, in order to account for the flux linkage harmonics we need to introduce position dependent components included in $\underline{\lambda}_{dq}^{s}(\vartheta_e, \underline{i}_{dq}^{sr})$ and $\underline{\lambda}_{dq}^{r}(\vartheta_e, \underline{i}_{dq}^{sr})$, which are hereafter integrated within the self and mutual inductance components:

$$\mathrm{L}_s(\vartheta_e) = \mathrm{L}_s + \tilde{\mathrm{L}}_s(\vartheta_e) \quad = \begin{bmatrix} L_{sd} + \tilde{L}_{sd}(\vartheta_e) & \tilde{L}_{sd,sq}(\vartheta_e) \\ \tilde{L}_{sq,sd}(\vartheta_e) & L_{sq} + \tilde{L}_{sq}(\vartheta_e) \end{bmatrix} \tag{1.52a}$$

$$\mathrm{L}_{sr}(\vartheta_e) = \mathrm{L}_{sr} + \tilde{\mathrm{L}}_{sr}(\vartheta_e) = \begin{bmatrix} L_{sd,rd} + \tilde{L}_{sd,rd}(\vartheta_e) & \tilde{L}_{sd,rq}(\vartheta_e) \\ \tilde{L}_{sq,rd}(\vartheta_e) & \tilde{L}_{sq,rq}(\vartheta_e) \end{bmatrix} \tag{1.52b}$$

$$\mathrm{L}_r(\vartheta_e) = \mathrm{L}_r + \tilde{\mathrm{L}}_r(\vartheta_e) \quad = \begin{bmatrix} L_{rd} + \tilde{L}_{rd}(\vartheta_e) & \tilde{L}_{rd,rq}(\vartheta_e) \\ \tilde{L}_{rq,rd}(\vartheta_e) & \tilde{L}_{rq}(\vartheta_e) \end{bmatrix} \tag{1.52c}$$

$\mathrm{L}_s(\vartheta_e)$, $\mathrm{L}_{sr}(\vartheta_e)$, $\mathrm{L}_r(\vartheta_e)$ stand for the inductance matrices of the stator windings (1.52a), the mutual inductance between stator and rotor windings (1.52b) and the inductance matrix of the rotor part (1.52c). Each term of (1.52) is expressed with constant and position dependent quantities, the latter stated with superscript $\sim$. Thus the model takes into account the presence of flux harmonics in the flux distribution.

Assumption 1.3.2. *Let $\tilde{\mathrm{L}}_s(\vartheta_e)$, $\tilde{\mathrm{L}}_{sr}(\vartheta_e)$, $\tilde{\mathrm{L}}_r(\vartheta_e)$ be considered periodic functions, with an average value of zero over an electrical period. Further, for the reciprocity principle, the cross-coupling between the $d-q$ stator axis is equal, namely $\tilde{L}_{sd,sq}(\vartheta_e) \equiv \tilde{L}_{sq,sd}(\vartheta_e)$. The same holds both for the stator-rotor component and for the rotor one.*

In according with that, the flux linkage component can be further defined in terms of stator and rotor contributions as

$$\underline{\lambda}^s_{dq}(\underline{i}) = \mathrm{L}_s \underline{i}^s_{dq}(t) + \mathrm{L}_{sr}\underline{i}^r_{dq}(t) \tag{1.53a}$$

$$\tilde{\underline{\lambda}}^s_{dq}(\vartheta_e, \underline{i}^{sr}_{dq}) = \tilde{\mathrm{L}}_s(\vartheta_e)\underline{i}^s_{dq}(t) + \tilde{\mathrm{L}}_{sr}(\vartheta_e)\underline{i}^r_{dq}(t) \tag{1.53b}$$

On the other side, from Fig. 1.10 the rotor fluxes are defined as

$$\underline{\lambda}^r_{dq}(\underline{i}) = \mathrm{L}_r \underline{i}^r_{dq}(t) + \mathrm{L}_{rs}\underline{i}^s_{dq}(t) \tag{1.54a}$$

$$\tilde{\underline{\lambda}}^r_{dq}(\vartheta_e, \underline{i}^{sr}_{dq}) = \tilde{\mathrm{L}}_r(\vartheta_e)\underline{i}^r_{dq}(t) + \tilde{\mathrm{L}}_{rs}\underline{i}^s_{dq}(t) \tag{1.54b}$$

where it has been defined a reciprocal mutual coupling between stator and rotor, such that $L_{rs}(\vartheta_e) = L_{sr}(\vartheta_e)^\top$.
The former (1.53), (1.54) represent the ideal and non-ideal behavior of the machine. Substituting (1.49) in (1.48) it gives

$$\underline{u}^s_{dq}(t) = \mathrm{R}\underline{i}^s_{dq}(t) + \frac{d}{dt}\underline{\lambda}^s_{dq}(\underline{i}) + \omega_e \mathbf{J}\underline{\lambda}^s_{dq}(\underline{i}) + \underline{d}^s_{dq}(\theta_e, \omega_e, \underline{i}) \tag{1.55a}$$

$$\underline{d}^s_{dq}(\theta_e, \omega_e, \underline{i}) = \underline{p}_{dq}(\vartheta_e, \underline{i}^{sr}_{dq}) + \omega_e \left(\underline{q}_{dq}(\vartheta_e, \underline{i}^{sr}_{dq}) + \mathbf{J}^\top \frac{d}{d\vartheta_e}\underline{q}_{dq}(\vartheta_e, \underline{i}^{sr}_{dq}) \right) \tag{1.55b}$$

where the term $\underline{p}_{dq}(\vartheta_e, \underline{i}^{sr}_{dq})$ and $\underline{q}_{dq}(\vartheta_e, \underline{i}^{sr}_{dq})$ are respectively defined as

$$\underline{p}_{dq}(\vartheta_e, \underline{i}^{sr}_{dq}) = \tilde{\mathrm{L}}_s(\vartheta_e)\frac{d}{dt}\underline{i}^s_{dq}(t) \tag{1.56a}$$

$$\underline{q}_{dq}(\vartheta_e, \underline{i}^{sr}_{dq}) = \mathbf{J}\tilde{\mathrm{L}}_s(\vartheta_e)\underline{i}^s_{dq}(t) + \mathbf{J}\tilde{\mathrm{L}}_{sr}(\vartheta_e)\underline{i}^r_{dq} \tag{1.56b}$$

The term $\underline{d}^s_{dq}(\vartheta_e, \omega_e, \underline{i})$ includes all the position dependent non idealities which give arise to the space harmonics in the fundamental voltage equation on the stator side (1.55). Following the model presented above, a full voltage expression can be gathered as follow. Starting from (1.48) and (1.49)

$$\begin{aligned}
\underline{u}^s_{dq}(t) &= R\underline{i}^s_{dq}(t) + \frac{d}{dt}\underline{\lambda}^s_{dq}(\vartheta_e, \underline{i}^{sr}_{dq}) + \omega_e \mathbf{J}\underline{\lambda}^s_{dq}(\vartheta_e, \underline{i}^{sr}_{dq}) \\
&= \mathrm{R}\underline{i}^s_{dq}(t) + \frac{d}{dt}\left(\mathrm{L}_s(\vartheta_e, \underline{i}^{sr}_{dq})\underline{i}^s_{dq}(t) + \mathrm{L}_{sr}(\vartheta_e, \underline{i}^{sr}_{dq})\underline{i}^r_{dq} \right) + \omega_e \mathbf{J}\mathrm{L}_s(\vartheta_e, \underline{i}^{sr}_{dq})\underline{i}^s_{dq}(t) \\
&+ \omega_e \mathbf{J}\mathrm{L}_{sr}(\vartheta_e, \underline{i}^{sr}_{dq})\underline{i}^r_{dq}
\end{aligned} \tag{1.57}$$

Now making use of the chain rule for the derivative of the products and write

$$\begin{aligned}\underline{u}^s_{dq}(t) = \mathrm{R}\underline{i}^s_{dq}(t) + \underline{i}^{s\top}_{dq}\frac{d}{dt}\mathrm{L}_s(\vartheta_e, \underline{i}^{sr}_{dq}) + \mathrm{L}_s(\vartheta_e, \underline{i}^{sr}_{dq})\frac{d}{dt}\underline{i}^s_{dq} + \underline{i}^{r\top}_{dq}\frac{d}{dt}\mathrm{L}_{sr}(\vartheta_e, \underline{i}^{sr}_{dq}) \\ + \mathrm{L}_{sr}(\vartheta_e, \underline{i}^{sr}_{dq})\frac{d}{dt}\underline{i}^r_{dq} + \omega_e\mathbf{J}\left(\mathrm{L}_s(\vartheta_e, \underline{i}^{sr}_{dq})\underline{i}^s_{dq}(t) + \mathrm{L}_{sr}(\vartheta_e, \underline{i}^{sr}_{dq})\underline{i}^r_{dq}\right)\end{aligned} \tag{1.58}$$

The time derivative of the rotor current, $\frac{d}{dt}\underline{i}^r_{dq}$, can be neglected for assumption 1.3.1, while the time derivative of the inductance matrix can be further decomposed as follow

$$\begin{aligned}\underline{u}^s_{dq}(t) = \mathrm{R}\underline{i}^s_{dq}(t) + \omega_e\underline{i}^{s\top}_{dq}\frac{d}{d\vartheta_e}\tilde{\mathrm{L}}_s(\vartheta_e, \underline{i}^{sr}_{dq}) + \mathrm{L}_s(\vartheta_e, \underline{i}^{sr}_{dq})\frac{d}{dt}\underline{i}^s_{dq} + \omega_e\underline{i}^{r\top}_{dq}\frac{d}{d\vartheta_e}\tilde{\mathrm{L}}_{sr}(\vartheta_e, \underline{i}^{sr}_{dq}) + \\ + \omega_e\mathbf{J}\left(\mathrm{L}_s(\vartheta_e, \underline{i}^{sr}_{dq})\underline{i}^s_{dq}(t) + \mathrm{L}_{sr}(\vartheta_e, \underline{i}^{sr}_{dq})\underline{i}^r_{dq}\right)\end{aligned} \tag{1.59}$$

Finally, splitting the $d-q$ components, a complete formulation of the $d-q$ axis stator voltages is written in (1.60) and (1.61).

$$\begin{aligned}u_d = Ri_d + L_{sd}\frac{d}{dt}i_d - \omega_e L_{sq}i_q + \overbrace{\tilde{L}_{sd}(\vartheta_e)\frac{d}{dt}i_d + \tilde{L}_{sd,sq}(\vartheta_e)\frac{d}{dt}i_q}^{p_d(\vartheta_e, \underline{i}^{sr}_{dq})} \\ + \omega_e[\frac{d}{d\vartheta_e}\tilde{L}_{sd}(\vartheta_e)i_d + \frac{d}{d\vartheta_e}\tilde{L}_{sq,sd}(\vartheta_e)i_q + \frac{d}{d\vartheta_e}\tilde{L}_{sd,rd}(\vartheta_e)I_{mg} \\ - \underbrace{\tilde{L}_{sd,sq}(\vartheta_e)i_d - \tilde{L}_{sq}(\vartheta_e)i_q - \tilde{L}_{sq,rd}(\vartheta_e)I_{mg}]}_{q_d(\vartheta_e, \underline{i}^{sr}_{dq})}\end{aligned} \tag{1.60}$$

$$\begin{aligned}u_q = Ri_q + L_{sq}\frac{d}{dt}i_q + \omega_e(L_{sd}i_d + L_{sd,rd}I_{mg}) + \overbrace{\tilde{L}_{sq}(\vartheta_e)\frac{d}{dt}i_q + \tilde{L}_{sq,sd}(\vartheta_e)\frac{d}{dt}i_q}^{p_q(\vartheta_e, \underline{i}^{sr}_{dq})} \\ + \omega_e[\frac{d}{d\vartheta_e}\tilde{L}_{sq}(\vartheta_e)i_q + \frac{d}{d\vartheta_e}\tilde{L}_{sd,sq}(\vartheta_e)i_d + \frac{d}{d\vartheta_e}\tilde{L}_{sq,rd}(\vartheta_e)I_{mg} \\ + \underbrace{\tilde{L}_{sq,sd}(\vartheta_e)i_q + \tilde{L}_{sd}(\vartheta_e)i_d + \tilde{L}_{sd,rd}(\vartheta_e)I_{mg}]}_{q_q(\vartheta_e, \underline{i}^{sr}_{dq})}\end{aligned} \tag{1.61}$$

1.3.2. Extended Electromagnetic Torque Expression

At the level of the electromagnetic torque produced by the machine, in this non ideal case, qualitatively it is possible to imagine the following: considering the $d-q$ reference frame, it is for definition synchronous to the fundamental angular velocity of the 3-phase stator rotating field, therefore a fundamental torque component arises as per (1.47). However, introducing position-dependent components, the $d-q$ coordinate system appears aa a stationary reference frame for the asynchronous residual harmonic components overlapped to the fundamental quantities. This translates in the fact that the total torque will be the sum of the fundamental coenergy variation projected onto the rotational reference frame and the residual coenergy variation which fluctuates relatively to the fundamental angular speed. Therefore, as an extension of (1.47), one may write the torque expression as

$$m = \frac{3}{2}z_p\underline{i}^s_{dq}(t)\mathbf{J}\lambda^s_{dq}(\vartheta_e, \underline{i}^{sr}_{dq}) + \frac{\partial}{\partial\vartheta_e}W_c(\vartheta_e, \underline{i}) \tag{1.62}$$

where $\frac{\partial}{\partial \vartheta_e} W_c(\vartheta_e, \underline{i})$ represents the coenergy variation over the electrical position assuming the $d-q$ currents constants.
The latter, in accordance with (1.52), can be further expressed as follow

$$W_c(\vartheta_e, \underline{i}) = \frac{1}{2} \underline{i}_{dq}^{s\top} \mathrm{L}_s(\vartheta_e) \underline{i}_{dq}^{s} + \underline{i}_{dq}^{s\top} \mathrm{L}_{sr}(\vartheta_e) \underline{i}_{dq}^{r} + \frac{1}{2} \underline{i}_{dq}^{r\top} \mathrm{L}_r(\vartheta_e) \underline{i}_{dq}^{r} \tag{1.63}$$

The expression (1.63) incorporates the principle of multiple excited coils acting on a single electromechanical system, remarked in (1.35).
Finally, substituting (1.63) in (1.62), the final torque expression becomes

$$\begin{aligned} m(\vartheta_e, \underline{i}_{dq}^{sr}) = \frac{3}{2} z_p \Big[& \underline{i}_{dq}^{s}(t)^\top \ \mathbf{J} \ \underline{\lambda}_{dq}^{s}(\vartheta_e, \underline{i}_{dq}^{sr}) \quad + \quad \frac{1}{2} \ \underline{i}_{dq}^{s}(t)^\top \frac{d}{d\vartheta_e} \tilde{\mathrm{L}}_s(\vartheta_e) \underline{i}_{dq}^{s}(t) \\ & + \ \underline{i}_{dq}^{s}(t)^\top \frac{d}{d\vartheta_e} \tilde{\mathrm{L}}_{sr}(\vartheta_e) \underline{i}_{dq}^{r}(t) \quad + \quad \frac{1}{2} \ \underline{i}_{dq}^{r}(t)^\top \frac{d}{d\vartheta_e} \tilde{\mathrm{L}}_r(\vartheta_e) \underline{i}_{dq}^{r}(t) \Big] \end{aligned} \tag{1.64}$$

Equation (1.64) is the most general expression which describes the electromagnetic torque produced by a synchronous machine, including all the position dependent effects which produces undesired torque fluctuation over time. The last term, namely $\underline{i}_{dq}^{r}(t)^\top \frac{d}{d\vartheta_e} \tilde{\mathrm{L}}_r(\vartheta_e) \underline{i}_{dq}^{r}(t)$ describes the so-called cogging torque effect, which is caused by the attraction of the constant rotor magnetic field to the stator iron teeth.
If instead of a doubly fed machine, it would have been considered a rotor with permanent magnets, thus considering $\psi_{pm} = L_{sd,rd} I_{pm}$, the reasoning would have been exactly the same except for the fact that the residual energy/coenergy would be expressed as

$$W_e(\underline{i}_{dq}^{s}, \psi_{pm}, \vartheta_e) = \frac{1}{2} \underline{i}_{dq}^{s\top} \tilde{\mathrm{L}}_s(\vartheta_e) \underline{i}_{dq}^{s} + \frac{d}{d\vartheta_e} W_e(\underline{i}_{dq}^{s} = 0, \psi_{pm}, \vartheta_e) \tag{1.65}$$

where in this particular case $\mathrm{L}_{sr}(\vartheta_e)$ and $\mathrm{L}_r(\vartheta_e)$ lose their meaning and the second term implicitly expresses the energy due to reluctance variation with rotational displacement, considering de-energized stator coils.
For the reason that in the equivalent doubly-fed machine all the terms appear analytically clear, we consider (1.64) as a valid general torque expression.
From (1.64), three particular cases can be defined:

1 - Constant $d-q$ axis currents

In case of constant $d-q$ axis stator currents the torque has fluctuations due to the harmonic contents of the inductances (and consequently of the stator PM flux linkage). Such harmonics are of sixth and multiple of six order [3].

2 - Ideal PMSM machine

In case of slot-less stator, sinusoidally distributed windings and rotor permanent magnets, all inductance terms are constant with the position (null derivative with respect to the position) and mutual inductance between $d-q$ windings is negligible. Therefore, the torque becomes:

$$m = \frac{3}{2} z_p \left[\psi_{pm} i_q + (L_{sd} - L_{sq}) i_d i_q\right] \tag{1.66}$$

where the permanent magnet flux is defined by $\psi_{pm} = L_{sd,rd} I_{pm}$.
Equation (1.66) applies to the formulation exposed in Sec. 1.2.3.

3 - Pure iron rotor

In case of a synchronous reluctance machine (SynRM), which means a machine without any excitation on the rotor side, $I_{pm} = 0$ applies.

For completeness, in Fig. 1.11 a typical harmonic spectrum of a 3-phase PMSM is shown. Harmonics are visible on the measured stator induced voltage and on the cur-

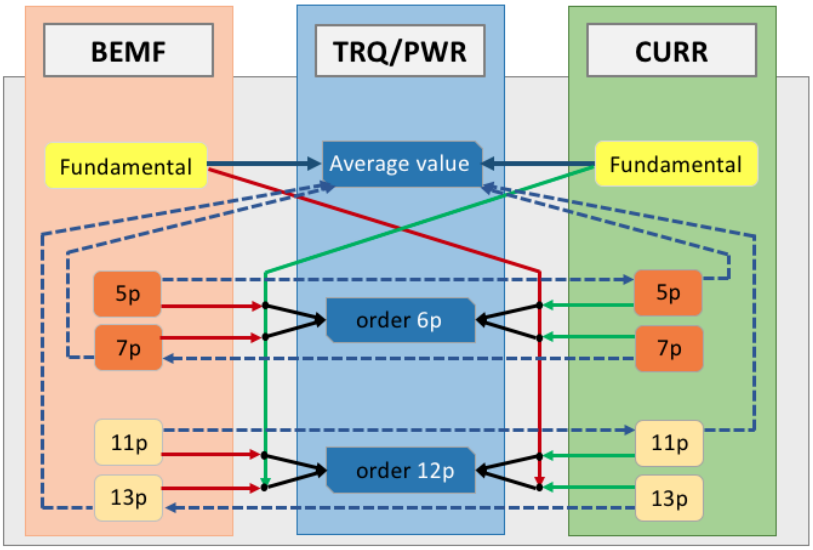

Figure 1.11: Typical harmonic spectrum of a 3 phase PMSM.

rent with a series of odd orders respectively the 5^{th}, the 7^{th}, the 11^{th} and 13^{th}, which are typically the strongest orders. The 3^{rd} order and its multiples, assuming star-connected machines, can be ignored. The current harmonics strictly depends from the

control strategies adopted for driving the current inside the machine. With standard controllers it is in general not possible to compensate these harmonics, thus power and torque produced by the machine are effectively a combination of both the induced voltage and current harmonics, which results in a series of 6^{th} and its multiplies [3].

Definition 1.3.1. *The total machine power at the terminal of a 3-phase star-connected PMSM appears respectively on a constant DC component and on multiple of* 6^{th} *order frequency components.*

The proof is avoided in fact developing analytically the power expression starting from the general product of the instantaneous 3-phase voltages and currents, the single phase power components have a set of pulsating even harmonics, namely the 2^{th}, 4^{th}, 6^{th}, 8^{th}, that once summed up for the 3-phases, the total power loses all the harmonic components but the 6^{th} and its multiples.
Finally, a practical expression for the instantaneous power in $\alpha-\beta$ or $d-q$ is as follow

$$P_e(t) = \frac{3}{2}\left(\underline{i}^{s\top}_{\alpha\beta}(t)\underline{u}^{s}_{\alpha\beta}(t)\right) = \frac{3}{2}\left(\underline{i}^{s\top}_{dq}(t)\underline{u}^{s}_{dq}(t)\right) \tag{1.67}$$

The extended equations presented in this section is certainly a complex model, which cannot be handled for controlling purposes, but it helped to give in-deep understanding of some issues arising in PMSM; therefore for our control applications throughout the dissertation, it will be considered the linear first order model presented in Sec.1.2.3, valid under proposition 1.2.1. Further, from this point forward, when the electrical magnitudes such as the current and the voltage are indicated without any superscript, they are referred exclusively to the stator.

1.4. State-Space Formulation

In this section we are going to introduce a compact way to describe the fundamental machine equations which allows us to develop several further topic along the dissertation. The most common state-space representation of a linear system is composed of n *states*, namely the values of the underlying dynamically evolving variables, with $o \leq n$ observable outputs and of a number m degrees of freedom in input, also called *control input*, which allow to influence the system's behavior. Mathematically

$$\dot{\underline{x}}(t) = \mathrm{A}(t)\underline{x}(t) + \mathrm{B}(t)\underline{u}(t) \tag{1.68a}$$
$$\underline{y}(t) = \mathrm{C}(t)\underline{x}(t) \tag{1.68b}$$

where $\underline{x}(t) \in \mathbb{R}^n$ is the state, $\underline{u}(t) \in \mathbb{R}^m$ is the control input, $\underline{y}(t) \in \mathbb{R}^o$ is the observable output, $AA(t) \in \mathbb{R}^{n\times n}$ is the state matrix, $\mathrm{B}(t) \in \mathbb{R}^{n\times m}$ is the input matrix and $\mathrm{C}(t) \in \mathbb{R}^{o\times n}$ is the output matrix.
The system (1.68) is a linear time variant (LTV) system, since the matrices which characterize the dynamical system are allowed to change in time. From the general definition of a state-space system (1.68), a fundamental property can be defined:

Definition 1.4.1. *The time-varying system* (1.68) *is called controllable to the origin on* $[t_0, t_f]$ *with* $(t_0 < t_f)$*, if given any initial state* $x_0 \in \mathbb{R}^n$ *and initial control input set* $u_0(t) : [t_0 - h_N, t_0] \to \mathbb{R}^m$*, there exists a piecewise continuous control input* $u(t)$ *such that the corresponding solution of* (1.68) *satisfies* $x(t_f) = 0$.

Further, for the subclass of linear time-invariant systems (LTI) it holds

Definition 1.4.2. *A continuous time-invariant linear state-space system is controllable if and only if*

$$rank\begin{bmatrix}\mathrm{B} & \mathrm{AB} & \mathrm{AB}^2 & \cdots & \mathrm{AB}^{n-1}\end{bmatrix} = n \tag{1.69}$$

therefore, in presence of constant system matrices, namely A, B, C, it becomes straight-forward to evaluate whether or not the system is controllable.

1.4.1. Continuous Time

For a PMSM, the machine currents (or fluxes, depending from the formulation) can be considered the states of our system, while the voltages the controllable inputs. Depending from the chosen reference frame for formulating the state-space system, the model has a different complexity, however considering the convenient formulation derived in (1.26), the continuous and linear state-space formulation can be written as follow

$$\dot{\underline{i}}_{dq}(t) = \mathrm{A}_c\underline{i}_{dq}(t) + \mathrm{B}_c\underline{u}^s_{dq}(t) + \mathrm{E}_c(t) \tag{1.70}$$

where

$$\mathrm{A}_c = \begin{bmatrix} -\frac{R_s}{L_{sd}} & \omega_e(t)\frac{L_{sq}}{L_{sd}} \\ -\omega_e(t)\frac{L_{sd}}{L_{sq}} & -\frac{R_s}{L_{sq}} \end{bmatrix}, \quad \mathrm{B}_c = \begin{bmatrix} \frac{1}{L_{sd}} & 0 \\ 0 & \frac{1}{L_{sq}} \end{bmatrix}, \quad \mathrm{E}_c = \begin{bmatrix} 0 \\ -\omega_e(t)\frac{\psi_{pm}}{L_{sq}} \end{bmatrix} \tag{1.71}$$

The state-space system (1.70) is LTV depending on the parameter $\omega_e(t)$. Moreover, the following assumption is made

Assumption 1.4.1. *The PMSM states are directly measurable through the current sensors. From* (1.68) *it holds* $x(t) \equiv y(t) \equiv \underline{i}_{dq}(t)$*, therefore* $\mathrm{C} = \mathbf{I}$*, where* $\mathbf{I}$ *is the identity matrix of dimension* $n \times n$*.*

The stability properties of the autonomous system (i.e. $\underline{u}^s_{dq}(t) = 0$) are shown as follows.

Proposition 1.4.1. *The autonomous system* (1.70) *is considered marginally stable if and only if the real part of every pole (eigenvalue) in the system's transfer-function is non-positive.*

Proof. The transfer function of the system can be obtained starting from its state-space representation through the following expression:

$$\mathrm{G}(s) = (s\mathbf{I} - \mathrm{A}_c)^{-1}\mathrm{B}_c \tag{1.72}$$

where I is a 2×2 identity matrix. The poles of $\mathrm{G}(s)$ are the uncanceled eigenvalues of A_c, as a result for a given A_c and B_c to be stable, all eigenvalues of A_c should be negative. In order to determine this, let write the characteristic equation of $(s\mathbf{I} - \mathrm{A}_c)$

$$det(s\mathbf{I} - \mathrm{A}_c) = det\begin{bmatrix} s - a_{c11} & a_{c12} \\ a_{c21} & s - a_{c22} \end{bmatrix} = (s - a_{c11})^2(s - a_{c22})^2 - a_{c12}a_{c21} \tag{1.73}$$

where $a_{c11},\ a_{c12},\ a_{c21},\ a_{c22}$ are the elements of matrix A_c. Imposing (1.73) to zero leads to

$$s_{1,2} = \frac{1}{2}\left(a_{c11} + a_{c22} \pm \sqrt{(a_{c11} - a_{c22})^2 + 4a_{c12}a_{c21}}\right) \tag{1.74}$$

We can distinguish two cases:

- the electrical speed $\omega_e = 0$, therefore $a_{c12} = a_{c21} = 0$ are obtained two solutions with a purely negative real part, since a_{c11} and a_{c22} are strictly negative.
- the electrical speed $\omega_e \neq 0$, therefore again two solutions result with a negative real part and eventually two distinct complex solutions.

In both cases we are sure that

$$\Re([s\mathbf{I} - \mathrm{A}_c]) < 0 \tag{1.75}$$

□

1.4.2. Discrete Time

Control of modern drive system is almost exclusively implemented on digital hardware. thus, the continuous-time state-space model (1.70) is transformed into discrete time. Let $T_s \in \mathbb{R}^+$ be the sampling period and $k \in \mathbb{N}^+$ identify the discrete-time instant $t = kT - s$. For simplicity, it is assumed that $\omega_e(t)$ varies slowly with respect to the sampling period.

Assumption 1.4.2. *Let T_s be sufficiently small such that $\omega_e(k) \approx \omega_e(t)$ for $t \in [kT_s, kT_s + T_s]$*

Moreover, the absolute value of $\omega_e(k)$ is limited from a design perspective of the drive, in fact the sampling theorem holds true.

Assumption 1.4.3. *Let the maximum mechanical frequency of the machine be $\leq \frac{f_s}{2}$, where $f_s = \frac{1}{T_s}$ is the sampling frequency. Therefore it holds that*

$$\omega_e \leq \frac{\pi}{T_s} \tag{1.76}$$

This assumption is necessary to be able to compute or estimate $\omega_e(k)$ correctly from the state-space systems or from a sensor. Moreover, this allows us to transform the continuous LTV system of (1.70) in a discrete linear time-invariant (LTI) system, for which, the definition 1.4.1 of controllability, can be verified; infact definition 1.4.2 for LTI systems holds true either in continuous and discrete domain.
When performing discretization, a zero order hold element is typically assumed at the input of the continuous time system. In other words, a constant input is applied for the entire sampling period.

Assumption 1.4.4. *Let $\underline{u}^s_{dq}(k) = \underline{u}^s_{dq}(t)$ for all $t \in [kT_s,\ kT_s + T_s]$*

The continuous-time state-space model (1.70) can be transformed into discrete time by exact (or zero-order-hold, ZOH) discretization (references), which yields

$$\underline{i}_{dq}(k+1) = \mathrm{A}_d \underline{i}_{dq}(k) + \mathrm{B}_d \underline{u}^s_{dq}(k) + \mathrm{E}_d(k) \tag{1.77}$$

where $\underline{i}_{dq}(k+1) = \underline{i}_{dq}(kT_s + T_s)$, $\underline{i}_{dq}(k) = \underline{i}_{dq}(kT_s)$ and $\underline{u}^s_{dq}(k) = \underline{u}^s_{dq}(kT_s)$, $\mathrm{E}_d(k) = \mathrm{E}_d(kT_s)$, which are constant over the sampling instant. The system matrices are defined as follow

$$\mathrm{A}_d = e^{\mathrm{A}_c T_s} \tag{1.78a}$$

$$\mathrm{B}_d = \left(\int_0^{Ts} e^{\mathrm{A}_c \tau} d\tau \right) \mathrm{B}_c \tag{1.78b}$$

$$\mathrm{E}_d = \left(\int_0^{Ts} e^{\mathrm{A}_c \tau} d\tau \right) \mathrm{E}_c \tag{1.78c}$$

Exact discretization preserves the stability properties of the continuous state-space system, but it is often intractable or the resulting discrete-time system is difficult to handle in practice. Approximations are commonly used to simplify the discretization process, thus the discrete matrix model (1.78 can be numerically approximated with

$$\mathrm{A}_d = \mathbf{I} + \mathrm{A}_c \left(\mathbf{I} T_s + \frac{\mathrm{A}_c T_s^2}{2!} + \frac{\mathrm{A}_c^2 T_s^3}{3!} + \cdots + \frac{\mathrm{A}_c^{h-1} T_s^h}{h!} \right) \tag{1.79a}$$

$$\mathrm{B}_d = \mathrm{B}_c \left(\mathbf{I} T_s + \frac{\mathrm{B}_c T_s^2}{2!} + \frac{\mathrm{B}_c^2 T_s^3}{3!} + \cdots + \frac{\mathrm{B}_c^{h-1} T_s^h}{h!} \right) \tag{1.79b}$$

$$\mathrm{E}_d = \mathrm{E}_c \left(\mathbf{I} T_s + \frac{\mathrm{E}_c T_s^2}{2!} + \frac{\mathrm{E}_c^2 T_s^3}{3!} + \cdots + \frac{\mathrm{E}_c^{h-1} T_s^h}{h!} \right) \tag{1.79c}$$

With the given approximation, the local truncation error diminishes as more terms are used. Using the first term is equivalent to a standard forward Euler difference.
The latter is the most widely-used approximation and it is based on the simple following consideration

$$\dot{\underline{i}}_{dq} \simeq \frac{\underline{i}_{dq}(k+1) - \underline{i}_{dq}(k)}{T_s} \tag{1.80}$$

Therefore truncating at the first term in 1.79 we can discretize (1.70) as

$$\underline{i}_{dq}(k+1) = \mathrm{A}_d \underline{i}_{dq}(k) + \mathrm{B}_d \underline{u}^s_{dq}(k) + \mathrm{E}_d(k) \tag{1.81a}$$

$$\mathrm{A}_d = \mathbf{I} + \mathrm{A}_c T_s = \begin{bmatrix} 1 - T_s \frac{R}{L_{sd}} & \omega_e(k) T_s \frac{L_{sq}}{L_{sd}} \\ -\omega_e(k) T_s \frac{L_{sd}}{L_{sq}} & 1 - T_s \frac{R}{L_{sq}} \end{bmatrix} \tag{1.81b}$$

$$\mathrm{B}_{sd} = \mathrm{B}_c T_s = \begin{bmatrix} \frac{T_s}{L_{sd}} & 0 \\ 0 & \frac{T_s}{L_{sq}} \end{bmatrix} \tag{1.81c}$$

$$\mathrm{E}_d = \mathrm{E}_c T_s = \begin{bmatrix} 0 \\ -\omega_e(k) T_s \frac{\psi_{pm}}{L_{sq}} \end{bmatrix} \tag{1.81d}$$

Even if Euler forward do not preserve the properties of the continuous time system, i.e. the discrete time system obtained via exact discretization, for its simplicity it will be exploited for the development of our work.

1.5. Power Electronics

The power module is the core element of every drive, in fact it allows the efficient transformation of DC quantities, from DC power source (e.g. vehicle battery), to AC quantities which are suitable for operating the 3-phase electrical machine connected as a load. This drive element is commonly addressed as "inverter". Further, the electronics integrated within the inverter allows to finely manipulate the voltage applied to the machine and this is done through the "modulation". In Fig. 1.12 the typical configuration of a 3-phase inverter is shown. It is composed by a DC capacitor which helps to filter high frequency noise coupled at the DC bus level, and six electronic controlled valves. The latter can be either turned on and off via a proper external signal, which allows to control in time the valves. In particular, in the figure are represented the commonly used *IGBTs* [1], but for some specific applications are also used the *MOSFET* [2]. In general, the first are preferred for high-voltage, high-current and low switching frequencies, while the second in case of low-voltage, low-current and high switching frequencies. If current flow is allowed, the valve is said to be *on*; otherwise, it is said to be *off*. The reverse conducting characteristic is achieved by adding an anti-parallel diode to the *IGBT*. The *MOSFET* has an anti-parallel diode inherit in its structure. Each AC phase is connected to both polarities of the DC link throughout transistor as it is shown in Figure 1.12. The two valves connected to the same phase, respectively the high side and the low side driver, are called the *leg* of the inverter.

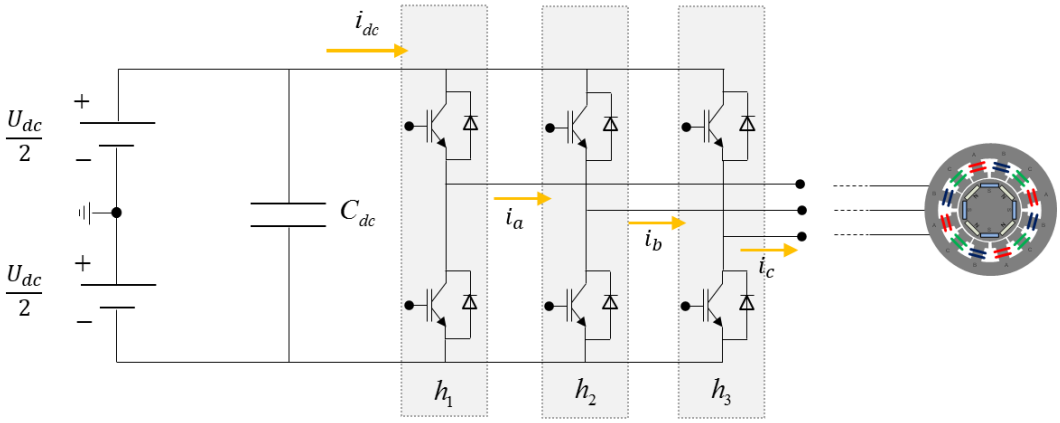

Figure 1.12: Voltage source inverter (VSI) topology.

The switching can be open and closed alternatively, in general it is avoided the simultaneous conduction of drivers belonging to the same leg, in fact this would lead to a short circuit of the DC power source. Each allowed combination of switching of the 3-phases is called *state* and in total they are 8. They are resumed in Tab. 1.1 and visually represented in Fig. 1.14. The maximum phase voltage available is equal to $\frac{2}{3}U_{dc}$.

[1] Insulated gate bipolar transistor

[2] Metal oxide semiconductor field effect transistor

1.5.1. Operation

Since the inverter can only produce square-wave voltage output at the 3-phase line, in order to properly control the machine it is necessary to introduce a modulation technique. The idea is to allows the power electronic to reproduce as accurate as possible a sinusoidal voltage. The most simple modulation method is called *Sinusoidal Pulse Width Modulation* (SPWM), which is visualized in Fig. 1.13. A duty cycle is generated by the feed-back controller, which expresses the normalized desired voltage to apply at the machine terminal. The duty cycle of each phase is compared with a triangular carrier and the switching logic is based on the follow

$$\text{if } d_i > \text{carrier, then } u_i = +\frac{U_{dc}}{2} \tag{1.82}$$

$$\text{if } d_i < \text{carrier, then } u_i = -\frac{U_{dc}}{2} \tag{1.83}$$

$$for\ i = a, b, c \tag{1.84}$$

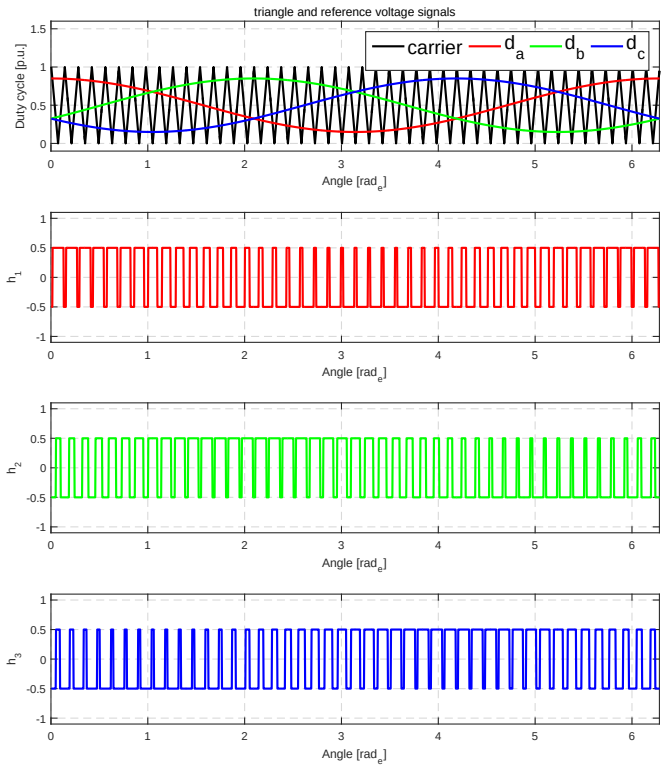

Figure 1.13: Voltage source inverter (VSI) topology.

Therefore, the width of the pulses is changed over time in order to reproduce a sinusoid. Moreover, the inverter output voltage has the following features:

- PWM frequency is the same as the frequency of the carrier
- Amplitude is controlled by the magnitude of the duty cycle

State	h_1	h_2	h_3	U_{an}	U_{bn}	U_{cn}	U_{ab}	U_{bc}	U_{ca}
s_0	0	0	0	0	0	0	0	0	0
s_1	1	0	0	$\frac{2}{3}$	$-\frac{1}{3}$	$-\frac{1}{3}$	1	0	-1
s_2	1	1	0	$\frac{1}{3}$	$\frac{1}{3}$	$-\frac{2}{3}$	0	1	-1
s_3	0	1	0	$-\frac{1}{3}$	$\frac{2}{3}$	$-\frac{1}{3}$	-1	1	0
s_4	0	1	1	$-\frac{2}{3}$	$\frac{1}{3}$	$\frac{1}{3}$	-1	0	1
s_5	0	0	1	$-\frac{1}{3}$	$-\frac{1}{3}$	$\frac{2}{3}$	0	-1	1
s_6	1	0	1	$\frac{1}{3}$	$-\frac{2}{3}$	$\frac{1}{3}$	1	-1	0
s_7	1	1	1	0	0	0	0	0	0

Table 1.1: The eight inverter voltage vectors. State 1 means that the high switching of the corresponding phase-leg is closed; state 0 means that the low switching of the corresponding phase-leg is closed.

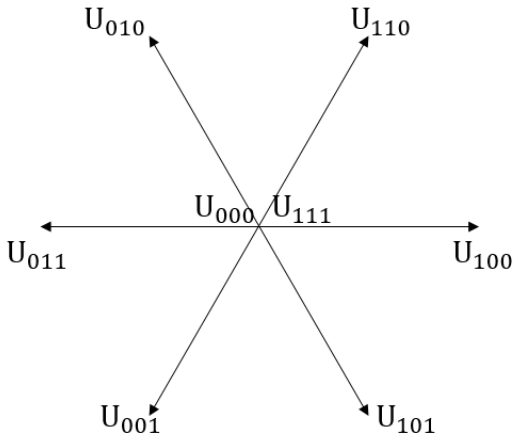

Figure 1.14: Switching state physically admissible by the considered inverter topology.

- Fundamental frequency is controlled by the frequency of the duty cycle

As a result the current flowing in the machine is shown in Fig. 1.15. Since the machine is seen as a resistive-inductive component from the power electronics, clearly it acts as a low-pass filter for the switching voltage applied on its terminal, therefore the pulses are "averaged" naturally by the machine and the current wave-form results in a sinusoid with a residual harmonic content overlapped, in particular the switching frequency of the inverter is clearly visible. With the SPWM technique it is possible to exploit the DC voltage practically till the fundamental sinusoidal voltage reaches $\frac{U_{dc}}{2}$, after that point, the power modulator saturate (it is said to go in *over-modulation*) and the voltage cannot any more be controlled linearly, thus harmonic distortion is increased. In order to overcome this limitation and enhance the exploitation of the DC bus, another popular technique has been introduces, which is referred as the *Space Vector Pulse*

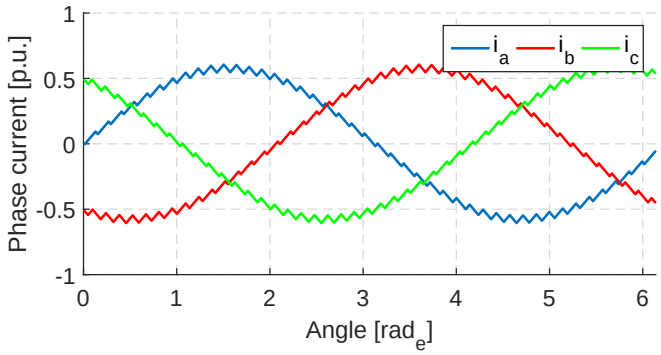

Figure 1.15: Filtered current waveform obtained connecting the power electronics to an RL load such as a PMSM.

Width Modulation (SVPWM). The objective of SVPWM technique is to approximate the reference voltage vector using the eight switching patterns. The reference vector is then synthesized using a combination of the two adjacent active switching vectors and one or both of the zero vectors. The procedure is briefly summarized in Fig. 1.16. The input of a modulator is the voltage vector $\underline{u}_{\alpha\beta}$, which is defined by its magnitude

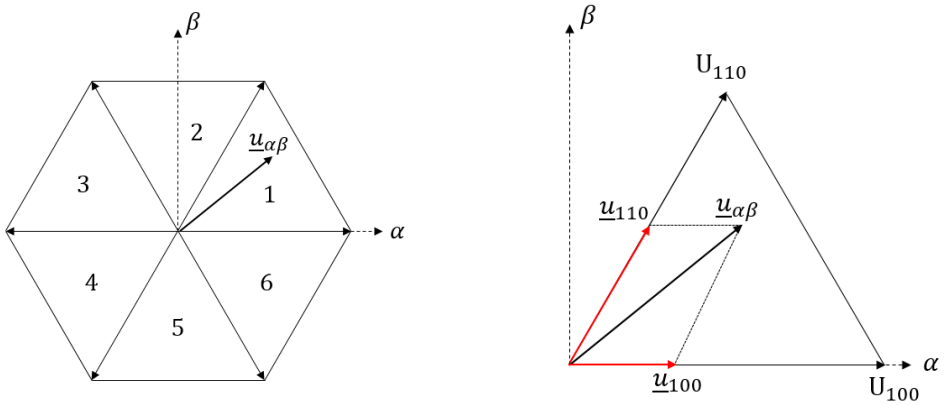

(a) Sectors

(b) Vector projections

Figure 1.16: SVPWM sectors and computation of vector duty cycles.

$\|\underline{u}_{\alpha\beta}\|$and its angle $\angle\underline{u}_{\alpha\beta}$ in polar coordinates. The vector is represented as an example in Fig. 1.16a, in the first sector. Therefore, from Fig. 1.16b it is shown that the actual commanded voltage can be obtained from a combination of the U_{100} and U_{110} and a passive vector, for example U_{000}. The components are obtained using the law of sine as shown in Figure 1.16b

$$\begin{aligned}\|\underline{u}_{100}\| &= \frac{\|\underline{u}_{\alpha\beta}\|}{\sin(2\pi/3)}\sin(\pi/3 - \angle\underline{u}_{\alpha\beta}) = \frac{2}{\sqrt{3}}\|\underline{u}_{\alpha\beta}\|\sin(\pi/3 - \angle\underline{u}_{\alpha\beta}) \\ \|\underline{u}_{110}\| &= \frac{\|\underline{u}_{\alpha\beta}\|}{\sin(2\pi/3)}\sin(\angle\underline{u}_{\alpha\beta}) = \frac{2}{\sqrt{3}}\|\underline{u}_{\alpha\beta}\|\sin(\angle\underline{u}_{\alpha\beta})\end{aligned} \tag{1.85}$$

Finally, it is necessary to calculate the ON time of the selected inverter states within the sampling period T_s, which is proportional to the calculated $\|\underline{u}_{100}\|$ and $\|\underline{u}_{110}\|$ and

yields to

$$\begin{aligned} T_{100} &= T_s \frac{3}{2U_{dc}} \|\underline{u}_{100}\| \\ T_{110} &= T_s \frac{3}{2U_{dc}} \|\underline{u}_{110}\| \end{aligned} \tag{1.86}$$

The remaining time of the entire period T_s, a passive vector is applied as

$$T_{000} = 1 - T_{100} - T_{110} \tag{1.87}$$

Note that the passive state can be also produced by T_{111} and in general this choice is made looking which of the two passive state produces less effort in being activated. Now, the complete sequence of activation time is generated and actuated to the inverter by PWM. In reality the sequence can be ordered in different way and it is not uniquely defined. In practice, the most popular technique relies on the production of a symmetric sequence, splitting the passive cycle T_{000} and applies half of it at the beginning and half at the end of the sampling period. Compared to the SPWM, the SVPWM has the feature to strech the maximum DC voltage range available from $\frac{1}{2}U_{dc}$ to $\frac{1}{\sqrt{3}}U_{dc}$, before it goes in over-modulatio. This is achieved by the third harmonic injection [4] and a clear comparison is shown in Fig. 1.17.

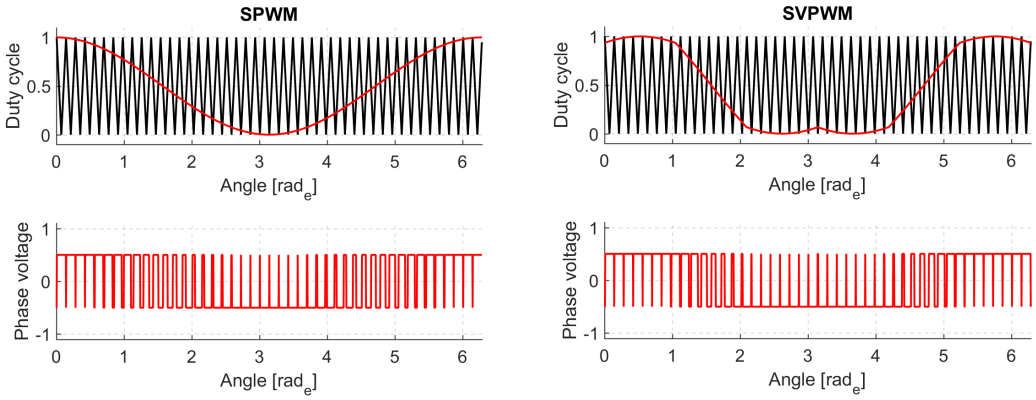

(a) $\frac{\|\underline{u}_{\alpha\beta}\|}{U_{dc}} = \frac{1}{2}$ (b) $\frac{\|\underline{u}_{\alpha\beta}\|}{U_{dc}} = \frac{1}{\sqrt{3}}$

Figure 1.17: SVPWM sectors and computation of vector duty cycles.

1.5.2. Non idealities

As far, the power converter has been introduced with its ideal behavior. However in reality since power is transmitted through an electronic device, some physical effects need to be accounted. Hereafter the principle undesired effect are described.

Voltage drop

The switching components, namely the transistors or the diode, are not ideal elements, therefore during their conduction, the power flows through them producing a voltage drop proportional to the ration between the activation voltage and the conductive resistance of the component. The IGBT or the MOSFET are composed by three element, in the case of an IGBT they are the gate (G) which allows to enable or disable the device, the collector (C), and the emittor (E), through which the power flows when the component is made conductive and a voltage u_CE appears. For the diode, instead, during the conductive phase it is considered a u_D. In function of the switching state and the direction of the current flowing, different operation are defined which are displayed in Fig. 1.18

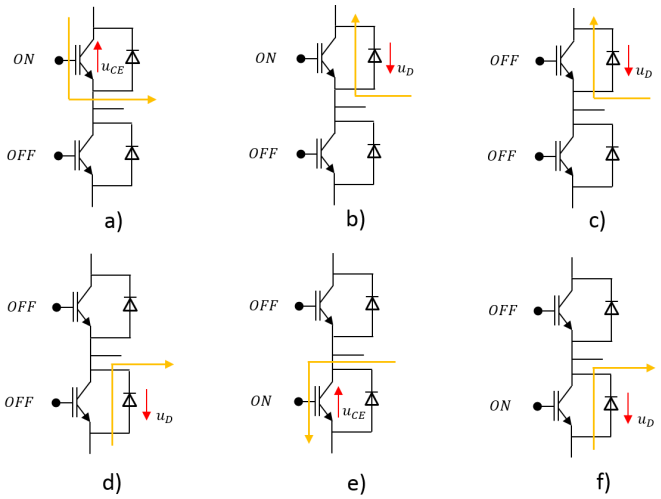

Figure 1.18: Possible instantaneous output voltages depending on the current direction and switching state, (a) $u_{ph} = 1/2U_{dc} - u_{CE}$, (b) $u_{ph} = 1/2U_{dc} + u_D$, (c) $u_{ph} = 1/2U_{dc} + u_D$, (d) $u_{ph} = -1/2U_{dc} - u_D$, (e) $u_{ph} = -1/2U_{dc} + u_{CE}$ (f) $u_{ph} = -1/2U_{dc} - u_D$.

Turn-on and turn-off time

As imaginable, it is not possible that the switching can instantaneous modify is state from conductive to non conductive or vice-versa, in fact the voltage will rise during activation and it will also extinguish during deactivation with a certain constant time. Turn-on and turn-off times of the IGBT's are the time that the switch takes to turn on or off (fully conduct or fully block the current, respectively) from when it is commanded to do so.

Interlock time

Interlock time is needed to prevent the DC link from being short circuited when the two devices of a leg of the inverter are switched. Its effects can be seen in Fig. 1.19. When the switch state of a leg changes, a delay time must be given for the switch initially on to turn off before the other switch is turned on. During that time, both switches are off, the states reflected. This delay time generates short voltage error pulses of a constant amplitude and width in the output voltage of one inverter leg, with respect to the commanded voltage value. The sign of the error pulse is the opposite of the current polarity in that leg.

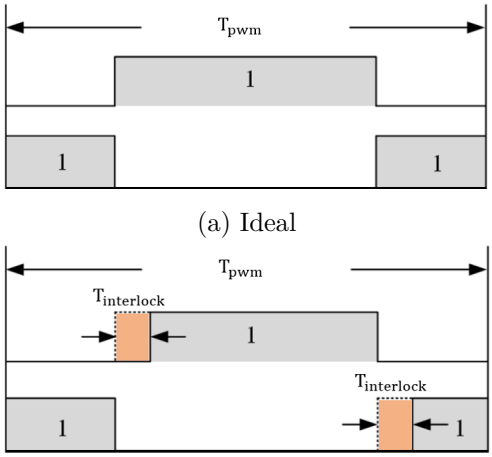

(a) Ideal

(b) Real

Figure 1.19: Switching function between upper and lower side electronic valve on the same phase-leg.

All the three described physical effects directly impact the duty cycle executed to the inverter, therefore the commanded voltage will be distorted and the current will be affected by an extra disturbance. In particular the voltage error V_ϵ applied to the machine can be described as follow

$$\begin{aligned} V_\epsilon &= \frac{1}{2}U_{dc}\frac{T_i}{Ts} + u_{CE}\frac{T_{on}-T_i}{T_s} - u_D\frac{T_{off}+T_i}{T_s} \quad \text{if } i>0 \\ V_\epsilon &= -\frac{1}{2}U_{dc}\frac{T_i}{Ts} - u_D\frac{T_{on}+T_i}{T_s} - u_{CE}\frac{T_{off}-T_i}{T_s} \quad \text{if } i<0 \end{aligned} \tag{1.88}$$

where T_i is the interlock time.

1.6. Other Sources of Uncertainty and Disturbance

The PMSM model introduced so far has been enriched with the position dependency terms arising in the non ideal flux spatial distribution within the machine. In case the effect of the spatial harmonics is neglected, the model is reduced to an ideal and linear set of equations, namely the $d-q$ voltage (1.26) and the $d-q$ flux (1.30). The latter it is not correct, in fact in general the current-flux maps are not linear due to the saturation of the iron and the quantity of flux produced per increment of current $\Delta \underline{i}_{dq}$ reduces strongly. Therefore, typically this phenomenon is described through the reduction of the inductances at higher load current.
Considering a PMSM, with no physical windings on the rotor, the constant component of the inductance stator matrices described in (1.52) and stated in (1.53) is modified with a non linearity, as

$$\underline{\lambda}^s_{dq}(\underline{i}) = \mathrm{L}_s(\underline{i}_{dq}(t))i_d(t) + L_{sr}(\underline{i}_{dq}(t))I_{pm} \tag{1.89}$$

with

$$\begin{aligned} \mathrm{L}_s(\underline{i}_{dq}(t)) : \mathbb{R}^2 \to \mathbb{R}^2 &= \begin{bmatrix} L_{sd}(\underline{i}_{dq}(t)) & - \\ - & L_{sq}(\underline{i}_{dq}(t)) \end{bmatrix} \\ \mathrm{L}_{sr}(\underline{i}_{dq}(t)) : \mathbb{R}^2 \to \mathbb{R}^2 &= \begin{bmatrix} L_{sd,rd}(\underline{i}_{dq}(t)) & - \\ - & - \end{bmatrix} \end{aligned} \tag{1.90}$$

The dependency from both the $d-q$ currents refers to the cross-saturation effect, where the current does not only saturate the material of the same axis but leads to variations of the flux of the other axis as well. It occurs when parts of the machine significantly saturate and the flux partially moves to paths of the other axis. This tendency introduces a magnetic coupling of the $d-q$ axis. Moreover, the consideration of a permanent magnet flux on the rotor leads to the following further simplification of (1.89)

$$\underline{\lambda}^s_{dq}(\underline{i}_{dq}) = \mathrm{L}_s(\underline{i}_{dq}(t))i^s_{dq}(t) + \underline{\psi}^s_{dq}(\underline{i}_{dq}(t)) \tag{1.91}$$

Also the rotor magnet flux is influenced by the level of the flux produced by the excitation. An example of non linear relationship respectively for the $d-q$ inductances and the permanent magnet flux is shown in Fig. 1.20.

The results have been produced via finit element (FE) analysis and in general are not available for most PMSM machines, in fact the detailed non linear knowledge of the machine electrical parameters does not justify the effort of obtaining such maps by mean of complex simulation analysis or laboratory measurements during commissioning since the machine behaves locally already with a good approximation, according to $\lambda^s_{dq} = \mathrm{L}_s\underline{i}_{dq}(t) + \underline{\psi}^s_{dq}$. However, for our experimental machine the inductance saturation is made available, therefore when necessary, it will be opportunely used as input information for the control strategy. In general the following assumption holds

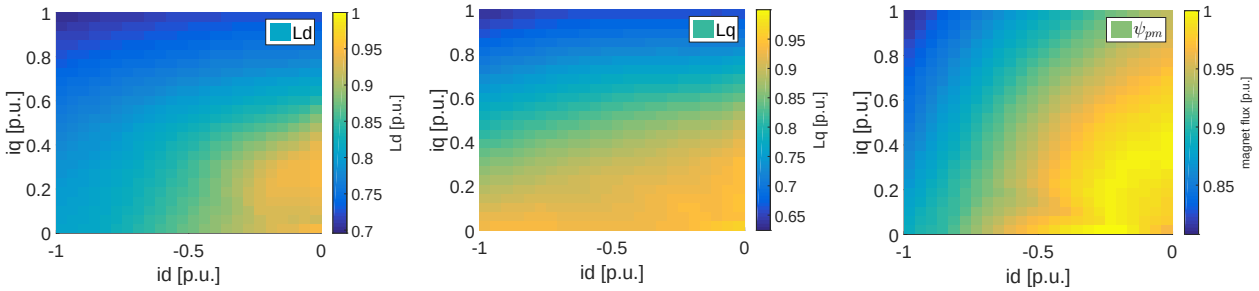

(a) d-axis inductance (b) q-axis inductance (c) magnet flux

Figure 1.20: Non linear 2D electrical parameter dependency calculated through FE simulations.

Assumption 1.6.1. *The linear relation* $\lambda^s_{dq} = \mathrm{L}_s \underline{i}_{dq}(t) + \underline{\psi}^s_{dq}$ *is suitable as local approximation of* $\underline{\lambda}^s_{dq}(\underline{i}_{dq}) = \mathrm{L}_s(\underline{i}_{dq}(t))i^s_{dq}(t) + \underline{\psi}^s_{dq}(\underline{i}_{dq}(t))$ *in the region of desired operation points.*

As a further source of uncertainty, another factor plays an important role in varying the machine state: the temperature. When the electrical power flows within the machine, a certain amount of it is certainly retained by the materials, such as the copper and the iron, under the form of losses, that is the energy which is not converted to mechanical power. The machine losses increase the overall temperature of the materials producing non linearities. In particular, the winding resistance and the residual flux of the permanent magnets are sensitive to the temperature gradient. As an illustrative example, figure 1.21 shows the temperature dependency. Respectively the resistance tends to increase with the temperature while the magnet flux tends to decrease. The latter demagnetizes completely in case it is reached the critical temperature of the specific rare earth considered.

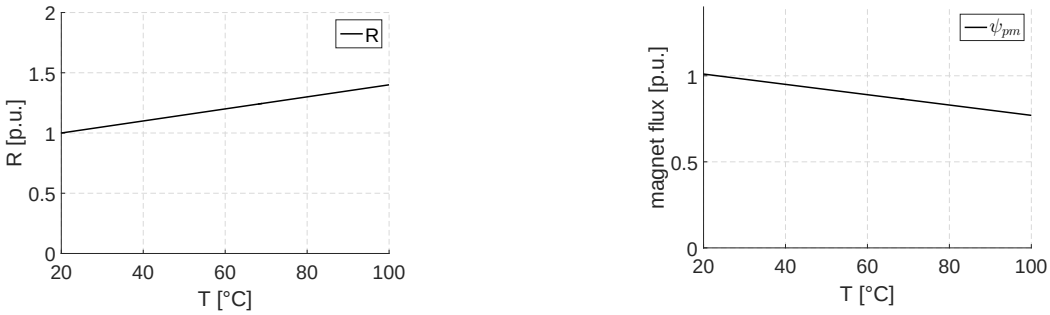

(a) Winding resistance (b) Permanent magnet flux

Figure 1.21: Parameter sensitivity to temperature gradient inside the machine.

This brief introduction to parameter uncertainties of the PMSMs is intended to stress out the fact that, even if the machine can be well approximated to a first order linear state-space system for the design of eventual control strategies, the time-variant parameter dependencies render in reality the electrical behavior of the machine strongly

variable. In case this effects are not regarded within the controller, it could result in severe performances degradation.

1.7. Experimental Platform

The experimental test bench is used to show that the proposed concepts can be implemented and executed in real time. Moreover, it is used to confirm the obtained results experimentally in the presence of non-modeled system behavior. The test bench consists of two back-to-back drive systems. One is a standard industrial drive, which is used to emulate a load and regulate a certain rotational speed of the shaft. On the other drive system, the proposed control developments are tested. The developed control code is compiled for the embedded control hardware, which executes the code in real time. In series between the two electrical machines is inserted a torque sensor, used in particular for the experimentations discussed in Cap. 3. The test-bench setup is shown in Fig. 1.22.

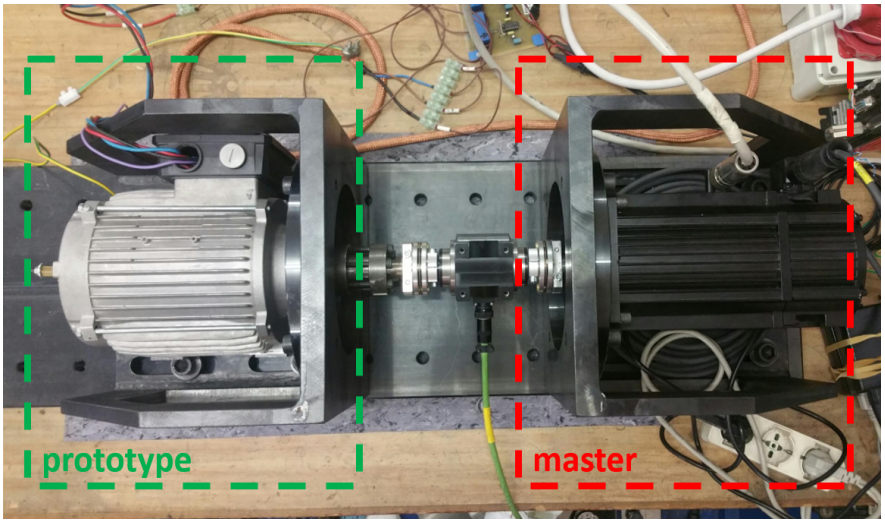

Figure 1.22: Test bed implementation at our facility.

The control code is executed on a dSPACE 1104, which is used as embedded control hardware and consists of a 250MHz PowerPC master chip, which is used to elaborate the real time data, and a 20MHz TI TMS320F240 slave chip, which provides advanced interfaces, e.g. DAC and PWM.. In order to operate the dSPACE board the Real-Time Interface (RTI) is used. This software acts as an interface between Simulink software package and DS1104 hardware. This software package comes along with the DS1104 board. As stated earlier, Real-Time Workshop builds the real-time C-code from the models built in Simulink. That real-time code is then compiled which is downloaded automatically into the target DSP system (DS1104 Controller Board) which is then executed.

Considering more in detail the motor under test during the development of the research work, it is a PMSM motor with interior permanent magnets. The machine was chosen as a good candidate in fact for its geometrical characteristic, it exhibits a

Table 1.2: Drive System Parameters

Power Electronics		
Parameter	Symbol	Value
Type		Two level voltage source inverter
Interlock time	T_i	3 μs
DC bus voltage	U_{DC}	300 V
Switching frequency	f_{sw}	8 kHz
Control Platform		dSPACE 1104
Sampling time	T_s	125 μs
Electrical Machine		
Parameter	Symbol	Value
Type		IPMSM
Pole pair number	z_p	4
Nominal current	I_N	4.7 A_{rms}
Nominal ph-ph voltage	U_N	170 V_{rms}
Nominal power	P_N	1500 W
Base speed	n_B	1500 rpm
Nominal torque	T_N	10 Nm
Phase resistance	R_s	1.5 Ω
Direct inductance	L_{sd}	34 mH
Quadrature inductance	L_{sq}	86 mH
PM flux	Ψ_{pm}	0.2 Vs

strong harmonic spatial-distribution of the fluxes at the air-gap, leading to a strong pulsation of the torque produced. The no-load BEMF can be observed in Fig. 1.23, while Tab. 1.2 resumes the overall drive system specifications of our experimental platform.

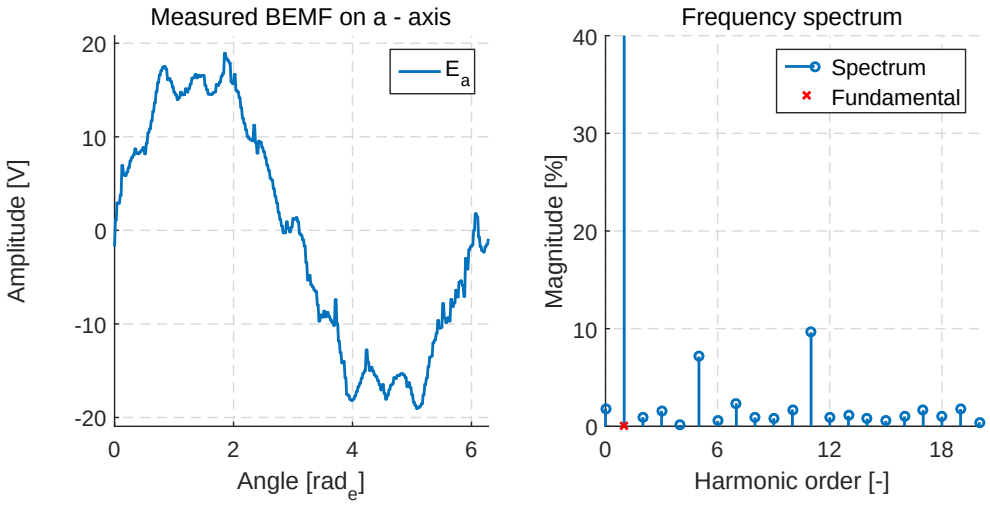

Figure 1.23: No load induced voltage at 200 rpm.

Chapter 2

Constant disturbances compensation

This chapter is devoted to the development and the analysis of the control strategies for improving the behavior of the machine under non idealities, in particular the parameter mismatch. A general introduction on the topic of the disturbance compensation is given. Furthermore effective schemes for tackling the time-varying machine parameters are proposed in place of the classical decoupling network.

2.1. Introduction on the Concept of Observer

Starting from the definition itself, the observer is literally a mathematical instrument which makes some estimation based on its previous observations. Further, the state estimation determines the underlying behavior of the system at any point in time by using past and current measurable information. Observers are useful because they help to reconstruct the state of a system in presence of disturbances or distortions, but more important they can also be used for estimating unmeasurable magnitudes. Therefore, observers are extremely helpful when it is necessary to increase the robustness and the reliability of a system. However, when observer are called for designing a control system, a crucial issue arises, which finds his answer in the concept of observability.

Definition 2.1.1. *Consider a system of the form*

$$\begin{matrix} \dot{x}(t) = f(x,t) \\ y(t) = h(x,t) \end{matrix} \quad , \; x \in \mathbb{R}^n, \; y \in \mathbb{R}^m \tag{2.1}$$

with initial condition x_0 at $t = 0$.
The system is observable if for any possible sequence of state and control vectors, the current state can be determined in finite time using only the outputs.
More formally from $y(x_0, t) = y(\tilde{x}_0, t)$, $t > 0$ follows that $x_0 = \tilde{x}_0$.

Definition 2.1.1 holds for a system of any form, but since in our case the PMSMs can be efficiently represented with a LTI continuous (1.70) and discrete model (1.81), the target of the definition is restricted to the following definition

Definition 2.1.2. *A continuous time-invariant linear state-space model is observable if and only if*

$$rank \begin{bmatrix} \mathrm{C} \\ \mathrm{CA} \\ \dots \\ \mathrm{CA}^{n-1} \end{bmatrix} = n \tag{2.2}$$

which holds also for LTI discrete systems.

The concept of observer is well known from the early 60', when R. Kalman in 1960 theorized the well-known *Kalman filter* (KF) [5] and D. Luenberger in 1964 proposed the state estimation of linear system with the *Luenberger observer* (LO) [6] respectively. They initiated two different school of thought concerning the state estimation problem; in particular the design proposed by the LO is based on a deterministic observer, which means that the disturbances or uncertainties are assumed to be known and systematic, while the concept followed by the KF relies on the stochastic nature of uncertainties, which are thus modeled as noise. But at the very core of both the algorithms they rely on an identical structure, which is also called *predictor-corrector* scheme; in fact within their framework it is contained a virtual model of the real system and in parallel the observer produces and estimation of the real state, which is consequently used for producing a correcting action. The idea is shown in Fig. 2.1.

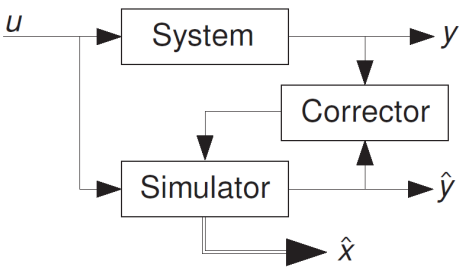

(a) Predictor-corrector structure.

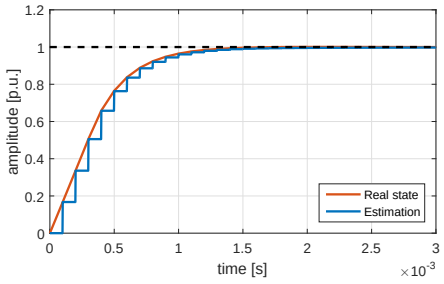

(b) State estimation over time.

Figure 2.1: Introduction on the observer control concept.

Considering an LTI system the observer structure can be defined as follow

Luenberger Observer

$$\dot{\underline{\hat{x}}}(t) = \underbrace{\mathrm{A}\underline{\hat{x}}(t) + \mathrm{B}\underline{u}(t)}_{\text{simulator}} + \underbrace{\mathcal{L}\left(\underline{y}(t) - \underline{\hat{y}}(t)\right)}_{\text{corrector}}$$
$$\underline{\hat{y}}(t) = \mathrm{C}\underline{\hat{x}}(t) \tag{2.3}$$

Kalman Filter

$$\dot{\underline{\hat{x}}}(t) = \underbrace{\mathrm{A}\underline{\hat{x}}(t) + \mathrm{B}\underline{u}(t)}_{\text{simulator}} + \underbrace{\mathcal{K}\left(\underline{y}(t) - \underline{\hat{y}}(t)\right)}_{\text{corrector}}$$
$$\underline{\hat{y}}(t) = \mathrm{C}\underline{\hat{x}}(t) \tag{2.4}$$

where $\mathcal{L}$ is the Luenberger gain and $\mathcal{K}$ is the Kalman gain. As said, the nature of the the two gains is different, in particular one could state that the derivation of $\mathcal{K}$ is optimal and time-variant in the sense that it minimizes the estimation error covariance

over time [7]. On the other side, the gain expressed by $\mathcal{L}$ are in general fixed and designed off-line as to stabilize the process defined by matrices A and B. However, for the special subclass of LTI systems as the $d-q$ model which describes the electrical dynamics of PMSMs, the performances of both the observers are similar and it can be shown in fact that the time-varying Kalman gain converges to a steady-state value, also called "infinite-horizon" linear-quadratic estimator. In the next chapter it will be introduced another estimation technique which has some analogies with the optimality of the KF and under certain simplifications reduces to the very same recursive solution of the least-squares estimation problem.
Disturbances and uncertainties widely exist in all industrial systems and bring adverse effects on performance and even stability of control systems [8, 9], depending on the application. One class of observer is preferable on the other, but both of them are well-known and vastly applied in the the industry [10–19].
The state estimation out of measurement noise is a partial problem which may arise in certain applications and need to be undertaken. However a system can be also affected by input disturbances, which cannot be directly measured, but are required to be compensated for guaranteeing adequate dynamical and steady-state performances. Therefore, from the intuition of the observer principle shown in Fig. 2.1, one can understand that they become suitable tools for estimating the disturbance (or the influence of the disturbance) from measurable variables, and then, a control action can be taken, based on the disturbance estimate, to compensate for the influence of the disturbance. This basic idea can be intuitively extended to deal with uncertainties where the influence of the uncertainties or un-modeled dynamics could be considered as a part of the disturbance. Consequently, in a similar fashion, the influence of the uncertainties could be suppressed, and system robustness can be improved [21, 22]. Both state observer (SO) and disturbance observer based (DOB) can be applied for linear and non-linear system [23–25], moreover the designer decides if both state and disturbance estimation are required or alternative the observer structure can be reduced saving computational effort [26]. In Fig. 2.2 the classification of the observers in its main theoretical types is given. On the other hand, the broad spectrum of the observer strategies applied

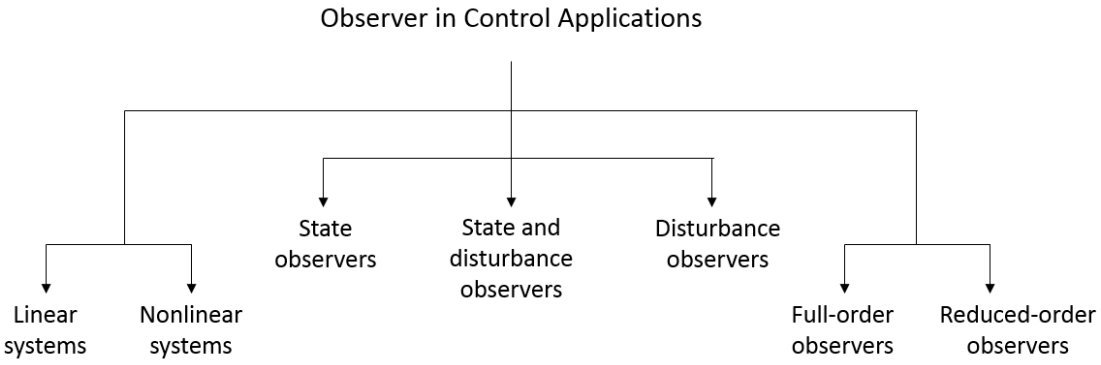

Figure 2.2: Theoretical classification of observers.

in control field for the electrical drives can be resumed with the Fig. 2.3. Most the applications fall in the topic of the position estimation. The goal of our application is to implement observers for tackling part of the disturbances and system uncertainties

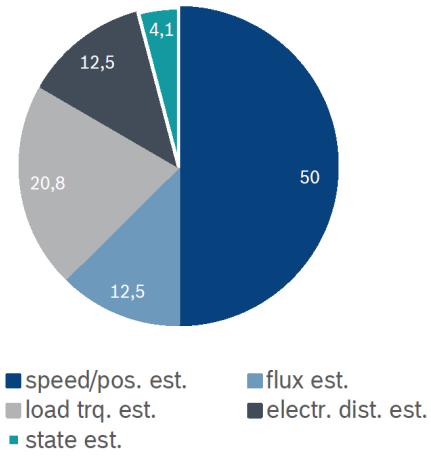

Figure 2.3: Most popular applications of observers for the electrical drives (expressed in %).

presented in Cap. 1, in particular they are very suitable for compensating the unknown mismatch produced by various effects such as iron saturation and temperature drift in electrical parameters (Sec. 1.6), inverter dead-time effects and measurements error (Sec. 1.5).
Since the disturbances we are dealing with in this context is in its nature physical, deterministic and bounded, the focus of what follow is founded on the deterministic approach proposed by Luenberger, which is simpler in its design and cheaper in its implementation. Further, eventual measurement noise, which is unavoidable in digital systems, is considered to affect the system in a light manner, in fact analog or digital filters can be placed for preprocessing the measured signals before to elaborate them within the controller. From equation (2.3) intuitively can be imagined that increasing the gain matrix $\mathcal{L}$, it leads to a faster convergence of the estimation during transient, however, as it will be depended in what follow, a large matrix gain amplifies the noise influence and in general a trade-off has to be found.

2.2. Linear Controller Based on Disturbance Observers

The traditional current control scheme for electric drives consists in a simple configuration based on proportional-integral (PI) controllers, shown in Fig. 2.4.

The controller tends to adjust the input current error, till the measured currents

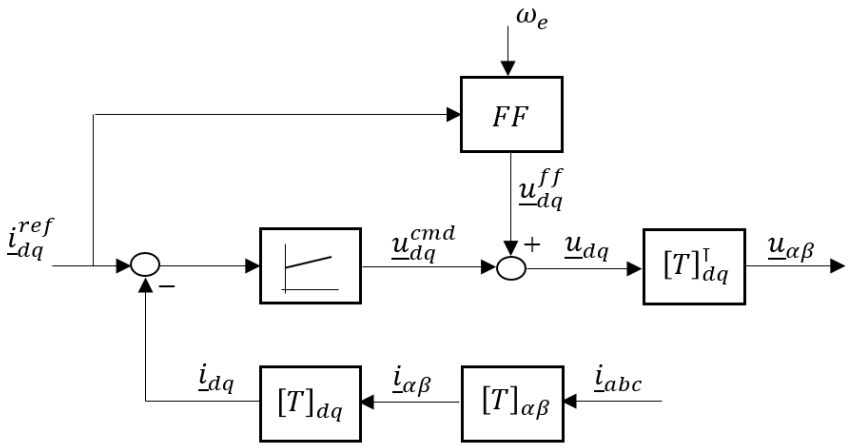

Figure 2.4: Traditional current control block scheme for PMSMs.

transformed in the $d-q$ plane follow exactly the set points. Thus, the current control results in a tracking problem. The PI is also called *feed-back* controller, while the block FF stays for *feedforward* controller, since its contribution does not consider the actual state error.

The feedforward makes use of rough model informations for decoupling the $d-q$ voltage equations (1.26) from the two cross-coupled terms and the rotor PM induced voltage, namely $\omega_e J \underline{\lambda}_{dq}^{s}(t)$. The latter operation is commonly implemented for obtaining a robust design of the PI feedback controller [27, 28].

However, the main drawback of this approach is that its performance depends on several electromechanical parameters that could not be known precisely or they could vary in a large range during the machine operation. Since the design of the regulators and ancillary actions is based on the knowledge of the system, model uncertainties, parameter mismatch and external disturbances could lead to a severe worsening of the drive performance . Robustness and reliability are key features in specific fields of technology as for example automotive and home appliance applications. In these fields, manufacturing and economical reasons often lead to machines with strong non-idealities which are potential source of disturbance. Despite this, the control should guarantee high performances complying with specifications during any drive operation.

In order to capture the unknown input disturbance the observer state-space needs to be augmented with an integrating effect on the disturbance itself, this results in an estimation of the disturbance based on the cumulative mismatch over time between the real system and the simulator within the observer. A simple structure based on the Proportional-Integral Observer (PIO) was suggested in [40] and investigated further in different contexts [41–43]. The PI-Observer assumes bounded disturbances but no other limitations with respect to the dynamics of disturbances. One commonly assumption made during the design of PI-Observers is the modeling of the disturbance as an un-

known piecewise constant term affecting the dynamics of the system. Mathematically can be written as

$$\dot{\underline{w}}(t) = 0 \tag{2.5}$$

where $\underline{w}(t) \in \mathbb{R}$ define a general disturbance vector within the control loop.
The latter means that no information about the dynamical nature of the disturbance is passed to the observer. With this consideration, it is discussed and shown theoretically in [44], [45] and with practical application examples in [46], [47] that the choice for the estimation of time dependent unknown inputs is appropriate.
The reason why PI-Observer are beneficial can be summarized as follow:

- has a simple linear structure in contrast to nonlinear observers;
- is robust against disturbances and noise compared with Luenberger observer or observers without the integral part in the feedback of estimation errors;
- estimates the states and unknown inputs simultaneously in comparison with state or disturbance observers;
- requires no special limitations on the type of disturbances compared with other kinds of state and disturbance observers;
- assumes no statistic information from process and measurement noise in contrast to KF.

In the following section the PI-Observer application for the PMSM will be designed and analyzed showing the potential benefits compared to the State-of-Art algorithms.

2.3. PI Observer Application Analysis on PMSM Current Control

As it has been explained in 2.1 the observer structure emulates a simplified version of the full system, introducing a disturbance term, namely $\underline{w}_{dq}$, which groups all the model dynamics that are in general not known precisely. The latter is also known as *unknown-disturbance* and addresses modeling errors, parameter uncertainties, measurement errors and all other undesired effects. Equation (1.70) with system matrices specified in (1.71) can be re-written as

$$\begin{aligned} \dot{\underline{i}}_{dq}(t) &= \mathrm{A}_c \underline{i}_{dq}(t) + \mathrm{B}_c \left(\underline{u}_{dq}(t) + \underline{w}_{dq}(t) \right) \\ \dot{\underline{w}}_{dq}(t) &= 0 \\ \underline{i}^m_{dq}(t) &= \underline{i}_{dq}(t) + n(t) \end{aligned} \tag{2.6}$$

where

$$\mathrm{A}_c = \begin{bmatrix} -\frac{R}{L_{sd}} & 0 \\ 0 & -\frac{R}{L_{sq}} \end{bmatrix}, \mathrm{B}_c = \begin{bmatrix} \frac{1}{L_{sd}} & 0 \\ 0 & \frac{1}{L_{sq}} \end{bmatrix} \tag{2.7}$$

The PMSM model is reformulated as a linear time-invariant system in which the $d-q$ axis are completely independent. The cross-coupling, the rotor induced voltage and the time-varying nature of the machine parameters are considered by the input

disturbance term $\underline{w}_{dq}(t)$ which is threated as an unknown function. Althought the latter assumption is a simplification, considering that the input disturbance depends from the current, this allows to reduce the complexity of the observer design procedure. For completeness, a measurement noise term, $n(t)$, has been added to the state, thus the measurable system output is indicated as $\underline{i}^m_{dq}(t)$.
The PIO is designed starting from the equation (2.6), which is the prediction model, augmenting the state-space system with the correction terms as

$$\begin{aligned} \dot{\hat{\underline{i}}}_{dq}(t) &= \mathrm{A}_o \hat{\underline{i}}_{dq}(t) + \mathrm{B}_o \left(\underline{u}_{dq}(t) + \hat{\underline{w}}_{dq}(t) + \mathcal{L}_1 \xi(t) \right) \\ \dot{\hat{\underline{w}}}_{dq}(t) &= \mathcal{L}_2 \ \xi(t) \\ \xi(t) &= \underline{i}^m_{dq}(t) - \hat{\underline{i}}_{dq}(t) \end{aligned} \tag{2.8}$$

with

$$\mathcal{L}_1 = \begin{bmatrix} \ell_{1d} & 0 \\ 0 & \ell_{1q} \end{bmatrix}, \quad \mathcal{L}_2 = \begin{bmatrix} \ell_{2d} & 0 \\ 0 & \ell_{2q} \end{bmatrix} \tag{2.9}$$

Here, A_o and B_o are the observer matrices describing the LTI system specified in (2.7), $\mathcal{L}_1$ and $\mathcal{L}_2$ are the observer proportional and integral matrices, $\hat{\underline{w}}_{dq}$ and $\hat{\underline{i}}_{dq}$ are the estimated disturbance and state respectively and ξ is the difference between the measured and the estimated output.

Proposition 2.3.1. *The estimation error produced by the observer converges asymptotically to zero for $t \to \infty$ if and only if the real part of every pole (eigenvalue) in the system's transfer-function is negative.*

Proof. First of all, it is necessary to define an analytical expression for the estimation errors, respectively of the state and the disturbance estimation. Assuming any mismatch between system and observer matrices, namely that $\mathrm{A}_c \equiv \mathrm{A}_o \equiv \mathrm{A}$ and $\mathrm{B}_c \equiv \mathrm{B}_o \equiv \mathrm{B}$, the error dynamics can be represented from (2.6) and (2.8) as follow

$$\begin{bmatrix} \dot{\xi}(t) \\ \dot{\xi}_w(t) \end{bmatrix} = \underbrace{\begin{bmatrix} \mathrm{A} - \mathrm{B}\mathcal{L}_1 & \mathrm{B} \\ -\mathcal{L}_2 & \mathbf{0} \end{bmatrix}}_{\mathrm{A}_{eq}} \begin{bmatrix} \xi(t) \\ \xi_w(t) \end{bmatrix} + \begin{bmatrix} \mathcal{L}_1 \\ \mathcal{L}_2 \end{bmatrix} n(t) \tag{2.10}$$

where $\xi(t) = \underline{i}^m_{dq}(t) - \hat{\underline{i}}_{dq}(t)$ and $\xi_w = \underline{w}_{dq}(t) - \hat{\underline{w}}_{dq}(t)$ are respectively the state estimation error and the disturbance estimation error.
System (2.10) is the augmented model, where the extra-state represents the estimated disturbance. From the relationship between the time and the frequency domain it comes that, similar to the reasoning developed in Prop. 1.4.1, the eigenvalues of the observer augmented matrix A_{eq} correspond to the roots λ_i of the characteristic equation. As a consequence the observer gains $\mathcal{L}_1$ and $\mathcal{L}_2$ have to be placed in order to ensure that $\Re(\lambda_i) < 0$ and that the error dynamics will converge to zero asymptotically over time. This brings the stability of the system and as the λ_i are placed left in the negative half plane, the error will converge faster. The characteristic equation can be calculated as follow:

$$det \begin{bmatrix} \mathrm{A} - \mathrm{B}\mathcal{L}_1 & B \\ -\mathcal{L}_2 & 0 \end{bmatrix} = \lambda^2 - (\mathrm{A} - \mathrm{B}\mathcal{L}_1)\lambda + \mathrm{B}\mathcal{L}_2 = 0 \tag{2.11}$$

Recalling the Descartes' rule of signs, it claims that permanence in the sign between two consecutive terms guarantees the negativity of the real part of the solution. Observing that $\mathrm{A} - \mathrm{B}\mathcal{L}_1 < 0 \;\forall\; \mathcal{L}_1 > 0$ and $\mathrm{B}\mathcal{L}_2 > 0 \;\forall\; \mathcal{L}_2 > 0$, we conclude that the system is stable if the observer gain matrices are strictly positive.

□

Since it results more convenient to study the observer performances in the frequency domain making use of the classical theory, the system (2.6) and its observer formulation (2.8) are transformed from the time domain to the frequency domain making use of the state-space transfer-function relationship, already introduced in Prop. 1.4.1

$$\mathrm{G}_p(s) = (s\mathbf{I} - \mathrm{A}_o)^{-1}\mathrm{B}_o \tag{2.12}$$

Therefore the transfer functions respectively for the measured and estimated $d-q$ currents can be expressed with the Laplace notation as follows

$$\begin{aligned} \underline{i}^m_{dq}(s) &= \left[\underline{u}_{dq}(s) + \underline{w}_{dq}(s)\right] \mathrm{G}_p(s) + n(s) \\ \hat{\underline{i}}_{dq}(s) &= \frac{\left[\underline{u}_{dq}(s) + \underline{i}^m_{dq}(s)\mathrm{G}_{CO}(s)\right] \mathrm{G}^n_p(s)}{1 + \mathrm{G}_{CO}(s)\mathrm{G}^n_p(s)} \end{aligned} \tag{2.13}$$

$$\begin{aligned} \mathrm{G}_P(s) = \frac{1}{\mathrm{L}_s s + \mathrm{R}_s} \quad , \mathrm{G}^n_P(s) = \frac{1}{\mathrm{L}^n_s s + \mathrm{R}^n_s} \\ \mathrm{G}_{CO}(s) = \frac{\mathcal{L}_1 s + \mathcal{L}_2}{s} \end{aligned} \tag{2.14}$$

Here, $\mathrm{G}_P(s)$ and $\mathrm{G}^n_P(s)$ are the actual and nominal model of the machine. The former includes the unknown machine parameters while the latter uses the nominal values that in (2.14) are stated for both dq axes with superscripts n. $\mathrm{G}_{CO}(s)$ is the proportional-integral term of the observer regulator.
The system described in (2.13) can be represented with the block scheme of Fig.2.5. Observer based control schemes are able to cope with disturbances, making the main

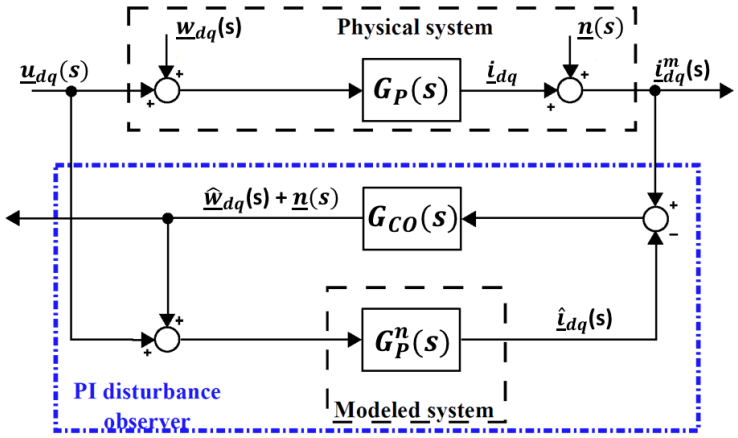

Figure 2.5: PI Observer block scheme

controller insensible to their effects. Moreover, also eventual measurement errors or

offset, stated as $n(s)$ in Fig.2.5 are included in the correction action offered by the observer. The choice of the observer parameters $\mathcal{L}_1$ and $\mathcal{L}_2$ determines its bandwidth that influences the behavior of the system. In particular, the higher the bandwidth the faster the disturbance estimation and the resulting compensation. In other words, a stronger disturbance rejection is obtained increasing the PIO bandwidth. However, the choice of the latter is bounded in real applications by the noise sensitivity of the system which could degrade its performance [43].

A system employing a disturbance decoupling action rejects disturbance independently on the control law. This is because the path that primarily perform disturbance rejection, does not pass through the direct control chain. For this reason, the bandwidth of the observer can be properly tuned to achieve a robust disturbance attenuation without affecting the dynamic behavior of the system. On the contrary, in traditional PI control structures, the disturbance rejection rely only on the main regulators whose bandwidth is limited by the stability constraints.

2.3.1. Traditional PI and PIO-Based Scheme

In this section a comparison between the performance of a common PI control structure and that of an observer-based scheme is reported. In particular, the disturbance rejection capability and the noise sensitivity are considered as indexes of comparison. A

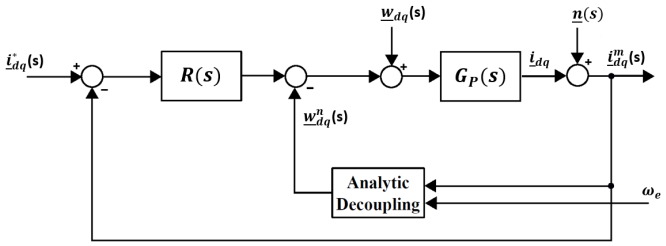

Figure 2.6: Traditional control scheme

traditional PI $d-q$ current control scheme is sketched in Fig.2.6. Here $R(s)$ represents the main regulator with the transfer function composed by the proportional and the integral term, that is

$$\mathrm{R}(s) = \frac{\mathrm{K}_p s + \mathrm{K}_i}{s} \tag{2.15}$$

where K_p and K_i are gain matrices of dimension $n \times n$. The coupling terms $\underline{w}_{dq}(s)$ between the two axes are compensated by the analytic decoupling block. The latter includes the nominal machine parameters as follows

$$\underline{w}^n_{dq}(s) = -\omega_e \mathbf{J} \mathrm{L}^n_s \underline{i}^m_{dq}(s) - \omega_e \underline{\psi}^s_{dq} \tag{2.16}$$

Fig.2.7 shows a PIO-based structure with the same notation introduced in (2.14). The representation of Fig. 2.7a and 2.7b have been introduced for clarity, but their are equivalent, producing the very same effect on the main control-loop.

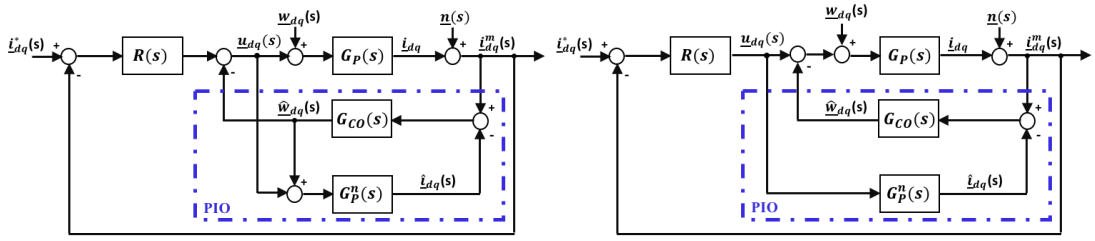

(a) Representation A (b) Representation B

Figure 2.7: Traditional control scheme decoupled with PI Observer.

2.3.2. Disturbance Rejection

The first analysis is made evaluating the disturbance rejection action of the two schemes. In order to do this, the transfer functions between the disturbance $\underline{w}_{dq}(s)$ and the output $\underline{i}_{dq}(s)$ have been derived and reported in (2.17) and (2.18) for the traditional PI and the PIO-based scheme respectively. The noise $\underline{n}(s)$ is considered zero.

$$\frac{\underline{i}_{dq}(s)}{\underline{w}_{dq}(s)} = \frac{\mathrm{G}_P(s)}{1 + \mathrm{R}(s)\mathrm{G}_P(s)} \tag{2.17}$$

$$\frac{\underline{i}_{dq}(s)}{\underline{w}_{dq}(s)} = \frac{\mathrm{G}_P(s)}{(1 + \mathrm{G}_{CO}(s)\mathrm{G}_P^n(s))(1 + \mathrm{R}(s)\mathrm{G}_P(s))} \tag{2.18}$$

Fig. 2.8 shows the bode plots of the considered transfer functions, where for completeness it also shows the cases in which the integrator in the main regulator (2.15) is neglected. This will us serve for further considerations. For the sake of clearness, P and PI refers to Fig. 2.6, while P+PIO and PI+PIO refers to Fig. 2.7 The greater disturbance attenuation of the PIO-based schemes is clearly demonstrated since the red solid line is below the blue dashed curve in most of the considered frequency range. For higher frequencies, all the frequency responses coincide, i.e. the behavior of the system is equal.

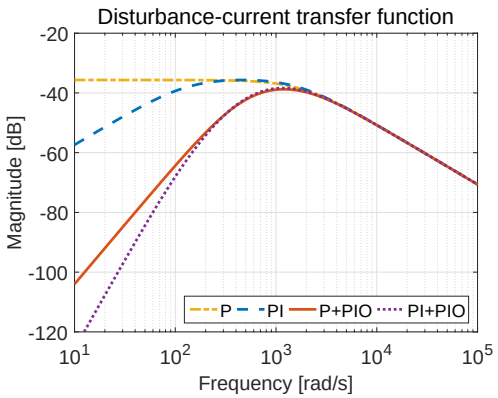

Figure 2.8: Comparison of disturbance attenuation between classical control and PIO-based scheme.

2.3.3. Noise Sensitivity

A second comparison is made in terms of noise sensitivity, thus the disturbance $\underline{w}_{dq}(s)$ is neglected. For both schemes the transfer function from the the noise signal $n(s)$ to the output $\underline{i}_{dq}(s)$ is computed and reported in (2.19) and (2.20) for the traditional PI and the PIO-based scheme respectively. Also for the noise sensitivity the cases without the integrator in the main regulator have been depicted.

$$\frac{\underline{i}_{dq}(s)}{n(s)} = \frac{\mathrm{G}_P(s)}{1+\mathrm{R}(s)\mathrm{G}_P(s)}\mathrm{R}(s) \tag{2.19}$$

$$\frac{\underline{i}_{dq}(s)}{n(s)} = \frac{\mathrm{G}_P(s)}{1+\mathrm{R}(s)\mathrm{G}_P(s)}\left[\frac{\mathrm{G}_{CO}(s)}{1+\mathrm{G}_{CO}(s)\mathrm{G}_P^n(s)}+\mathrm{R}(s)\right] \tag{2.20}$$

The bode plots of Fig. 2.9 empathize the fact that the scheme with the observer has an higher sensitivity to the noise. This effect represents a critical aspect in real applications and it could seriously degrade the drive performance.

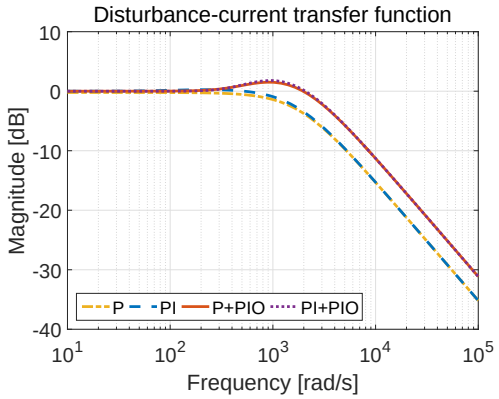

Figure 2.9: Comparison of noise attenuation between classical control and PIO-based scheme.

2.4. Proposed Proportional Controller with Reduced Coupling Path

Hereafter it is presented a variation of the standard PIO-based structure introduced in the previous sections, which substantially improve the overall controller behavior. The considerations made in Sec. 2.3.1 highlighted that the PIO-based control scheme presents an improved disturbance rejection capability but it is more sensitive to high frequency noise compared with a traditional PI control. The aim of this section is to obtain a compromise between these two aspects, i.e. the disturbance rejection and the noise attenuation.
Therefore in order to achieve the latter objective, two main modifications are done:

1. the regulator in the direct path becomes a pure proportional controller.

2. the disturbance compensation is derived only through the integral part of the observer regulator G_{CO}.

The proposed scheme is shown in Fig. 2.10 and the relative transfer functions are described in (2.21).

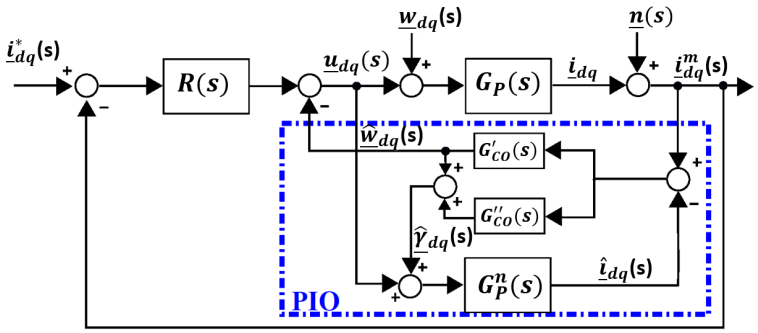

Figure 2.10: Modified version of the decoupling disturbance block scheme.

$$\begin{aligned} \mathrm{R}(s) &= K_p \\ \mathrm{G}'_{CO}(s) = \frac{\mathcal{L}_2}{s} \quad &, \quad \mathrm{G}''_{CO}(s) = \mathcal{L}_1 \\ \mathrm{G}_{CO}(s) &= \mathrm{G}'_{CO}(s) + \mathrm{G}''_{CO}(s) \end{aligned} \tag{2.21}$$

Even if having the full PI in the main regulator leads to a stronger disturbance attenuation, in accordance with Fig. 2.8, removing the integral part in the main loop introduces several advantages in terms of dynamics and ease of design and implementation. In particular, the controller output limitation results much simpler than in PI regulators, where wind-up effects have to be considered. The latter occur in case of large long-lasting error between the reference and the feedback quantity. In this case, if a proper anti wind-up algorithm is not implemented, the output of the integrator goes on increasing and causing overshoot and oscillations on the controlled quantity.
Despite the absence of an integral term in the main path, a null steady state error is guaranteed by the observer integrator action.

Proposition 2.4.1. *The desired current value is asymptotically tracked with a pure proportional controller if and only if the observer is designed as a pure integrator dynamic system.*

Proof. With reference to figure 2.10 let's write the following

$$\underline{\xi}_i(s) = \frac{1}{\mathrm{R}(s)} \left(\underline{u}_{dq}(s) + \hat{\underline{w}}_{dq}(s) \right) \tag{2.22a}$$

$$\hat{\underline{w}}_{dq} = \mathrm{G}'_{CO}(s) \left(\underline{i}^m_{dq}(s) - \hat{\underline{i}}_{dq}(s) \right) \tag{2.22b}$$

$$\hat{\underline{i}}_{dq} = \mathrm{G}^n_P(s) \left(\underline{u}_{dq}(s) + \hat{\underline{\gamma}}_{dq}(s) \right) \tag{2.22c}$$

$$\hat{\underline{\gamma}}_{dq} = \mathrm{G}_{CO}(s) \left(\underline{i}^m_{dq}(s) - \hat{\underline{i}}_{dq}(s) \right) \tag{2.22d}$$

where $\underline{\xi}_i(s) = \left(\underline{i}^*_{dq}(s) - \underline{i}^m_{dq}(s)\right)$ and the nominal observer transfer function is modeled as

$$\mathrm{G}^n_P(s) = \frac{1}{s\mathrm{L}_s} \tag{2.23}$$

Combining (2.22 b) and (2.22 c) it is possible to rewrite $\underline{\hat{w}}_{dq}$ as a function of the observer inputs, namely the commanded voltage $\underline{u}_{dq}$ and the measured current $\underline{i}^m_{dq}$ as follow

$$\underline{\hat{w}}_{dq}(s) = \mathrm{G}^{'}_{CO}(s)\left(\frac{1}{1+\mathrm{G}_{CO}(s)\ \mathrm{G}^n_P(s)}\right)\left(\underline{i}^m_{dq}(s) - \mathrm{G}^n_P(s)\underline{u}_{dq}(s)\right) \tag{2.24}$$

Finally, substituting (2.24) in (2.22 a) leads to

$$\underline{\xi}_i(s) = \mathrm{R}(s)\left[\underline{u}_{dq}(s) + \left(\frac{\mathrm{G}^{'}_{CO}(s)}{1+\mathrm{G}_{CO}(s)\ \mathrm{G}^n_P(s)}\right)\underline{i}^m_{dq}(s) - \left(\frac{\mathrm{G}^{'}_{CO}(s)\ \mathrm{G}^n_P(s)}{1+\mathrm{G}_{CO}(s)\ \mathrm{G}^n_P(s)}\right)\underline{u}_{dq}(s)\right] \tag{2.25}$$

The error in steady state condition ($s \to 0$) is null, in fact

$$\begin{aligned}\underline{\xi}_i(0) &= \frac{1}{R(0)}\left[\underline{u}_{dq}(0) + 0\cdot\underline{i}^m_{dq}(s) - 1\cdot\underline{u}_{dq}(0)\right] \\ &= \frac{1}{K_p}\left[\underline{u}_{dq}(0) - \underline{u}_{dq}(0)\right] = 0\end{aligned} \tag{2.26}$$

with

$$\begin{aligned}&\left(\frac{\mathrm{G}^{'}_{CO}(s)}{1+\mathrm{G}_{CO}(s)\ \mathrm{G}^n_P(s)}\right) \to 0,\ \text{for } s \to 0 \\ &\left(\frac{\mathrm{G}^{'}_{CO}(s)\ \mathrm{G}^n_P(s)}{1+\mathrm{G}_{CO}(s)\ \mathrm{G}^n_P(s)}\right) \to 1,\ \text{for } s \to 0\end{aligned} \tag{2.27}$$

This important result allows a pure proportional controller to be used without having the drawback of the steady-state error. Furthermore, (2.26) highlights another important point. Indeed, since this expression does not depend on the inductance used in the observer, the steady state error is null even in case of parameter uncertainties in the machine model.

□

As derived from Prop. 2.4.1, the observer may compensate even for the resistive voltage drop beyond the other external and internal disturbance. For this reason, the estimated model of the machine in the observer, namely (2.8) can include only the inductive term as follows

$$\begin{aligned}\dot{\hat{\underline{i}}}_{dq}(t) &= \mathrm{B}_o\left(\underline{u}_{dq}(t) + \underline{\hat{w}}_{dq}(t) + \ell_1\underline{\xi}(t)\right) \\ \dot{\underline{\hat{w}}}_{dq}(t) &= \ell_2\underline{\xi}(t) \\ \underline{\xi}(t) &= \underline{i}^m_{dq}(t) - \hat{\underline{i}}_{dq}(t)\end{aligned} \tag{2.28}$$

The model can be represented in the frequency domain as in Fig. 2.11.

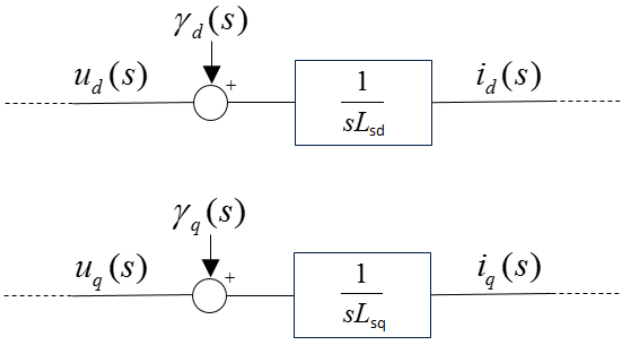

Figure 2.11: Representation of the reduced model of a PMSM to a pure integrator in the frequency domain.

The second modification consists in compensating the disturbance with only the integral term of the observer. Since the observer proportional component does not affect the main path, two main effects in the control performance can be expected and both of them can be qualitatively explained by the slower response of the pure integrator. First, the disturbance rejection will be less effective during disturbance transients since the integral term alone is not able to cope with fast dynamics. On the other hand, a lower sensitivity to high frequency noise is achieved resulting in a more robust behavior of the system. The aforementioned effects can be analyzed by studying the system in the frequency domain. The new transfer functions between the disturbance $\underline{w}_{dq}(s)$ and the output of the drive $\underline{i}_{dq}(s)$ and of the observer $\underline{\hat{w}}_{dq}(s)$ are given by

$$\begin{aligned} \frac{\underline{i}_{dq}(s)}{\underline{w}_{dq}(s)} &= \frac{\mathrm{G}_P(s)}{1+\mathrm{R}(s)\mathrm{G}_P(s)} \cdot \left(1 - \frac{\hat{w}(s)}{w(s)}\right) \\ \frac{\underline{\hat{w}}_{dq}(s)}{\underline{w}_{dq}(s)} &= \mathrm{G}'_{CO}(s)\mathrm{G}_P(s)\left[1 - \frac{\mathrm{G}^n_P(s)\mathrm{G}_{CO}(s)}{1+\mathrm{G}_{CO}(s)\mathrm{G}^n_P(s)}\right] \end{aligned} \tag{2.29}$$

Similarly, the transfer functions between the noise $n(s)$ and the current $\underline{i}_{dq}(s)$ and estimate $\underline{\hat{w}}_{dq}(s)$ can be obtained as

$$\begin{aligned} \frac{\underline{i}_{dq}(s)}{n(s)} &= \frac{\mathrm{G}_P(s)}{1+\mathrm{R}(s)\mathrm{G}_P(s)} \cdot \left[\mathrm{R}(s) + \frac{\underline{\hat{w}}_{dq}(s)}{n(s)}\right] \\ \frac{\underline{\hat{w}}_{dq}(s)}{n(s)} &= \mathrm{G}'_{CO}(s)\left[1 - \frac{\mathrm{G}_{CO}(s)\mathrm{G}_P(s)}{1+\mathrm{G}_{CO}(s)\mathrm{G}^n_P(s)}\right] \end{aligned} \tag{2.30}$$

The bode plot of (2.29) is shown in Fig. 2.12 where the proposed scheme is stated with P+IO. This figure allows comparing the three control structures. It is clear that, in terms of disturbance rejection, the performance of the new scheme are between those of the other two configurations as desired. In other words, P+IO presents a disturbance attenuation stronger than PI but weaker than PIO. Similarly, the transfer function (2.30) that relates the noise to the output current is plotted in Fig. 2.13. Once again, the behavior of the proposed scheme lies between the other two terms of comparison. In particular, P+IO is characterized by a noise sensibility which is higher than PI and lower than PIO. For a deeper understanding of the system behavior under presence of

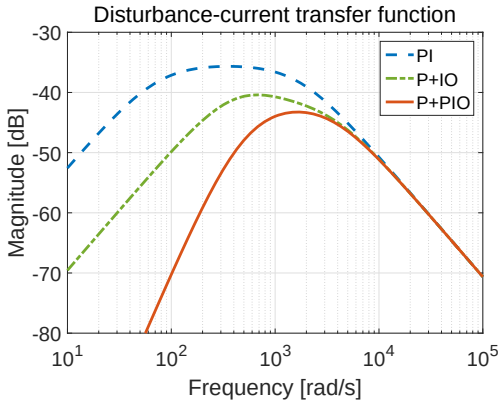

Figure 2.12: Comparison between the effect of PI and I disturbance decoupling on the input disturbance.

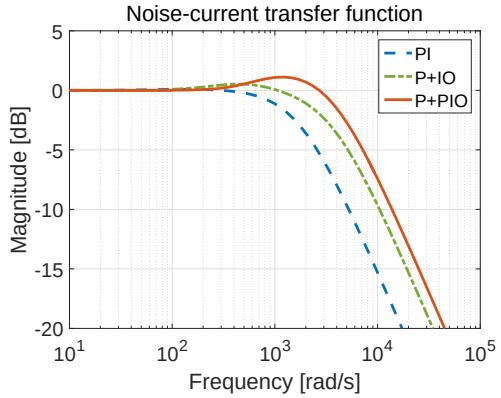

Figure 2.13: Comparison between the effect of PI and I disturbance decoupling on the input noise.

noise, the transfer function between the noise $n(s)$ and the compensation term $\underline{\hat{w}}_{dq}(s)$ has been reported in Fig. 2.14.

The frequency domain analysis of Fig. 2.12 and Fig. 2.13 allows confirming the expected behaviour of the system. For this reason, the proposed scheme represents a good compromise between disturbance rejection and noise sensitivity.

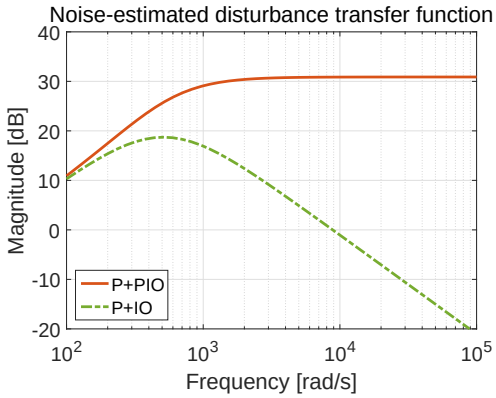

Figure 2.14: Noise sensitivity on the estimated disturbance in case of full PI and only I decoupling path.

2.4.1. Sensitivity Analysis

In this section, an analysis in the frequency domain of the proposed scheme is reported. The first aspect considered is how the gain K_p of the proportional regulators modifies the noise sensitivity and the disturbance rejection of the scheme. The bode plot of the noise-current and of the disturbance-current transfer functions in the dq-axes are reported in Fig. 2.15a and Fig. 2.15b. This parameter has been varied between -50% and $+300\%$ of its optimal value. As can be seen, for both axes, the higher the value of K_p the lower is the attenuation to high frequency noise. On the other hand, increasing the proportional gain results in a stronger disturbance rejection. The choice of this parameter represents a trade-off between the aforementioned aspects.

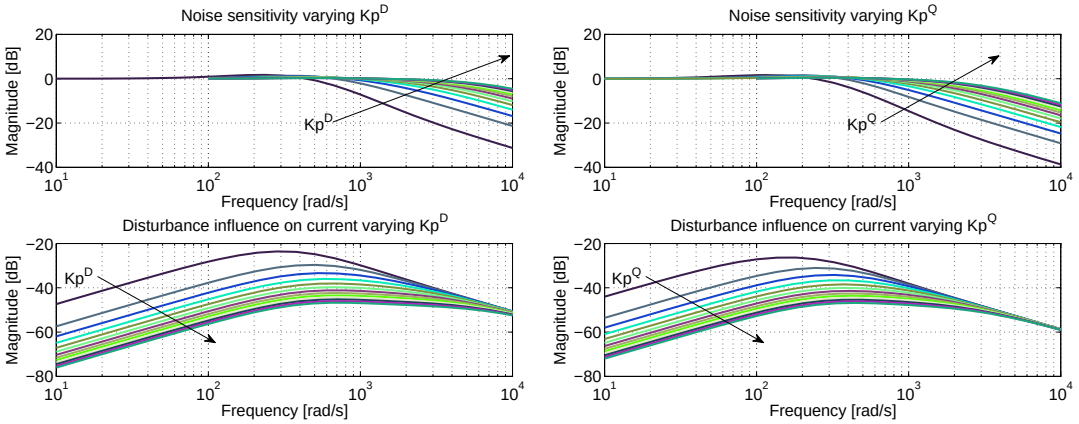

(a) Effect of K_p^D in the d-axis

(b) Effect of K_p^Q in the q-axis

Figure 2.15: Noise and disturbance sensitivity to the main proportional gain variation.

A second analysis has been carried out considering the parameter mismatch. In particular, the inductances of the machine (stated with L_{sd}^r and L_{sq}^r) have been varied

to emulate the iron saturation. The bode blot of the estimated disturbance-disturbance and of the current-disturbance transfer functions has been evaluated and reported in Fig. 2.16a and Fig. 2.16b for the d-axis and the q-axis respectively. The values of the inductances are varied starting from the unsaturated values and are decreased to the 10% of their initial value. It is worth noticing that strong iron saturation, i.e. a high ration between the real and the nominal inductances occurs, affects the tracking capability of the observer. As a consequence, the action of disturbance rejection is reduced as can be seen in the current-disturbance transfer function.

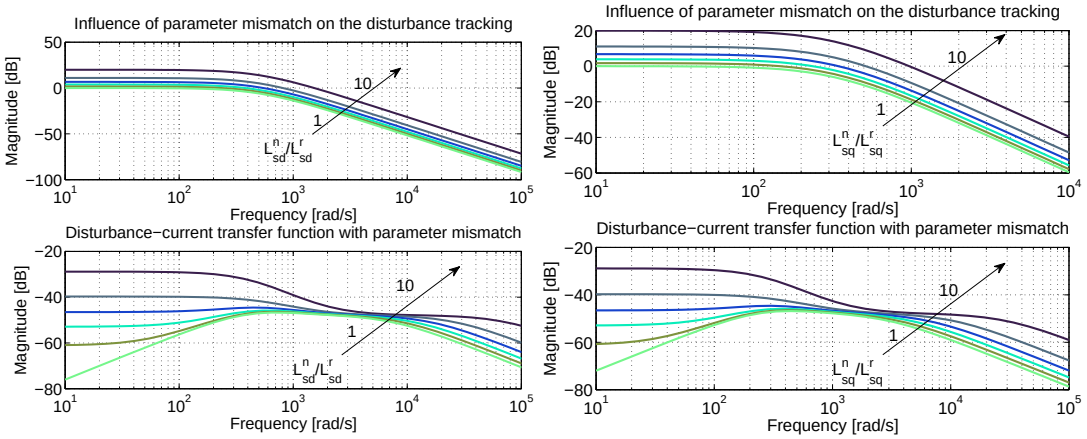

(a) Effect of parameter mismatch : L_{sd} (b) Effect of parameter mismatch : L_{sq}

Figure 2.16: Noise and disturbance sensitivity to the inductance mismatch.

2.5. Implementation

In this section, the proposed control strategy is validated at the test-bench. A comparison is carried between a standard PI controller at different speed reference. The details of the implementation platform at our facility together with the main data of the PMSM utilized, are presented in Sec. 1.7.
The PMSM used for the experimentation shows in general a strong frequency disturbance either at the 6^{th} and the 12^{th} electrical harmonic order. This allows us to evaluate the dynamical performances of the observer and the steady-state disturbance rejection capability.

Table 2.1: Optimized PI and P+PIO gains

- PI control -		
	K_P	K_I
PI - d-axis	51	4203
PI - q-axis	38	6672
- P+PIO control -		
	K_P	
P - d-axis	56	–
P - q-axis	47	–
	l_1	l_2
PIO - d-axis	36	7820
PIO - q-axis	42	8340

2.5.1. Dynamical Performances

As a first set of experimental tests the comparison is run between a standard PI and the proposed pure proportional controller with the PI Observer. In particular, the observer is tested feed-backing the estimation with the full PI (P+PIO) and with the only integral component (P+IO). Both the PI and the P with the PI Observer have been optimized and in Tab. 2.1 the assigned gains are reported.

In Fig. 2.17 the transient response of the system to a current step is shown. The set-point $\underline{i}_{dq} \in \{-2.1, 3.8\}$ lies on the machine MTPA[1]. The experiment is repeated respectively at 100, 300, 500 rpm. It appears clear immediately the strong correlation between the expected behavior deducted by the analyzed transfer functions and the controller response adopting the various strategies. From a dynamical point of view the fastest reaction to a change in the current reference is attained by the PI Observer where the full estimated disturbance is feed to the main controller for compensation. However, fast response leads also to overshoot the set-point. This behavior is encountered also in the response of the PI, in fact since it can control the system dynamics only via its own degree of freedom, a good compromise between dynamical performances and overshoot it is hard to achieve. What seems to provide the best performances is the resulting proposed controller in which only the integral part of the estimated disturbance is feed to the main controller. The pure proportional gain on the main path ensures fast reaction, while the moderate disturbance compensation provided by the PI Observer ensures a precise tracking. This trend between the compared strategies is more evident as the speed increases. A second test is repeated in Fig. 2.18,2.19,2.20. In this case the focus is the comparison between the PI and the P+IO schemes and at each speed level the current load is increased in order to evaluate the eventual performance degradation due to iron saturation. It is possible to notice that in general the PI controller similar to the previous case tends to lose its tracking capabilities and increases the overshoot. In the case of the P+IO controller the performances only slightly reduced and more important is the fact that the overshoot is extremely contained even when the current load is augmented.

[1]Maximum Torque per Ampere

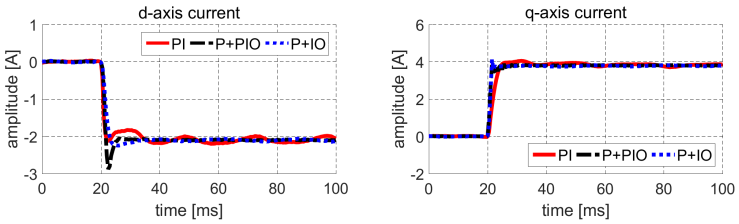

(a) Step-current reference tracking performances at 100 rpm.

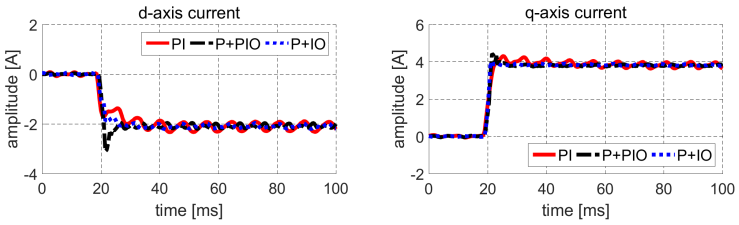

(b) Step-current reference tracking performances at 300 rpm.

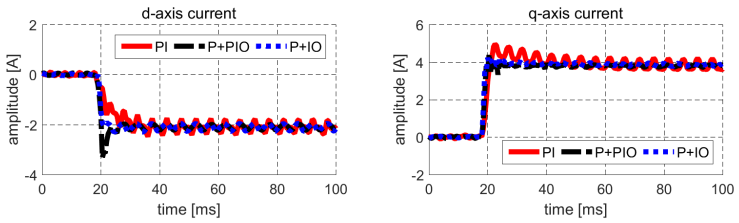

(c) Step-current reference tracking performances at 500 rpm.

Figure 2.17: Measurement of transient step-response performances with fixed load and increasing speed.

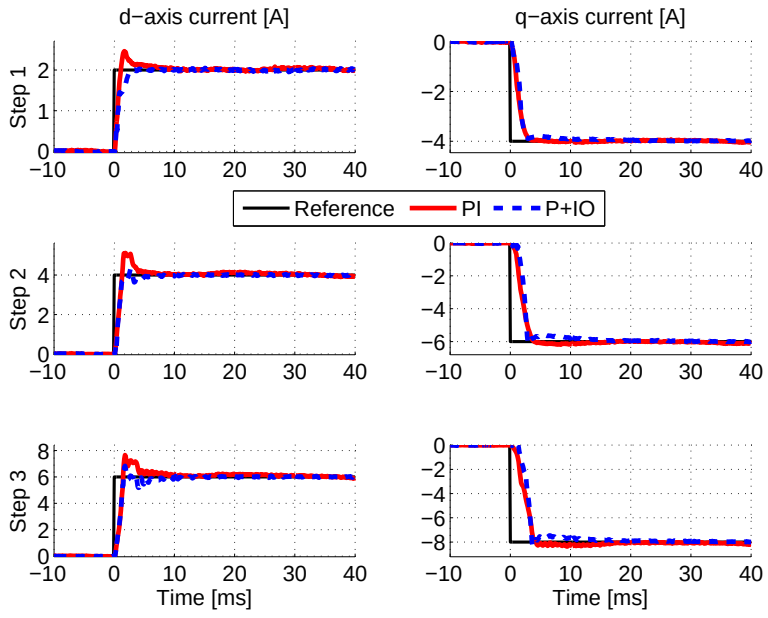

Figure 2.18: Measurement of transient step-response performances current step with increased load at 100 [rpm].

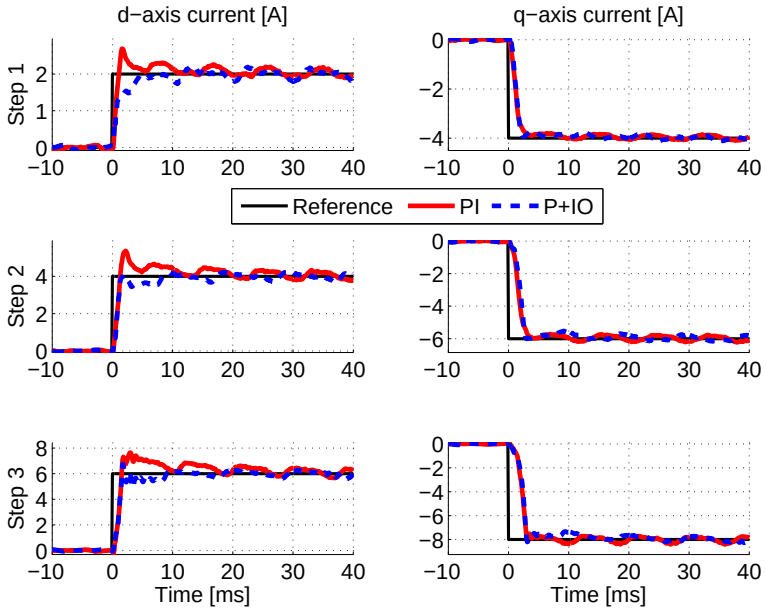

Figure 2.19: Measurement of transient step-response performances current step with increased load at 300 $[rpm]$.

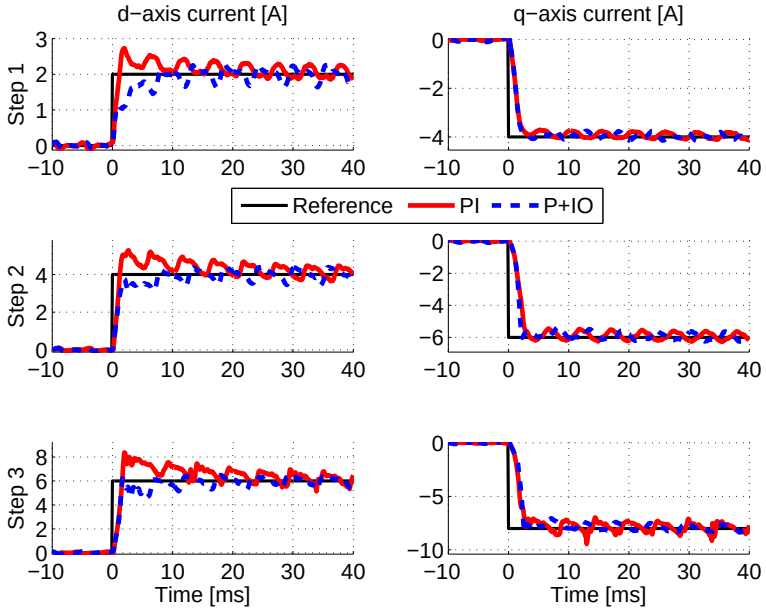

Figure 2.20: Measurement of transient step-response performances current step with increased load at 500 $[rpm]$.

2.5.2. Steady-State Performances

Hereafter the steady-state performance is analyzed with more attention. In Fig. 2.21 the Fourier spectrum decomposition of the step response of Fig. 2.17 is proposed. From the Bode diagrams analyzed in the previous section, the expected performances

are obtained. In general at each speed the P+PIO obtains the highest harmonic disturbance rejection, while the PI the lowest, therefore the observer is able to increase the robustness against disturbances in the control loop along a wider speed range.

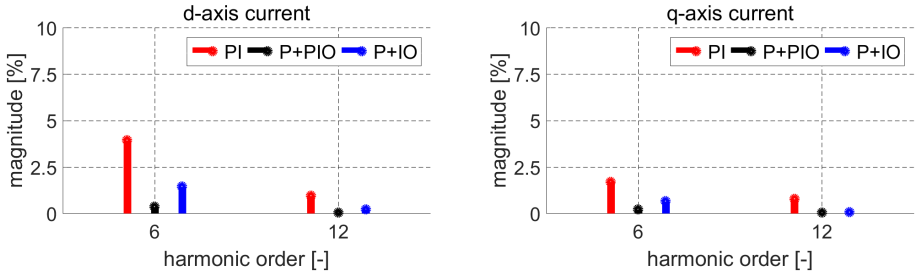

(a) Fourier analysis at 100 *rpm*.

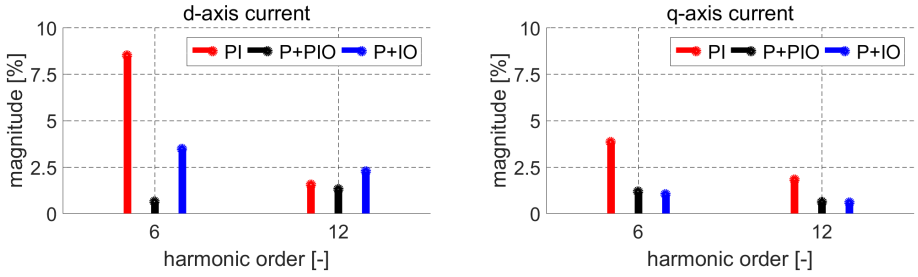

(b) Fourier analysis at 300 *rpm*.

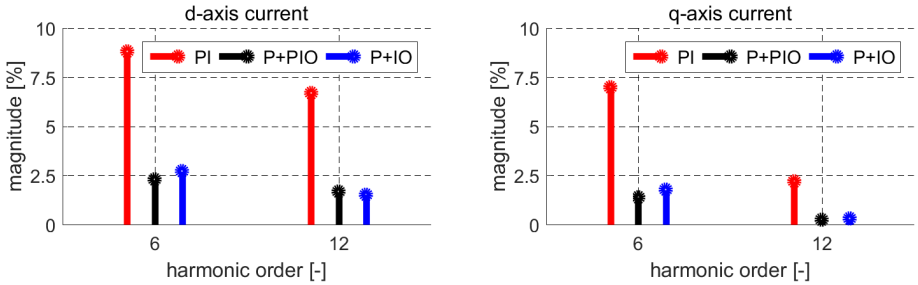

(c) Fourier analysis at 500 *rpm*.

Figure 2.21: Measurement of stead-state harmonic content stressing the disturbance rejection capability of the observer strategy.

Of course this high difference in rejecting the frequency disturbance on the current dynamics reduces as the fundamental frequency increases and as shown in Fig. 2.13 the controller with the integrated observer tends to behave as the standard PI for $\omega_e \to \infty$. This fact is acceptable in fact the rejection of fast disturbances, as could be addressed the harmonics produced by the non sinusoidal flux distribution at the air-gap, is just a matter of bandwidth in this case. Therefore, since the proposed strategies enter in the category of linear fixed-bandwidth controller and the disturbance is threated as un-modeled piecewise constant term, it is not possible to expect strong performances at high fundamental frequency. Simply, the proposed solution is intended to target the model-mismatch which can occur during machine operation and to strengthen the dynamical robustness (in terms of precision tracking) of the current control, at a convenient price in term of hardware resources. In the next chapter, we will focus specifically on the harmonic issue of PMSM developing ad hoc strategies to tackle the problem. As

it will be shown, more sophisticated control schemes are required in order to guaranteeing compensation capabilities independently from the operational frequency of the machine.

Chapter 3

Periodic disturbances compensation

In this chapter the attention is brought on the periodic disturbances arising in PMSMs, which in general causes harmonic distortion in the phase current and torque. The cause-effect chain for manipulating the harmonic content of the machine input and output is deeply analyzed. Methods for the estimation of the harmonic disturbances are presented and consequently, the design of suitable active harmonic cancellation techniques are proposed, showing that the correction of such undesired effects is achievable both in feed-back and in feed-forward.

3.1. Introduction on the Concept of Noise Cancellation

Periodic disturbance compensation is embraced from a much broader field which plays a relevant role in the automation and drive industry, that is the acoustic noise control (ANC). In principle two types of acoustic noise exists: one is so-called *broad-band* noise which is totally random and characterized by fluid turbulence, the second is called *narrow-band* noise and in general it happens when a source of noise concentrates part of its energy on specific frequencies. Rotary machines such as electrical motors are well-known to be classified in the second group; in fact as it has been shown in Cap. 1 and in particular Fig. 1.11, the electromagnetic noise spectrum exists only on specific harmonics.
More in detail, the electromagnetic noise which arises at the air-gap of the machine due to the non sinusoidal spatial distribution of the flux, potentially originates two different source of harmful noise: (i) periodic radial forces which excite the stator teeth at very high frequencies propagating the vibrations on the yoke and the external iron part on which the stator is connected, (ii) periodic tangential forces which lead to an electromagnetic torque pulsation provoking undesired frictional effects on the bearings and on the mechanical coupled parts at the shaft.
Although both the phenomenon arise from the same source and they are characterized by a specific narrow-band noise spectrum dependent from the construction design, they are not correlated with each other. The latter means that taking action for improving the undesired disturbance produced by one source, could worsen heavily the other. Further, for what concerns the radial forces, it is quiet complex to define the cause-

effect transfer function from the air-gap machine quantities, such as the magnet flux and the current distribution, to the radiated sound power produced by the stator sheets accelerations and it involves 3D Finite Element Tools. An example of 3D modeling of the stator deformations due to air-gap forces is shown in Fig. 3.1.
The focus of this research aims to the manipulation of the disturbance which directly affects the controlled magnitudes in the closed-loop; therefore investigating in methods for improving the source of noise cause of tangential tensions on the rotor and torque ripple at the shaft. This phenomenon is especially critical when it is required a precise tracking, for example in the manufacturing and process industries.

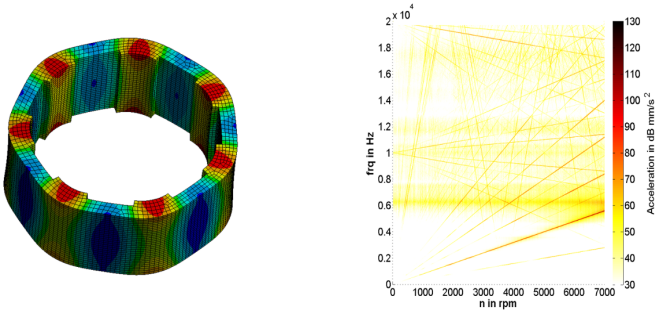

Figure 3.1: Example of a 3D FEA of the stator deformations due to non sinusoidal air-gap flux distribution and its correlated acceleration spectrum.

In order to counteract undesired sources of noise present in a PMSM drive, but more in general in any device which together with its main functionality releases also a certain amount of acoustic noise, two methodologies can be chased: passive and active noise control. The first one are just methods relying on sound absorbing materials which enclose the source of disturbance. However, they are relatively difficult to integrate within compact design of the target devices, costly, and ineffective at low frequencies, making the passive approach to noise reduction often impractical. For these reason in the late 80s, the field of active acoustic noise control started to born and rapidly many algorithms became popular in control engineering. The idea to compensate for noise disturbance with quiet inexpensive software control loops became very attractive [48, 49]. For a survey, the interested author can look at [50] and [51]. The concept of the active acoustic noise cancellation is very simple: a first source emits some undesired frequencies overlapped to the main signal which should be suppressed, therefore a second source opportunely placed will emits the very same magnitude of that noise frequency, but in phase opposition in order to cancel it for the principle of the superposition effects. The concept is represented in Fig. 3.2.

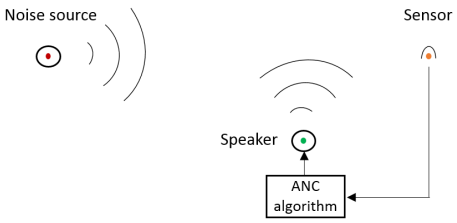

Figure 3.2: Visualization of the active noise control concept in acoustic field.

Transferring this idea on electrical machines, a similar situation can be deduced. In fact, for the sake of simplicity in rotary PMSM the source of noise can be attributed on the rotor reluctance and magnets which produce at the air-gap the main ideal flux with a superimposed series of undesired flux harmonics. The latter, through the Faraday's law of induction (1.15), propagate themselves on the stator coils and also at the shaft, through the interaction with the stator current, they originate forces on the rotor. The harmonic issue for this kind of machines is well known since many decades [52, 53] and already several solutions have been proposed [54, 55].
In the hypothetical case of placing opportunely an Hall effect sensor in the air-gap, the noise quantity could be directly measurable, enabling its suppression through an ANC algorithm. The latter are also called *feed-forward methods*, where the disturbance is directly measured or known in advance and therefore an antiphase signal of the same nature can be straight-forward synthesized in the controller for cancellation purpose. At the contrary *feed-back methods*, as it is the most common case in electrical machines, make us of indirect sensing of the noise through the measured magnitudes at disposal and with an adaptive control algorithm generate a compensation. They are in general more critical regard to stability conditions and thus they need more attention during implementation phase [56].
The challenge with electrical machines is exactly to sense or estimate correctly the disturbance and actively compensate for it at its very nature, therefore modifying the behavior of the stator and rotor flux interaction in the air-gap.
The only degree of freedom at disposal are the voltages generated in the controller and feed to the inverter, which subsequently can manipulate the current flowing into the machine. Therefore, in function of what we need to achieve as objective, the compensation have to be added to the input voltage knowing exactly the effect on the resulting current and the field distribution at the air-gap. The latter is in general extremely hard to achieve in fact the cause-effect relationship between stator and rotor magnitudes includes non linearities and position dependent effects which cannot be easily modeled in practice. It will be shown how even with simplified model informations it is possible to achieve interesting results in terms of undesired noise compensation.
More important, in PMSM we are certainly dealing with narrow-band noise and this fact facilitate the design of an ANC algorithm, in fact even if direct measurement of the disturbance is not available, the exact frequency spectrum of the undesired harmonics is fixed on the fundamental frequency of the machine and known, since a speed sensor is a minimum requirement for an electrical drive. With the intent of robustly reducing or eliminating the torque ripple in PMSM, in the last decades many solution have been proposed, either feed-back methods and feed-forward ones. In [57] the authors proposes an adaptive control algorithm for rejecting specific harmonics on the position of a servo motor. Again, in [58] a resonant controller is designed for mitigating speed oscillation. Unfortunately the majority of them rely on rather complex control structures which reduce the potential practical implementation in commercial drives [59, 60]. Moreover, the harmonic injection is commonly imposed as a current reference, requiring to design a suitable current control for tracking high frequency signals [36, 61], especially for variable frequency high speed drives. Another suitable alternative, in place of injecting harmonics in feed-back approaches, comes directly through model-based considerations. In [62] the authors developed an extended version of the Park transformation in order to compensate torque harmonics and also in [63] a similar method is followed for driving

the machine with specific non-sinusoidal currents with further considerations on losses impact.
Although various tentatives have been proposed, the fact that electrical machines are variable frequency drives makes the whole problem more complex for practical implementation, especially because eventual measurement errors or delay increase their negative effect rapidly with the frequency and instability can occur. Besides that, there is an established number of research scores related to the field of the acoustic noise cancellation. Least mean square (LMS) algorithms and adaptive notch filters are commonly used for suppressing noise [50,51]. Further, quiet efficient methods based on the knowledge of the system's frequency response are used for the adaptive narrow-band sinusoidal disturbance suppression [64]. Inspired by the scientific literature developed in the last two decades the intent of what follow in the chapter is to investigate on these methodologies, evaluate their impact on PMSM and find out the best practice in terms of implementation. The focus will be the torque ripple but generalization on other quantities is opportunely carried out when necessary.

3.2. Real-time Voltage and Torque Disturbance Estimation

As briefly explained in Sec. 3.1, feed-back methods relies on an indirect measurement or estimation of the quantity which is to be suppressed. This methodology is commonly approached in electrical drives, in fact besides laboratory test-benches, in embedded systems it is too expensive to install torque sensors therefore rarely direct measurement of the ripple on the torque is made available. Moreover it is quite challenging also to obtain the precise and clean measurement of the real torque produced by the machine at the test-bench, in fact due to the positioning of the sensor between the sample motor and the load machine, mechanical torsional modes and harmonics produced by the secondary machine can be captured by the sensor and distort the quality of the measure [65]. One of the most common attempt proposed in literature to produce a compensation for the torque disturbance is realized through the speed control loop [66]. The latter relies on direct measurement via encoder or resolver.
This strategy is based on the physical fact that the speed at the shaft has harmonics proportional to the one in the torque [67], which is clearly truth since the rotation of the shaft is produced by the electromagnetic torque generated on the surface of the rotor and the disturbance is propagated on the speed through the mechanical relationship, that is:

$$m(\vartheta_e, \underline{i}_{dq}^{sr}) - m_l = J\frac{d}{dt}\omega_r + b\omega_r \tag{3.1}$$

where m_l is the load torque, J is the inertia of the machine and b is the friction coefficient. However due to limited bandwidth of the sensor and the inertia of the machine, the high frequency noise is rapidly filtered out from the speed measure making the algorithm practical only for low speed drives [67].
A more sophisticated approach which get rid of the speed signal is based on the on-line estimation of the torque ripple. An hybrid solution is proposed in [68], where the voltages are shaped via a non linear Lyapunov controller which monitors the speed error, but also the estimated flux and torque quantities.
Further, in [69] the instantaneous electromagnetic torque is estimated using real-time observation together with pre-computed informations about the non sinusoidal spatial distribution of the rotor flux at the air-gap stored in function of the electrical position. The estimated disturbance is used for shaping the only q-axis current and obtain compensation. Motivated by the effort presents in literature, it has been decided, in this context, to pursue the field of real-time methods for gathering information on the torque disturbance and consequently to use that information for designing a cancellation algorithm.
In Sec. 2.1, the linear estimators have been introduced and successfully employed for improving the dynamical performances of the current control against parameter uncertainties. As already marked, the usage of simple linear observer structure has several applications in the context of PMSMs control. However the limit of these algorithms is their attachment on a prediction-correction action path which has a specific bandwidth and thus the residual noise produced by the machine is hardly followed.
Consequently, if we want to gather some accurate information on the disturbance, the capability of the classical linear observer needs to be enhanced. In doing this it becomes extremely important to consider the measurement noise issue, which can easily corrupt the performance of the estimator at high frequencies.

Hereafter an advanced observer methodology is going to be constructed through its own cost-function, where we can clearly state the goal of our estimator making also easier to introduce a degree of freedom for controlling the noise injection.

3.2.1. Observer Algorithm Based on Quadratic Programming

It has been observed in Sec. 1.3.2 that the general torque expression of a PMSM, formulated in the rotor reference frame, is composed of various position-dependent terms (1.64), which lead to periodic sinusoidal functions synchronized on the 6^{th} harmonic and its multiples. In particular there is a reluctance contribution produced by the interaction of the only stator currents, a synchronous contribution caused by the interaction between the stator currents and the permanent magnet flux and the cogging torque harmonics. The latter is an external torque disturbance, therefore does not influence stator magnitudes and cannot be seen within the electrical system. But in this context we assume that the cogging torque is not the predominant source of disturbance, therefore our focus is on the other two terms, which clearly influence the machine current and voltage (see (1.55)).
At an high level of abstraction it is possible to model the electromagnetic power function as a *Fourier series*, that is

$$P_{me}(\theta_e) = \sum_{n=0}^{\infty} P_{me,6n} \mathrm{e}^{j6n\theta_e} \tag{3.2}$$

where n is the harmonic order contribution to the electrical power and the subscript 0 indicates the nominal constant component.
Similar to the LTI state-space model introduced in Sec. 2.3, namely (2.6), the disturbance is assumed piecewise constant, including the un-modeled voltage disturbance from the non sinusoidal flux and the nonlinear dynamics, namely referring to (1.55)

$$\underline{w}_{dq}(t) = -\left(\omega_e \mathbf{J} \underline{\lambda}^s_{dq}(\underline{i}) + \underline{d}^s_{dq}(\theta_e, \omega_e, \underline{i})\right) \tag{3.3}$$

An estimation of the system states can be built exploiting the observed input-output signals and an internal model which simulates the real current dynamics in $d-q$ reference frame

$$\frac{d}{dt}\hat{\underline{i}}_{dq}(t) = \mathrm{A}_o \hat{\underline{i}}_{dq}(t) + \mathrm{B}_o(\underline{u}_{dq}(t) + \underline{\hat{w}}_{dq}(t)) \tag{3.4}$$

The output of the estimation will be, as for the linear PI Observer case (2.8), the tracked measured current and the full machine voltage disturbance which affects the current dynamics, in fact in (3.4) there isn't any disturbance effect modeled. However the design of the correction law after observer prediction is not anymore based on a linear transfer function, such as (2.14), but rather on an adaptive law. The attempt here is to characterize the observer estimation as an optimization problem, in which we want to minimize the error between the measured and the estimated current over time.
This kind of observer structure enters within the field of *Moving Horizon Estimation* (MHE) [71].

The simplest quadratic problem formulation can be stated as

$$\begin{aligned} min\ \ J &= \frac{1}{2}(\underline{i}^m_{dq}(t) - \hat{\underline{i}}_{dq}(t))^2 \\ s.t.\ \frac{d}{dt}\hat{\underline{i}}_{dq}(t) &= \mathrm{A}_o\hat{\underline{i}}_{dq}(t) + \mathrm{B}_o(\underline{u}_{dq}(t) + \underline{\hat{w}}_{dq}(t)) \end{aligned} \tag{3.5}$$

On the basis of the optimization problem (3.5), two major strategies to approach a dynamic optimal control problem can be distinguished up-front:

- **Direct methods** first perform full time discretization, which eliminates the time dependency and allows for application of stationary optimization algorithms to (3.5).
- **Indirect methods** solve the optimization problem in function space to obtain some general optimality conditions first. These are discretized to compute an optimal solution afterwards.

A direct approach has been hereafter pursued, since it has a more clear structure and more flexibility in terms of cost function refinement for further objectives.
Let us consider a moving time window, as sketched in Fig. 3.3, where the red dots are the measurements and the black dots represent the estimated state within a defined window which is moving forward each sampling time. Making use of a direct method for defining the estimation problem, (3.4) is first discretized using the forward Euler method (1.81), as follow

$$\hat{\underline{i}}_{dq}(k+1) = \mathrm{A}_d\hat{\underline{i}}_{dq}(k) + \mathrm{B}_d\underline{u}_{dq}(k) + \mathrm{B}_d\underline{\hat{w}}_{dq}(k) \tag{3.6}$$

where

$$\mathrm{A}_d = \begin{bmatrix} 1 - T_c\frac{R_s}{L_d} & 0 \\ 0 & 1 - T_c\frac{R_s}{L_q} \end{bmatrix}, \quad \mathrm{B}_d = \begin{bmatrix} \frac{T_c}{L_d} & 0 \\ 0 & \frac{T_c}{L_q} \end{bmatrix} \tag{3.7}$$

are the discretized version of matrices A_c and B_c in (3.4). The voltage disturbance $\underline{\hat{w}}_{dq}(k)$ is further expressed conveniently as a variational term to incorporate an integrative effect of the estimation over time. This allows us to define our unknown variable as the $\Delta\underline{\hat{w}}_{dq}(k)$ between the previous and the actual sample, that is

$$\underline{\hat{w}}_{dq}(k) = \underline{\hat{w}}_{dq}(k\text{–}1) + \Delta\underline{\hat{w}}_{dq}(k) \tag{3.8}$$

The discrete-time current dynamics expressed in (3.6) can be generalized to an horizon in the past of length N intervals, therefore the estimated state at the instant z, previous to the actual, is written as follow

$$\begin{aligned} \hat{\underline{i}}_{dq}(k\text{–}z) = \mathrm{A}_d^{N-h}(\hat{\underline{i}}_{dq}(k\text{–}N)) \ + \sum_{j=1}^{N-z} \mathrm{A}_d^{N-z-j}\mathrm{B}_d[u_{dq}(k\text{–}N\text{–}1{+}j) + \underline{\hat{w}}_{dq}(k\text{–}N\text{–}2{+}j)] \ + \\ + \sum_{j=1}^{N-z} \mathrm{A}_d^{N-z-j}\mathrm{B}_d(\Delta\underline{\hat{w}}_{dq}(k\text{–}N\text{–}1{+}j)) \end{aligned} \tag{3.9}$$

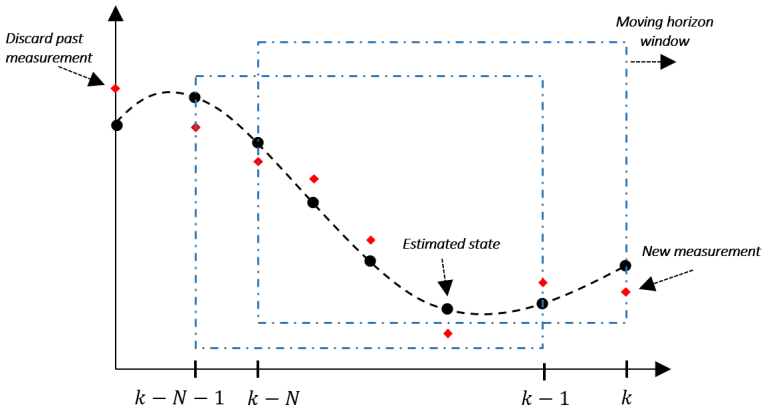

Figure 3.3: Moving Horizon Estimator.

with $z = 0, \ldots, N-1$.
Equation (3.9) can be written in a compact vectorial form expressing the estimated state from the oldest value to the most recent as

$$\mathrm{X} = \Phi_i x_0 + \Gamma_u(\mathrm{U} + W) + \Gamma_u \Delta W \tag{3.10}$$

with

$$\mathrm{X} = \begin{bmatrix} \hat{\underline{i}}_{dq,k-N+1} \\ \vdots \\ \hat{\underline{i}}_{dq,k} \end{bmatrix}, \mathrm{U} = \begin{bmatrix} \underline{u}_{dq,k-N} \\ \vdots \\ \underline{u}_{dq,k-1} \end{bmatrix}, \mathrm{W} = \begin{bmatrix} \underline{\hat{w}}_{dq,k-N-1} \\ \vdots \\ \underline{\hat{w}}_{dq,k-2} \end{bmatrix}$$

$$\Phi_i = \begin{bmatrix} \mathrm{A}_d \\ \mathrm{A}_d^2 \\ \vdots \\ \mathrm{A}_d^N \end{bmatrix}, \Gamma_u = \begin{bmatrix} \mathrm{B}_d & \mathbf{0} & \ldots & \mathbf{0} \\ \mathrm{A}_d\mathrm{B}_d & \mathrm{B}_d & \ldots & \mathbf{0} \\ \vdots & \vdots & \ddots & \mathbf{0} \\ \mathrm{A}_d^{N-1}\mathrm{B}_d & \mathrm{A}_d^{N-2}\mathrm{B}_d & \ldots & \mathrm{B}_d \end{bmatrix}$$

$$\Delta \mathrm{W} = \left[\Delta \underline{\hat{w}}_{dq,k-N} \ldots \Delta \underline{\hat{w}}_{dq,k-1}\right]^T$$

The initial condition, i.e. the oldest estimation available from the previous moving horizon window, is expressed by $x_0 = \hat{\underline{i}}_{dq}(k-N)$.
Once the model has been fully discretized as in (3.10), it is possible to construct the cost function which is the core of the estimator, that is

$$J(\Delta \mathrm{W}) = (\mathrm{Y} - \mathrm{X})^\top \mathrm{Q}(\mathrm{Y} - \mathrm{X}) + \Delta \mathrm{W}^\top \mathrm{R} \Delta \mathrm{W} + (\bar{\mathrm{X}} - C\mathrm{X})^\top \mathrm{S}(\bar{\mathrm{X}} - C\mathrm{X}) \tag{3.11}$$

where

$$\mathrm{Q} = \begin{bmatrix} \underline{q}_1 & \ldots & \mathbf{0} \\ \vdots & \ddots & \vdots \\ \mathbf{0} & \ldots & \underline{q}_N \end{bmatrix}, \mathrm{R} = \begin{bmatrix} \underline{r}_1 & \ldots & \mathbf{0} \\ \vdots & \ddots & \vdots \\ \mathbf{0} & \ldots & \underline{r}_N \end{bmatrix}$$

$$\mathrm{S} = \begin{bmatrix} \underline{s}_1 & \dots & \mathbf{0} \\ \vdots & \ddots & \vdots \\ \mathbf{0} & \dots & \underline{s}_N \end{bmatrix}, \mathrm{C} = \begin{bmatrix} \mathbf{I}_1 & \dots & \mathbf{0} \\ \vdots & \ddots & \vdots \\ \mathbf{0} & \dots & \mathbf{0}_N \end{bmatrix}$$

$$\mathrm{Y} = \begin{bmatrix} \underline{i}_{dq,k-N+1} \\ \vdots \\ \underline{i}_{dq,k} \end{bmatrix}, \bar{\mathrm{X}} = \begin{bmatrix} \bar{x}_{dq,k-N+1} \\ \vdots \\ \mathbf{0} \end{bmatrix}$$

Definition 3.2.1. *Let $\underline{q}$, $\underline{r}$, $\underline{s}$, represent state matrices of the size $n \times n$, namely*

$$\underline{q}_i = \begin{bmatrix} q_i^d & 0 \\ 0 & q_i^q \end{bmatrix} \quad \underline{r}_i = \begin{bmatrix} r_i^d & 0 \\ 0 & r_i^q \end{bmatrix} \quad \underline{s}_i = \begin{bmatrix} s_i^d & 0 \\ 0 & s_i^q \end{bmatrix} \tag{3.12}$$

with $i = 0, \dots, N$. The matrices $\underline{q}$, $\underline{r}$, $\underline{s}$ are all positive definite by definition and this can be guaranteed by choosing the diagonal terms, such that they are all $\mathbb{R}^+$.

The matrix C has only the first diagonal element equal to the identity matrix, for considering only the oldest estimation.
The cost function (3.11) is composed of three quadratic terms: the first term penalizes the deviation between the estimated state vector X and the measured state vector Y, the second term acts as a regularization term on the estimated voltage disturbance and the third term, the so-called *terminal-cost*, provides consistency to the actual optimization problem with the past state informations that are not explicitly accounted for in the current time window, but included in $\bar{\mathrm{X}}$. Through the choice of the weighting matrices Q, R, and S it is possible to tune the performances of the estimator in terms of stability and robustness to measurement noise.
Moreover, since our machine model (3.4) is a linear first order system of size $n \times n$, the cost function (3.11) is strictly convex quadratic with N linear equality constraints and this setup allows a closed-form solution of the problem to be obtained. Referring to (3.10) and (3.11), the following Linear Quadratic Problem (LQP) can be stated:

$$\min \quad \frac{1}{2} J(\mathrm{X}, \Delta\mathrm{W}) \tag{3.13a}$$

$$s.t. \quad \mathrm{X} = \Phi_i x_0 + \Gamma_u(\mathrm{U} + \mathrm{W}) + \Gamma_u \Delta\mathrm{W} \tag{3.13b}$$

where, our optimization variable vector is defined by $\Delta\mathrm{W}$.
Since the motor voltage disturbance is deterministic and well-defined by the geometry of the machine, including inequality boundaries on W would just add extra computational effort without producing any benefit, therefore in this context a simplified version of the MHE is implemented, enabling real-time computation of the solution under hard time constraint.
In order to obtain the explicit dense solution of the optimization problem (3.13), it is necessary to transform it in its unconstrained version, that is, the equality (3.13b) is substituted in (3.13a).
This leads to

$$J = (\Delta\mathrm{X} - \Gamma_u\Delta\mathrm{W})^\top \mathrm{Q}(\Delta\mathrm{X} - \Gamma_u\Delta\mathrm{W}) + (\Delta\bar{\mathrm{X}} - \mathrm{C}\Gamma_u\Delta\mathrm{W})^\top \mathrm{S}(\Delta\bar{\mathrm{X}} - \mathrm{C}\Gamma_u\Delta\mathrm{W}) + \Delta\mathrm{W}^\top \mathrm{R}\Delta\mathrm{W} \tag{3.14}$$

with

$$\Delta \mathrm{X} = \mathrm{Y} - \Phi_i x_0 - \Gamma_u(\mathrm{U} + \mathrm{W})$$
$$\Delta \bar{\mathrm{X}} = \bar{\mathrm{X}} - \mathrm{C}\Phi_i x_0 - \mathrm{C}\Gamma_u(\mathrm{U} + \mathrm{W})$$

Through some algebra, (3.14) can be transformed in the canonical linear-quadratic formulation as

$$J = \frac{1}{2}\Delta \mathrm{W}^\top H \Delta \mathrm{W} + g\Delta \mathrm{W} + c \tag{3.15}$$

with

$$\mathrm{H} = \Gamma_u^\top \mathrm{Q}\Gamma_u + \Gamma_u^\top \mathrm{C}^\top \mathrm{S}\mathrm{C}\Gamma_u + \mathrm{R}$$
$$g = -2(\Delta \mathrm{X}^\top \mathrm{Q}\Gamma_u + \Delta \bar{\mathrm{X}}^\top \mathrm{C}\Gamma_u)$$
$$c = \Delta \mathrm{X}^\top \mathrm{Q}\Delta \mathrm{X} + \Delta \bar{\mathrm{X}}^\top \mathrm{S}\Delta \bar{\mathrm{X}}$$

$\mathrm{H} \in \mathbb{R}^{nN \times nN}$, $g \in \mathbb{R}^{1 \times nN}$ and $c \in \mathbb{R}$ are respectively the quadratic, the linear and the constant terms of the LQP.
The closed-form solution can be computed posing the gradient of (3.15) to zero, that is

$$\Delta \mathrm{W}^{opt} = -\mathrm{H}^{-1} g^\top \tag{3.16}$$

For definition 3.2.1, matrix H is guaranteed to have full rank and be positive definite, therefore the inverse is fully defined.
Equation (3.16) is the optimal explicit solution of the proposed estimator which is updated at each sampling time, tracking the measured motor current and producing an estimation of the varying disturbance affecting the current-voltage PMSM system, addressed for simplicity by (3.3).

3.2.2. Instantaneous Electromagnetic Power Computation

The algorithm introduced in the last section is capable to estimate the motional voltage affecting the PMSM, reproducing the discrete time evolution of the voltage disturbance. Therefore, the information from the output of the Linear Quadratic Observer (LQO) can be exploited for improving the output machine torque. Further, the exact frequencies, on which the periodic disturbance acts, are known (3.2); thus it is possible to use that information to generate a certain rotating voltage through the inverter for attenuating or possibly canceling these specific harmonics. In normal operative condition, the machine is not using the full DC voltage bus, thus the remaining part can be used for harmonic cancellation. The idea is sketched in Fig. 3.4.
Since the goal is to have an estimation of the torque disturbance, that information can be gathered from the instantaneous power computed starting from the estimated voltage disturbance. In order to shape some harmonic voltage within a feed-back path, it is necessary to extract a ripple quantity from the observers, therefore the estimated voltage disturbance components are first combined together with the currents to produce an estimation of the instantaneous power as

$$\hat{P}_{dq}(\theta_e) = -\frac{3}{2}\left(\hat{\underline{i}}_{dq}^\top(t)\hat{\underline{w}}_{dq}(\theta_e)\right) \tag{3.17}$$

It should be remarked that considering the mathematical model developed in Sec. 1.3.1, the computed quantity (3.17), in accordance with (3.3), (1.55) and (1.56), contains not only the mechanical power harmonics, but also the pulsation of the magnetic energy.

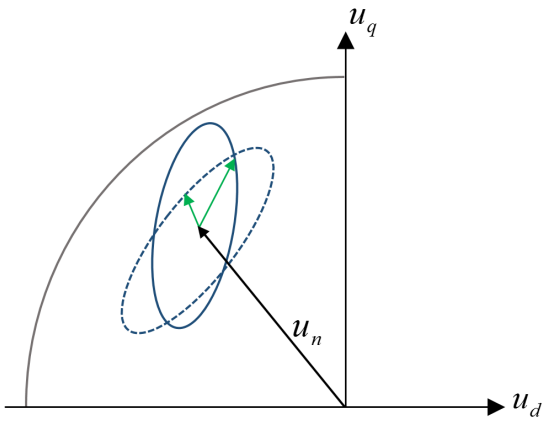

Figure 3.4: Different compensating voltage trajectories which use the remaining free DC bus for fulfilling additional control tasks such as the torque harmonics compensation.

Assumption 3.2.1. *The added harmonic terms, estimated from the observation of the stator magnitudes, are assumed to do not corrupt the estimation, therefore* $\underline{\hat{w}}_{dq}(\vartheta_e)$ *can be considered as a reliable mean for the real-time electromagnetic power and torque prediction.*

This can be proved through the detailed analysis of the voltage disturbance component of the PMSM. From (3.3), knowing $\underline{d}^s_{dq}(\theta_e, \omega_e, \underline{i})$ from (1.55) it is possible to write

$$\underline{\hat{w}}_{dq}(\vartheta_e) = -\omega_e \mathbf{J} \underline{\lambda}^s_{dq}(\underline{i}) - \underline{p}_{dq}(\vartheta_e, \underline{i}^{sr}_{dq}) - \omega_e \left(\underline{q}_{dq}(\vartheta_e, \underline{i}^{sr}_{dq}) + \mathbf{J}^\top \underline{\dot{q}}_{dq}(\vartheta_e, \underline{i}^{sr}_{dq}) \right) \tag{3.18}$$

Substituting (1.56) in (3.18) yields to

$$\begin{aligned} \underline{\hat{w}}_{dq}(\vartheta_e) = &- \omega_e \mathbf{J} \underline{\lambda}^s_{dq}(\underline{i})(t) - \tilde{\mathrm{L}}_s \frac{d}{dt} \underline{i}^s_{dq}(t) - \omega_e \left(\mathbf{J} \tilde{\mathrm{L}}_s \underline{i}^s_{dq}(t) + \mathbf{J} \tilde{\mathrm{L}}_{sr} \underline{i}^r_{dq} \right) \\ &- \omega_e \left(\mathbf{J}^\top \mathbf{J} \frac{d}{d\vartheta_e} \tilde{\mathrm{L}}_s(\vartheta_e) \underline{\hat{i}}^\top_{dq}(t) + \mathbf{J}^\top \mathbf{J} \frac{d}{d\vartheta_e} \tilde{\mathrm{L}}_{sr}(\vartheta_e) \underline{\hat{i}}^r_{dq}(t) \right) \end{aligned} \tag{3.19}$$

and computing the power from (3.17), follow

$$\begin{aligned} \hat{P}_{dq}(\theta_e) = \frac{3}{2} \Big[&\omega_e \underline{\hat{i}}^{s\top}_{dq}(t) \mathbf{J} \underline{\lambda}^s_{dq}(\vartheta_e, \underline{i}^{sr}_{dq}) + \underline{\hat{i}}^{s\top}_{dq}(t) L_s(\vartheta_e) \frac{d}{dt} \underline{i}^s_{dq}(t) + \underline{\hat{i}}^{s\top}_{dq}(t) L_{sr}(\vartheta_e) \frac{d}{dt} \underline{i}^r_{dq}(t) \\ &+ \omega_e \left(\underline{\hat{i}}^{s\top}_{dq}(t) \mathbf{J}^\top \mathbf{J} \frac{d}{d\vartheta_e} \tilde{L}_s(\vartheta_e) \underline{\hat{i}}^s_{dq}(t) + \underline{\hat{i}}^{s\top}_{dq}(t) \mathbf{J}^\top \mathbf{J} \frac{d}{d\vartheta_e} \tilde{L}_{sr}(\vartheta_e) \underline{\hat{i}}^r_{dq}(t) \right) \Big] \end{aligned} \tag{3.20}$$

Equation (3.20) includes also terms which are not involved in the production of the torque disturbance. At this point, a first assumption can be stated. In the frequency range where the torque disturbance needs to be detected on-line, during standard operation of a PMSM, the currents are assumed sinusoidal in the stator reference frame and therefore almost stationary in the rotor reference frame. The latter is admissible and fairly achievable, by setting a proper bandwidth for the current controller. This means that energy fluctuation due to the $d-q$ current derivative $\frac{d}{dt} \underline{i}^s_{dq}$ in steady-state

is negligible. Further, for PMSM the rotor equivalent current $\underline{i}^r_{dq}$ is constant and the derivative null.
Therefore in steady-state holds

$$\hat{\underline{i}}^{s\top}_{dq}(t) L_s(\vartheta_e) \frac{d}{dt} \underline{i}^s_{dq} \sim 0 \tag{3.21a}$$

$$\hat{\underline{i}}^{s\top}_{dq}(t) L_{sr}(\vartheta_e) \frac{d}{dt} \underline{i}^r_{dq} \sim 0 \tag{3.21b}$$

Further, the stator reluctance component, namely $\hat{\underline{i}}^{s\top}_{dq}(t) \frac{d}{d\vartheta_e} \tilde{L}_s(\vartheta_e) \hat{\underline{i}}^{s\top}_{dq}(t)$, due to the position dependency of the inductance can be decomposed in two terms, representing half the contribution of the energy variation and half the electromagnetic torque pulsation. Thus, (3.20), considering also that $\mathbf{J}^\top \mathbf{J} = \mathbf{I}$, with $\mathbf{I} \in \mathbb{R}^2$ identity matrix, can be written as

$$\begin{aligned} \hat{P}_{dq}(\theta_e) = \frac{3}{2}\omega_e \Bigg[& \hat{\underline{i}}^{s\top}_{dq}(t) \mathbf{J} \underline{\lambda}^s_{dq}(\vartheta_e, \underline{i}^{sr}_{dq}) + \frac{1}{2} \hat{\underline{i}}^{s\top}_{dq}(t) \frac{d}{d\vartheta_e} \tilde{L}_s(\vartheta_e) \hat{\underline{i}}^s_{dq}(t) \\ & + \frac{1}{2} \hat{\underline{i}}^{s\top}_{dq}(t) \frac{d}{d\vartheta_e} \tilde{L}_s(\vartheta_e) \hat{\underline{i}}^s_{dq}(t) + \hat{\underline{i}}^{s\top}_{dq}(t) \frac{d}{d\vartheta_e} \tilde{L}_{sr}(\vartheta_e) \hat{\underline{i}}^r_{dq}(t) \Bigg] \end{aligned} \tag{3.22}$$

Dividing (3.22) by the mechanical speed, we obtain an estimation of the torque together with its harmonic disturbance, excluding the contribution of the cogging torque which is not captured by the stator electrical dynamics.
However, due to the fact that the pulsation of the magnetic energy and the mechanical output cannot be distinguished through the measurements, equation (3.22) approximate the exact torque expression (1.64) till a certain extent. Although this could appear as a limitation, in practice this depends to the target machine. Considering for example a surface-mounted PMSM, the air-gap reluctance and its position-dependency becomes almost negligible, therefore the harmonic distribution of the mutual flux component between stator and rotor term, namely $\frac{d}{d\vartheta_e} \tilde{L}_{sr}(\vartheta_e) \hat{\underline{i}}^r_{dq}$, is predominant and the estimation (3.22) is reliable. This is also a fair assumption for interior PMSM with a weak stator flux component, compared to the contribution of the rotor permanent magnets, which again empathizes the effect of the rotor flux to the torque harmonics generation. This observation is reinforced in the next section where different experimental proofs are given.
Finally, we are able to say that the estimated power computed by (3.17) represents a good approximation of the instantaneous electromagnetic power with its inherited disturbance.

3.2.3. Observer Performances Validation

In this section the LQO is implemented at the test-bench and validated on the PMSM. The algorithm has been tested with different horizon lengths and it has been found that horizon $N = 3$ on our hardware platform was a good compromise between accuracy and computational cost. In Tab. 3.1 the average execution time for different horizon length is shown. It has to been mentioned that the code has been optimized for a fast real-time execution. In particular, since the LQO solves an unconstrained problem, the exact solution is available by computing the inverse of the Hessian problem matrix

(3.16). The latter can be explicitly parametrized in order to avoid the usage of algebraic routines for computing it on-line. This reduces the estimation problem to a bunch of sum and products which makes the real-time execution quite fast. Moreover, it allows the adaptation of the PMSM model to different operative conditions, in particular the variation of the inductances with the electrical load.

Table 3.1: Average execution time of the LQ Observer

Horizon $[N]$	1	2	3
Time $[\mu s]$	5.8	9.4	17.3

In order to validate the estimation performances two type of tests are run:

1. Test in no load condition;
2. Test with machine under load.

The first experiment allows to estimate the machine BEMF, while from the second experiment an estimation of the torque ripple is achievable through the instantaneous power computation (3.17) scaled by the mechanical speed ω_r.
In Fig. 3.5 it is shown the behavior of the estimator for different factors of the regularization component, namely the matrix R in (3.11), which is assumed to have a fixed $\underline{r} = [\underline{r}_1 \dots \underline{r}_{N+1}]^\top$ value for the entire horizon. The motor is controlled with zero current references, therefore among all the non-sinusoidal component of the voltage disturbance (3.18), in no load condition only the one related to the rotor permanent magnets is present, namely

$$\underline{\hat{w}}_{dq}(\vartheta_e) = -\omega_e \left(\mathbf{J} \underline{\psi}^s_{dq} + \frac{d}{d\vartheta_e} \underline{\tilde{\psi}}^s_{dq}(\vartheta_e) \right) \tag{3.23}$$

where in accordance with the exposition of Sec. 1.3, the fictitious rotor electrical circuit which produces the flux at no load has been substituted by the equivalent permanent magnet flux such that $\underline{\psi}^s_{dq} = L_{sr} \underline{i}^r_{dq}$ and $\underline{\tilde{\psi}}^s_{dq} = \tilde{L}_{sr} \underline{i}^r_{dq}$ (see 1.53).
In Figure 3.5, the $d-q$ estimated BEMF is transformed in $\alpha - \beta$ and displayed for convenience. The result shows that excluding a regularization term in the cost function of the LQ Observer, namely the term $\Delta W^T R \Delta W$ in (3.11) exposes the estimation to a very high noise-to-signal ratio, making the output hardly useful.
However, with a slight increase of the penalty weight on the estimated voltage disturbance, the estimation becomes extremely robust to the noise and as it is possible to see in Fig. 3.5c, the function results highly correlated with the real motor BEMF shown in Fig. 1.23. Regarding the other weighting coefficients for the penalization matrices Q and S, the terms have been kept fixed and equal for the $d-q$ axis and the horizon length, respectively $\underline{q}_{ii} = 1$ for $i = 1 \dots \underline{q}_{N+1}$ and $\underline{s}_{ii} = 1e{-}3$ for $i = 1 \dots \underline{s}_{N+1}$. Finally, if the penalization becomes consistent as in Fig. 3.5d, all the harmonics are filtered out and the only fundamental is recovered.

For the second type of experiments, the machine has been loaded with various current set-points for validating the prediction under different electromagnetic conditions.

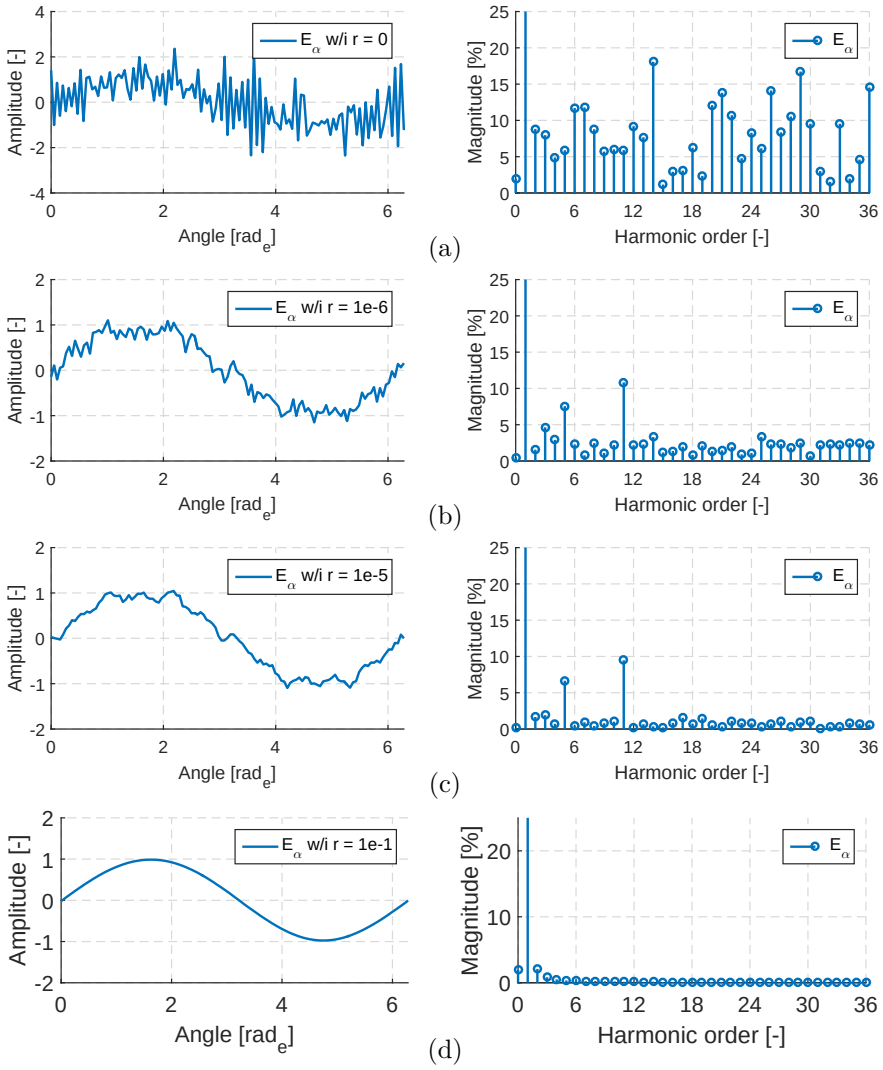

Figure 3.5: Estimation of the machine BEMF at no load condition, varying the regularization weighting coefficients in R for the disturbance. The resulting E_α is displayed normalized to its peak value.

It is made clear that the prediction model of the LQO is adapted in accordance with the magnetic characteristic available of the machine. In case the model (3.7) is kept constant to its nominal values, the estimation would lose accuracy in the prediction under high load current. Although the information of the iron saturation is necessary, since that we are dealing with a model-based control strategy, this is not completely a limitation, in fact this kind of advanced control features arise in particular contexts where the target application requires high precision; therefore, it is assumed that a sufficient magnetic saturation characteristic of the machine over its operation is available. In Fig. 3.6 the results are shown.

On the right, the estimation of the current is compared to the measured one in $d-q$. As the primary objective of the observer is to track the measured system state, the estimation appears perfectly overlapped to the measurement in all the four cases.

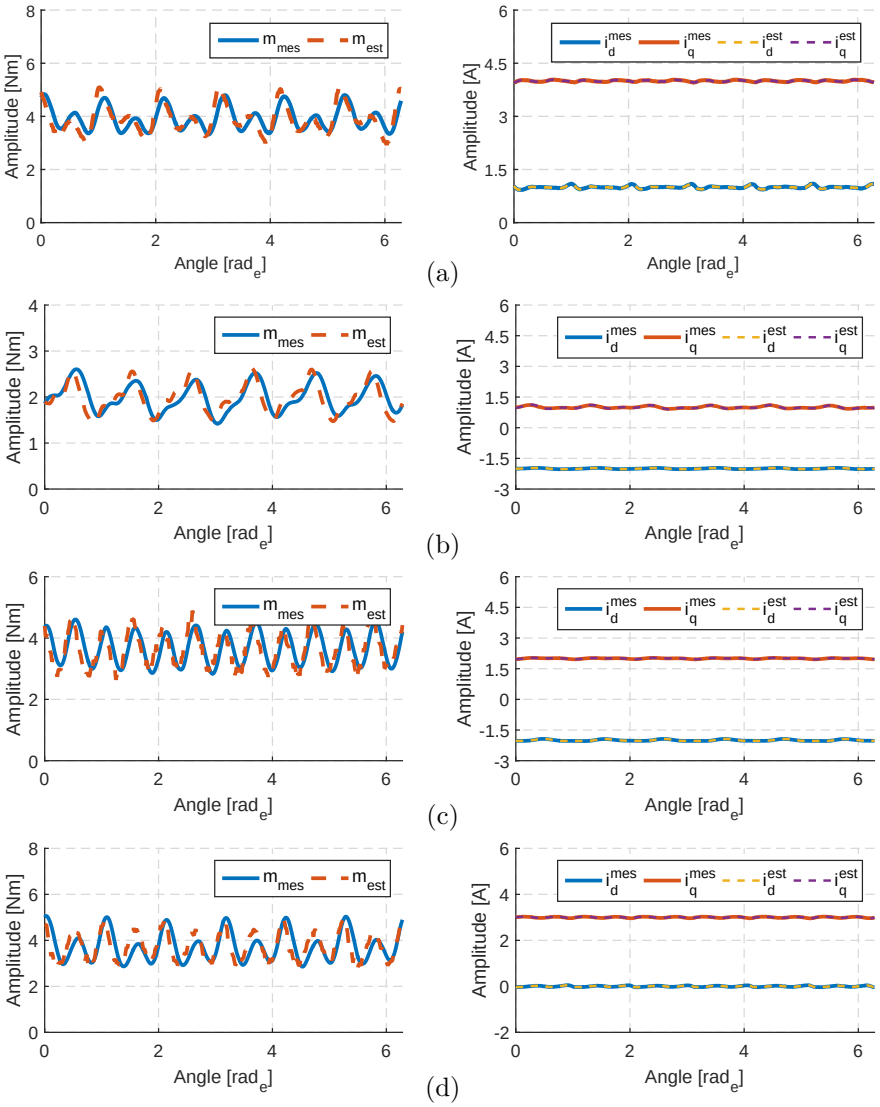

Figure 3.6: Estimation of the torque ripple via the instantaneous power computation with different current set-point at 100 *rpm*.

On the left-side of the figure, it is displayed the comparison between the estimated torque computed from the instantaneous power and the real measured torque via the sensor. In all the four load situations presented a good correlation between the two functions is obtained. As already noted the measured torque is affected by the cogging effect, which is not estimated.

3.3. Feedback Active Harmonic Injection

In the previous section, it has been shown how to potentially estimate the instantaneous PMSM voltage and torque disturbance. This procedure is part of the feed-back approach, in fact it has been exploited the indirect propagation of the source disturbance within the voltage and the current, in order to estimate the undesired pulsating component.
The estimated power (3.17), can be subsequently processed through an high pass filter (HPF) for getting rid of the mean value. The resulting signal is the undesired residual ripple quantity.
Forcing to smooth the estimated residual harmonics in the power (3.17), it results in reducing the machine torque disturbance, that is the desired harmonic cancellation. In what follow, a suitable method for the harmonic injection based on the estimated feed-back error will be designed.
In the literature, various different cancellation approaches can be found. A popular approach for general ANC tasks is given by the LMS-algorithm which is based on the idea of a broad-band noise disturbance cancellation by suitable input injection [72]. This configuration provides only limited attenuation over a restricted frequency range for periodic or band-limited noise. It also suffers from instability, because of the possibility of positive feedback at high frequencies. However, in our context where we are dealing specifically with narrow-band periodic disturbance harmonics, due to the predictable nature of the narrow-band signals, a more robust system that uses the estimated error from the LQ Observer to predict the reference input can be designed. In particular, the standard broad-band LMS can be filtered in order to be excited only on selective frequencies. The algorithm is briefly sketched in Fig. 3.7, referred in literature as the *Adaptive Notch Filter*. The single-frequency notch filter uses two adaptive weights and a synthetized sine and cosine digital carrier to cancel an undesired sinusoidal interference in the primary input [73]. The application of this technique to the active periodic noise control was proposed by Ziegler [74].

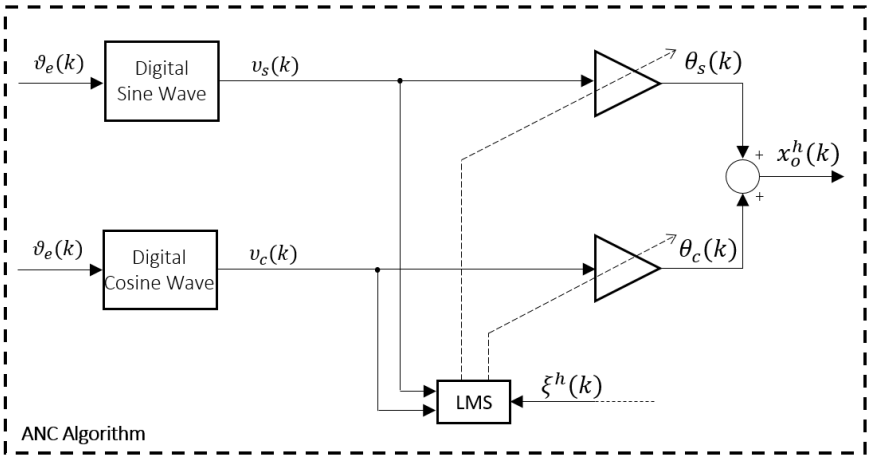

Figure 3.7: Block diagram of the adaptive notch filter.

Definition 3.3.1. *Let define a generic periodic quantity as*

$$x^h(t) = \underline{\upsilon}^\top(t)\underline{\theta}^x \tag{3.24}$$

with

$$\underline{\theta}^x = \begin{bmatrix}\theta_s \\ \theta_c\end{bmatrix} \qquad \underline{\upsilon}(t) = \begin{bmatrix}sin(\omega_h t) \\ cos(\omega_h t)\end{bmatrix} \tag{3.25}$$

where $\underline{\theta}^x \in \mathbb{R}^2$ represents the parameter space of the signal in which θ_s and θ_c are the magnitude respectively of the sine and cosine components, ω_h specifies the electrical angular speed of the harmonic order and $x^h(t) \in \mathbb{R}$ denotes the specific scalar magnitude considered.

The synthesized sine and cosine waves are synchronous and proportional to the order h of the fundamental electrical frequency. A discrete periodic error quantity $\xi(k)$ is introduced in the filter, where the sine wave is split into two orthogonal components, $\upsilon_s(k)$ and $\upsilon_c(k)$. These two reference signals are separately weighted and then summed to produce the compensation signal $x_o^h(k)$ as

$$x_o^h(k) = \theta_s(k)\upsilon_s(k) + \theta_c(k)\upsilon_c(k) \tag{3.26}$$

where

$$\begin{aligned}&\upsilon_s(k) = sin(6h\vartheta_e(k))\\ &\upsilon_c(k) = cos(6h\vartheta_e(k))\\ &\text{with } \{h \in \mathbb{N}^+ \mid 1 \leq h < +\infty\}\end{aligned}$$

The magnitude and the phase of this compensation signal are adjusted in the ANC controller, which feeds the inverter with a pulsating voltage serving as the control source to cancel the corresponding harmonic components. The LMS algorithm updates the filter weights to minimize the residual error ξ^h as follow

$$\underline{\theta}_o^x(k{+}1) = \underline{\theta}_o^x(k{+}) - 2\mu\xi^h(k)\underline{\upsilon}(k) \tag{3.27}$$

where μ is the factor that controls stability and rate of convergence.
From the block scheme in Fig. 3.7, the transfer function can be computed and a general example has been displayed in Fig. 3.8
The LMS algorithm estimates an instantaneous gradient in a crude but efficient manner by assuming that $(\xi^h)^2(k)$, the square of a single error sample, is an estimate of the mean-square error and by taking the derivative of $(\xi^h)^2(k)$ with respect to $\underline{\theta}_o^x$, the updating law is derived as (3.27).
The algorithm can be easily extended for multi-harmonic compensation by repeating in parallel the structure projected on different frequency domains. Although its simple structure, the stable convergence of the input error to zero is very sensitive to the system operating point and frequency. This issue increases the effort of tuning the learning rate μ, which can easily make the system unstable if it is chosen wrongly. A popular variation of the LMS is the FxLMS [72], for which again the error signal is projected onto harmonics similar to what is shown in Fig. 3.7, but it is also pre-filtered through the system dynamics. The latter helps to improve the convergence robustness, and the FxLMS algorithm is able to completely cancel harmonic components if the phase error in the estimated transfer function remains below $\frac{\pi}{2}$.

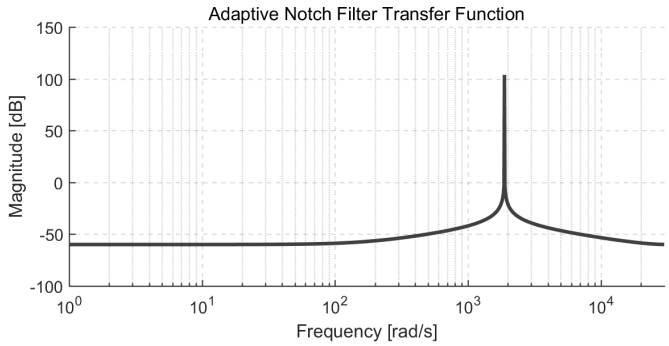

Figure 3.8: Magnitude response from the computed transfer function of the adaptive narrow-band filter. In the diagram the resonant frequency has been set at 300 Hz.

However, the rate of convergence remains strongly dependent from the harmonic frequency, therefore maintaining high the calibration effort.
Further, these algorithm LMS-based are applicable only on SISO system, which limits the applicability in our context, since that we are dealing with a MIMO system.

For the above mentioned reasons hereafter it is designed a more complex injection technique which combines model-based informations with optimality conditions and moreover decomposes the problem in two stages: first a set of harmonic current references is generated and then, the periodic voltage vector is calculated by mean of the direct current feed-back. This allows to accommodate MIMO systems and also enables a full degree of freedom on the injection angle.

3.3.1. Proposed Torque Ripple Compensation Technique

Current reference generation

The method proposed here subsequently focuses on the selective cancellation of specific harmonic orders within the electromagnetic torque. For this scope the mathematical treatment will consider only periodical functions for the magnitudes involved in the analysis as defined in Def. 3.3.1, namely the voltage $\underline{u}^h_{dq}(t)$, the current $\underline{i}^h_{dq}(t)$ and the torque $m^h(t)$. The latter can be seen as a superposition onto the nominal field-oriented control of a PMSM.
For this purpose the current-voltage relationship of the PMSM can be described in the frequency domain as shown in Fig. 3.9. The disturbance affecting the system can be modeled acting in different points of the path, in fact the physical effect may be either at the input, at the output or somewhere in between. However the control performance indicator is determined by a residual error objective of the harmonic cancellation algorithm. In what follows, the input-output equation can be written as

$$\begin{aligned} \underline{i}^h_{dq}(t) &= \mathrm{G}_P(j\omega_h)\left(\underline{u}^h_{dq}(t) + \underline{d}^h_{dq}(t)\right) \\ m^h(t) &= \mathrm{G}_M(j\omega_h)\left(\underline{i}^h_{dq}(t) + \underline{\lambda}^h_{dq}(t)\right) \end{aligned} \tag{3.28}$$

where the periodic disturbance term $\underline{d}^h_{dq}(t)$ has been modeled as an input variable, in the same way it was defined during the development of the PI Observer in Sec. 2.3 and

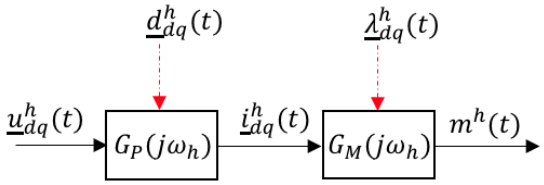

Figure 3.9: Input-Output transfer function with added disturbances for a general PMSM.

the LQ Observer in Sec. 3.2.1, while the flux harmonic disturbance $\underline{\lambda}^h_{dq}(t)$ affecting the torque has been considered at the output. The transfer function from the voltage to the current of the PMSM is $\mathrm{G}_P(j\omega_h)$ and the transfer function from the current to the electromagnetic torque is $\mathrm{G}_M(j\omega_h)$.
Further, in this context $\underline{d}^h_{dq}(t)$ represents exclusively the physical position dependent voltage disturbance of the PMSM, namely $\underline{d}^s_{dq}(\vartheta_e, \omega_e, \underline{i})$. In the case of torque harmonic compensation, the control objective is formulated as a tracking problem, in fact specific current harmonics are in general desired for achieving compensation of the torque disturbance. Therefore, an adaptation law need to be designed in order to obtain some specific periodic current references solution of the torque harmonic cancellation problem.
In general it is quite challenging to define a cause-effect transfer function from the current or the voltage to the torque frequency disturbance, in fact this would involve well-equipped test-bench platforms. Further, characterizing big size machines becomes even harder due to the high inertia. The latter procedure is at the basis of all the feed-forward methods. However hereafter simple model-based informations are exploited which are enough reliable for local approximation. In this context the ideal torque expression (1.66) can be exploited for producing some reference harmonic current which can be then used as a set-point for the voltage injection. For a general PMSM with reluctance torque component, there are two degrees of freedom which can influence the output torque, namely the $d-q$ currents, thus in practice the compensation of eventual torque periodic disturbance is an overdetermined problem.
Equation (1.66) can be thought as a predictor of the nominal torque together with its eventual pulsation. Althought it is a non linear function of the currents, the change of amplitude $m^h(t)$ due to a small harmonic current vector variations $i^h_d(t)$ and $i^h_q(t)$ can be approximated by linearizing (1.66) on the local operation as

$$m^h(t) = m^h_0(t) + \nabla^m_d(\underline{i}_{dq}) i^h_d(t) + \nabla^m_q(\underline{i}_{dq}) i^h_q(t) \tag{3.29}$$

where m^h_0 is the actual torque harmonic value.
The latter can be expanded in the parameter space, respectively the sine and cosine components as

$$m^h(t) = m^h_0(t) + S_1(t)^\top \nabla^m_{dq}(\underline{i}_{dq}) \underline{\theta}^i_{dq} \tag{3.30}$$

where ∇^m_d and ∇^m_q are respectively the local gradient of the torque expression (3.29), respectively for d and q components. The latter can be expanded in the parameter space, respectively the sine and cosine components as

$$m^h(t) = m^h_0(t) + \Upsilon_1(t)^\top \nabla^m_{dq}(\underline{i}_{dq}) \underline{\theta}^i_{dq} \tag{3.31}$$

for which $\Upsilon_1(t)^\top \in \mathbb{R}^{1\times 2p}$ is a matrix defined as

$$\Upsilon_1(t)^\top = \left[\underline{\upsilon}(t)_1^\top \dots \underline{\upsilon}(t)_{2p}^\top\right] \tag{3.32}$$

where $p \in \mathbb{N}^+$ represents the number of selected harmonics dimension (one for each state variable), thus the space of the projected sine and cosine harmonics components is equal to two times p.
The gradient $\nabla_{dq}^m \in \mathbb{R}^{2p\times 2p}$ is arranged in a diagonal form matrix such

$$\nabla_{dq}^m(\underline{i}_{dq}) = \begin{bmatrix} \frac{\partial m^h}{\partial \underline{\theta}_d^i} & & \\ & \ddots & \\ & & \frac{\partial m^h}{\partial \underline{\theta}_q^i} \end{bmatrix} \tag{3.33}$$

where $\frac{\partial m^h}{\partial \theta_d^i}$ and $\frac{\partial m^h}{\partial \theta_q^i}$ are the partial derivative respectively for the $d-q$ currents sine and cosine components, namely

$$\begin{aligned} \frac{\partial m^h}{\partial \underline{\theta}_d^i} &= K_r i_q^*(t)\cdot \mathbf{I} \\ \frac{\partial m^h}{\partial \underline{\theta}_q^i} &= K_r i_d^*(t)\cdot \mathbf{I} + K_s \cdot \mathbf{I} \end{aligned} \tag{3.34}$$

where $K_r = \frac{3}{2} z_p (L_{sd} - L_{sq})$ is the reluctance constant, $K_s = \frac{3}{2} z_p \Psi_{pm}$ is the synchronous constant, $i_d^*(t)$ and $i_q^*(t)$ are the set-point currents for the $d-q$ current driven into the machine and $\mathbf{I} \in \mathbb{R}^{p\times p}$ is the identity matrix.
Once a prediction of the torque input can be computed in function of the current components, it is then possible to formulate a quadratic problem (QP) which allows to obtain a gradient-based updating rule for the $d-q$ current components. The goal is to bring $m^h(t) \to 0$ for $t \to \infty$, but this weak formulation would not lead to a well-posed problem, therefore it is necessary to add a regularization term which scope is to minimize the norm of the current vector solution of the minimization problem. This term is defined as the one introduced in the LQ-Observer design (3.11), respecting Def. 3.2.1 and it performs the same function. The cost function can be formulated as

$$J(\underline{\theta}_{dq}^i) = \frac{1}{2}\|\underline{\theta}_{dq}^i\|_R^2 + \frac{1}{2}\|m^h(t)\|_2^2 \tag{3.35}$$

$R \in \mathbb{R}^{2p\times 2p}$ with $r_{ii} > 0$ for $i = 1\dots 2p$, is the regularization diagonal matrix which introduces a penalization of the $d-q$ axis harmonic components. In order to obtain an updating law for the current coefficients it is possible to take the gradient of the cost function, which is

$$\frac{\partial J(\underline{\theta}_{dq}^i)}{\partial \underline{\theta}_{dq}^i} = \underline{\theta}_{dq}^{i\top} R + m^{h\top}(t)\frac{\partial m^h(t)}{\partial \underline{\theta}_{dq}^i} \tag{3.36}$$

which from the linearized error equation (3.31) leads to

$$\begin{aligned} \frac{\partial J}{\partial \underline{\theta}_{dq}^i} &= \underline{\theta}_{dq}^{i\top} R + m^{h\top}(t)\Upsilon_1^\top(t)\nabla_{dq}^m \\ &= \underline{\theta}_{dq}^{i\top} R + \underline{\theta}_{dq}^{i\top}\nabla_{dq}^{m\top}\Upsilon_1(t)\Upsilon_1^\top(t)\nabla_{dq}^m + m_0^{h\top} S_1^\top(t)\nabla_{dq}^m \\ &= \underline{\theta}_{dq}^{i\top} H + b^\top \end{aligned} \tag{3.37}$$

with

$$\begin{aligned} \mathrm{H} &= \mathrm{R} + \mathrm{M} \\ \mathrm{M} &= \nabla_{dq}^{m\top} \Upsilon_1(t) \Upsilon_1^{\top}(t) \nabla_{dq}^{m} \\ b &= \nabla_{dq}^{m} \Upsilon_1(t) m_0^h(t) \end{aligned} \tag{3.38}$$

and $M \in \mathbb{R}^{2p \times 2p}$ is a symmetric matrix including all the quadratic convolution products between the partial derivatives of the parameter space, $b \in \mathbb{R}^{2p \times 1}$ is a real vector of the linear terms which depends directly from the input error $m_0^h(t)$ and $c \in \mathbb{R}$ is a constant. The time-derivative of the current coefficients, necessary to bring the periodic torque disturbance to zero, can be computed through the gradient of (3.35) taking the negative steepest-descent direction (3.37), yielding to the formula

$$\begin{aligned} \dot{\underline{\theta}}_{dq}^{i} &= -\rho_i \frac{\partial J(\underline{\theta}_{dq}^{i})}{\partial \underline{\theta}_{dq}^{i}} \\ &= -\rho_i \left(\mathrm{H} \underline{\theta}_{dq}^{i} + b \right) \end{aligned} \tag{3.39}$$

where $\rho_i \in \mathbb{R}^{+}$ is a learning coefficient for controlling the convergence of the algorithm. After the integration of (3.39) the reference $d-q$ harmonic currents are generated converting the updated coefficients to the time domain by multiplying them with $\underline{\upsilon}(t)$. Since the matrix H in (3.39) is guaranteed to be at least positive semi-definite, due to the perturbation coefficient offered by the regularization term R, the dynamics of (3.39) is stable. In general the convergence of the coefficients to their steady-state values is not guaranteed $\forall \rho_i > 0$, however some guidelines for the analysis of the system's stability can be given.
Let's first discretize the updating law as

$$\underline{\theta}_{dq}^{i}(k+1) = \underline{\theta}_{dq}^{i}(k) - \rho_i \left(\mathrm{H} \underline{\theta}_{dq}^{i}(k) + b \right) \tag{3.40}$$

which can be re-written in the following recurrent form

$$\underline{\theta}_{dq}^{i}(k+1) = \left(\mathbf{I} - \rho_i \mathrm{H} \right) \underline{\theta}_{dq}^{i}(k) - \rho_i b \tag{3.41}$$

This is a linear dynamic system, which will be stable if the eigenvalues of the matrix $\mathbf{I} - \rho_i \mathrm{H}$ are less than one in magnitude [75]. The eigenvalues of this matrix can be expressed in terms of the eigenvalues of the Hessian matrix H. Let $\left[\lambda_1, \lambda_2 \dots \lambda_{pq} \right]^{\top}$ and $\left[z_1, z_2 \dots z_{pq} \right]^{\top}$ be the eigenvalues and eigenvectors of the Hessian matrix. Then

$$\left[\mathbf{I} - \rho_i \mathrm{H} \right] z_j = z_j - \rho_i \mathrm{H} z_j = z_j - \rho_i \lambda_j z_j = \left(1 - \rho_i \lambda_j \right) z_j \tag{3.42}$$

where the index $j = 1, \dots, 2p$.
Therefore the eigenvectors of $\mathbf{I} - \rho_i \mathrm{H}$ correspond to the eigenvectors of H and the eigenvalues of $\mathbf{I} - \rho_i \mathrm{H}$ are $(1 - \rho_i \lambda_j)$. The condition to fulfill is the following

$$\mid (1 - \rho_i \lambda_j) < 1 \tag{3.43}$$

Therefore, the maximum stable learning rate can be deduced from (3.43) as

$$\rho_i < \frac{2}{\lambda_{max}} \tag{3.44}$$

In our case the eigenvalues of the system matrix H depend from several factors, including the machine parameters such as the inductances, the magnet flux and the pole pairs number. Considering these parameters fixed from the specific design of the machine under evaluation, the eigenvalues depends from the actual machine current, for which the linearized optimization problem (3.35) is obtained, namely i_d and i_q. In Fig. 3.10 the theoretical learning rate guaranteeing the stability of the updating gradient law is displayed. As the absolute magnitude of the current increases, the learning rate exponentially decreases. As a safety rule, the learning rate is choosen to be smaller than the required for the maximum current load of the machine, computing (3.44).

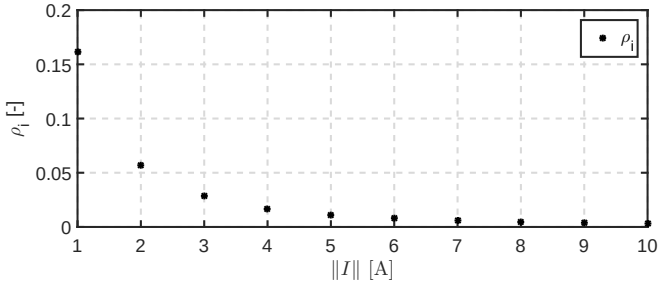

Figure 3.10: Maximum stable learning rate in function of the increasing machine current.

Voltage Reference Generation

The periodic current obtained from the updating law (3.39) can be directly used as a superimposed reference to the nominal current set-point. The latter would imply the design of an high bandwidth current control in order to track the harmonic reference [61]. In this context, it is desired to do not modify the structure of the main current control, but rather make use of model-based informations from the current to the voltage for generating the periodic voltage signal feed to the inverter. In the field of the active acoustic noise control different solutions have been already proposed in the last decades and a substantial contribution was made by M. Bodson [64]. The main idea is to determine and exploit the frequency response of the system when it is excited with specific harmonics and design a control law based on that information for rejecting eventual disturbance acting within the path [76]. For our purpose the goal is not to compensate the eventual disturbance in the current loop, namely $\underline{d}^s_{dq}(\vartheta_e, \omega_e, \underline{i})$, bringing the current ripple to zero, but rather to track a specific current harmonic profile. An error in the current closed-loop path can be written as follow

$$\begin{aligned} \underline{\xi}^h_{dq}(t) &= \underline{i}^{h*}_{dq}(t) - \underline{i}^h_{dq}(t) \\ &= \underline{i}^{h*}_{dq}(t) - \Upsilon_2(t)^\top \mathrm{G}_P(j\omega_h) \left(\underline{\theta}^u_{dq} + \underline{\theta}^d_{dq} \right) \end{aligned} \tag{3.45}$$

where $\underline{i}^{h*}_{dq}(t)$ is a general periodic current reference and $\Upsilon_2(t) \in \mathbb{R}^{p \times pq}$ is a matrix defined as

$$\Upsilon_2(t) = \begin{bmatrix} sin(\omega_h t) \cdot \mathbf{I} & cos(\omega_h t) \cdot \mathbf{I} \end{bmatrix}^\top \tag{3.46}$$

$\mathrm{G}_P(j\omega_h)$ is the voltage to current transfer function and it is computed from the state-space system (2.6) as follow

$$\mathrm{G}_P(j\omega_h) = (j\omega_h \mathbf{I} - \mathrm{A}_c)^{-1}\mathrm{B}_c \tag{3.47}$$

For a practical implementation (3.47) is written in accordance with the frequency parameter space of the voltage, $\underline{\theta}^u_{dq}$, as

$$\mathrm{G}_P(\omega_h) = \begin{bmatrix} \Re\{\mathrm{G}_P(j\omega_h)\} & -\Im\{\mathrm{G}_P(j\omega_h)\} \\ \Im\{\mathrm{G}_P(j\omega_h)\} & \Re\{\mathrm{G}_P(j\omega_h)\} \end{bmatrix} \tag{3.48}$$

Similar to what have been developed in Sec. 3.3.1, the error expression between the harmonic current set-point and the measured current (3.45) can be minimized through a quadratic problem. The cost function can be stated simply with the squared of the tracking error as

$$J(\underline{\theta}^u_{dq}) = \frac{1}{2}\|\underline{\xi}^h_{dq}(t)\|_2^2 \tag{3.49}$$

In this case an updating law can be derived solving again a quadratic optimal problem for finding the voltage coefficients which lead to the correct tracking of the reference one. The derived gradient-based updating law makes use of the inverse transfer function [77], in this case $\mathrm{G}_P^{-1}(j\omega_h)$ and can be written as follow

$$\dot{\underline{\theta}}^u_{dq} = \rho_u G_P^{-1}(\omega_h)\Upsilon_2(t)\underline{\xi}^h_{dq}(t) \tag{3.50}$$

The gradient (3.50) can be intuitively derived with a procedure similar to (3.37) and (3.39), where in this specific case the convergence factor ρ_u is normalized in order to produce an orthogonal gradient descent [78]. Knowing that for minimizing (3.49), the coefficients $\underline{\theta}^u_{dq}$ need to be updated in the direction of the negative gradient, namely $-\frac{\partial J(\underline{\theta}^u_{dq})}{\partial \underline{\theta}^u_{dq}}$, it is possible to write

$$\begin{aligned} \dot{\underline{\theta}}^{u\top}_{dq} &= -\rho_u \frac{\partial J(\underline{\theta}^u_{dq})}{\partial \underline{\theta}^u_{dq}} \\ &= -\rho_u \underline{\xi}^{h\top}_{dq}(t)\frac{\partial \underline{\xi}^h_{dq}(t)}{\partial \underline{\theta}^u_{dq}} \\ &= \rho_u \underline{\xi}^{h\top}_{dq}(t)\Upsilon_2(t)^\top \mathrm{G}_P(\omega_h) \end{aligned} \tag{3.51}$$

Taking the transpose and normalizing for the norm of $\mathrm{G}_P(j\omega_h)$, that is $\Re\{\mathrm{G}_P(\omega_h)\}^2 + \Im\{\mathrm{G}_P(\omega_h)\}^2$, (3.51) becomes

$$\begin{aligned} \dot{\underline{\theta}}^u_{dq} &= \rho_u \left(\mathrm{G}_P(\omega_h)^\top \mathrm{G}_P(\omega_h)\right)^{-1} \mathrm{G}_P(\omega_h)^\top \Upsilon_2(t)\underline{\xi}^h_{dq}(t) \\ &= \rho_u \mathrm{G}_P^{-1}(\omega_h)\Upsilon_2(t)\underline{\xi}^h_{dq}(t) \end{aligned} \tag{3.52}$$

Through the normalization of the gradient, a more robust version of the standard gradient law is obtained and its implementation is in general preferred [79]. The choice in our case has been also dictated by the fact that the algorithm is applied to a variable frequency drive, therefore the values of $\mathrm{G}_P(\omega_h)$ strongly depends from the time-variant nature of the harmonic frequencies and this affect the convergence of the updating law.

The latter effect can be reduced via normalization as per (3.52), limiting the sensitivity of the algorithm's convergence to the variable frequency. Although it requires the inversion of the system transfer function, the latter can be produced in advance and efficiently parametrized in the controller, leading to a low computational effort per each sampling time [80]. As per (3.39) an adaptation learning rate is defined as $\rho_u \in \mathbb{R}^+$. However in this case, it has been extensively shown that for values of ρ_u small enough, a sufficient condition for the stability requires that $\mathrm{G}_P(j\omega_h)$ is minimum phase at the selected frequencies [64]. Since the transfer function $\mathrm{G}_P(j\omega_h)$ of a PMSM has its poles on the left-half s-plane, namely $\Re\{\mathrm{G}_P(j\omega_h)\} > 0$, its inverse is also stable and this condition satisfies the minimum phase criteria.

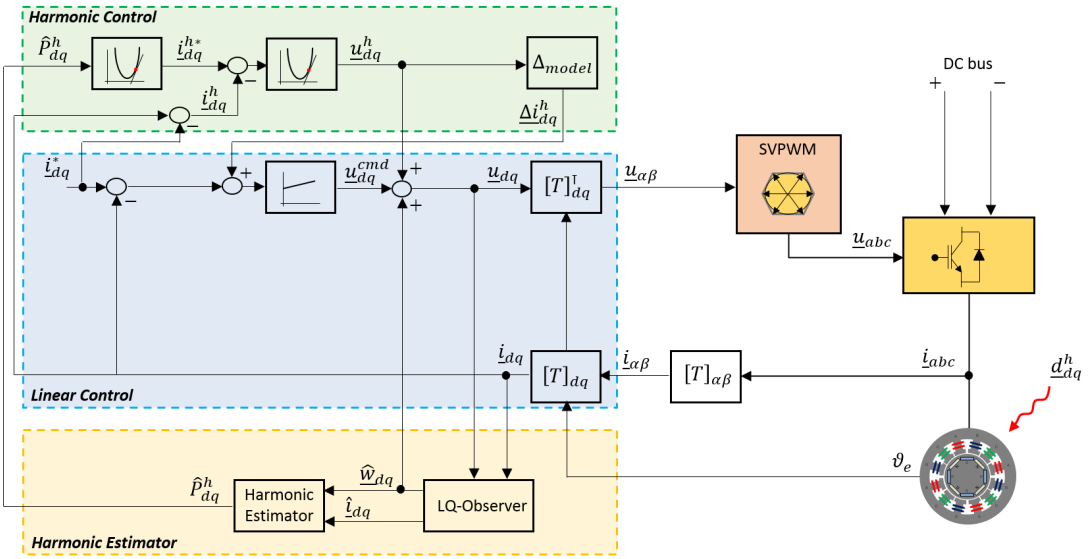

Figure 3.11: Overall control strategy.

3.3.2. Overall Harmonic Controller

The presented algorithms in Sec. 3.3.1 and 3.3.1 are embedded within a linear PMSM controller. The overall control strategy is shown in Fig. 3.11. The linear control is constituted by two simple PI and provides the tracking of the reference currents. In parallel the harmonic controller provides active compensation features for selected frequencies. The input for the harmonic control is a known pulsating quantity related to the flux disturbance at the torque level. The latter is estimated directly from the LQ Observer. The first gradient-based block uses the linearized torque prediction model (3.31) for producing a $d-q$ harmonic current vector which is subsequently passed to the inner current harmonic tracking controller. The latter, based on the information provided by the modeled transfer function of the PMSM generates harmonic voltages which are added to the nominal commanded voltage as a compensation signal. Both the current and voltage harmonic generators are formulated in order to act on a selected number of harmonics, which need to be specified during the synthesis of the controller. A general block scheme of the harmonic controller is represented in Fig. 3.13. The harmonic error quantity, namely the torque or the current, is projected on the specific harmonic

reference frame and after the computation of the gradient, the coefficients are updated through integration. A simple $sin(\omega_h t)$ and $cos(\omega_h t)$ multiplication is repeated for converting back the coefficients in the time domain. Further, from the harmonic estimator block it is extracted also the harmonic voltage disturbance effecting the voltage, namely $\underline{w}^h_{dq}$, which represents the residual position-dependent term introduced in (1.55). This quantity is added to the inverter voltage $\underline{u}_{dq}$. Neglecting system delays and saturation effects, than $\underline{w}^h_{dq}(t) = -\underline{d}^h_{dq}(t)$, therefore the voltage disturbance is effectively decoupled and the voltage harmonic controller, which is based on the linear transfer function $\mathrm{G}_P(j\omega_h)$ exactly represents the frequency behavior of the PMSM without added source of disturbance. Finally, The so-called Δ-*model* is necessary for decoupling the harmonic control action from the nominal one, in fact since both controllers act on the same path, an unavoidable competition arises between them if this effect is not considered. For this reason a nominal model of the PMSM based on the state-space formulation (1.70) of the PMSM is implemented leaving apart the term associated to the rotor flux, namely $E_c(t)$. The continuous state-space form is:

$$\underline{\Delta \dot{i}}^h_{dq}(t) = A_\Delta \underline{\Delta i}^h_{dq}(t) + B_\Delta \underline{u}^h_{dq}(t) \tag{3.53}$$

where

$$\mathrm{A}_\Delta = \begin{bmatrix} -\frac{R_s}{L_{sd}} & \omega_e \frac{L_{sq}}{L_{sd}} \\ -\omega_e \frac{L_{sd}}{L_{sq}} & -\frac{R_s}{L_{sq}} \end{bmatrix}, \quad \mathrm{B}_\Delta = \begin{bmatrix} \frac{1}{L_{sd}} & 0 \\ 0 & \frac{1}{L_{sq}} \end{bmatrix} \tag{3.54}$$

During the discretization of (3.53), the electrical angular speed is assumed slow-varying, thus piecewise constant for the duration of the sampling.

Definition 3.3.2. *Let the Δ-model transfer function be computed from* (3.53)*, namely* $\mathrm{G}_\Delta(s) = (s\mathbf{I} - \mathrm{A}_\Delta)^{-1}\mathrm{B}_\Delta$*. The predicted $\Delta i^h_{dq}(t)$ is added to the reference current of the linear controller input such that the harmonic injection is analytically decoupled and the main control does not react against it.*

Proof. The latter can be proved analyzing the closed-loop path between the linear and the harmonic controller. A simplified block scheme is shown in Fig. 3.12, where the various blocks are represented by a transfer function term. In particular, G_Δ represents equation (3.53), R_{foc} represents the transfer function of a general linear PI field-oriented controller and R_{hrm} stays for the gradient-based law of (3.50). For simplification the measurement noise has been ignored, so that it holds $\underline{i}_{dq} \equiv \underline{i}^m_{dq}$. From the representation of Fig. 3.12, it follows

$$\begin{aligned} \underline{\xi}^i_{dq}(s) &= \underline{i}^*_{dq}(s) - \underline{i}_{dq}(s) + \underline{\Delta i}^h_{dq}(s) \\ &= \underline{i}^*_{dq}(s) - \mathrm{G}_P(s)\underline{u}_{dq}(s) + \underline{\Delta i}^h_{dq}(s) - \mathrm{G}_P(s)\underline{d}^h_{dq}(s) \\ &= \underline{i}^r_{dq}(s) - \mathrm{G}_P(s)\underline{u}^{cmd}_{dq}(s) - \mathrm{G}_P(s)\underline{\hat{w}}^h_{dq}(s) - \mathrm{G}_P(s)\underline{u}^h_{dq}(s) + \mathrm{G}_\Delta(s)\underline{u}^h_{dq}(s) - \mathrm{G}_P(s)\underline{d}^h_{dq}(s) \end{aligned} \tag{3.55}$$

Under the assumption $\underline{\hat{w}}^h_{dq} = -\underline{d}^h_{dq}(s)$ and thus, of the perfect knowledge of the system ($\mathrm{G}_\Delta \equiv \mathrm{G}_P$), this yields

$$\underline{\xi}^i_{dq}(s) = \underline{i}^*_{dq}(s) - \mathrm{R}_{foc}(s)\mathrm{G}_P(s)\underline{\xi}^i_{dq} \tag{3.56}$$

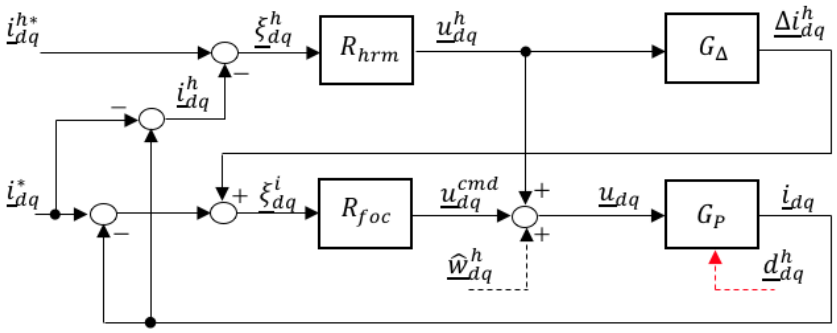

Figure 3.12: Inner harmonic control block scheme.

and finally re-arranging the equation

$$\underline{\xi}^{i}_{dq}(s) = \left(\mathbf{I} + \mathrm{R}_{foc}(s)\mathrm{G}_P(s)\right)^{-1} \underline{i}^{*}_{dq}(s) \tag{3.57}$$

From (3.57) it is evident that the harmonic control does not appear in the linear control input, hence the nominal control behavior is not influenced and the decoupling between the two elements is achieved. □

The reader should notice that at this point, in case pre-calculated current harmonics are known, it is possible to implement only the inner harmonic block for tracking the specified references, namely $\underline{i}^{h*}_{dq}(s)$ saving the hardware resources for the computation of the $d-q$ currents. Or, further, in case the objective is to suppress specific current harmonics, the desired current reference wil be set to zero. Finally, the extension to multi-harmonic compensation follows straightforward.

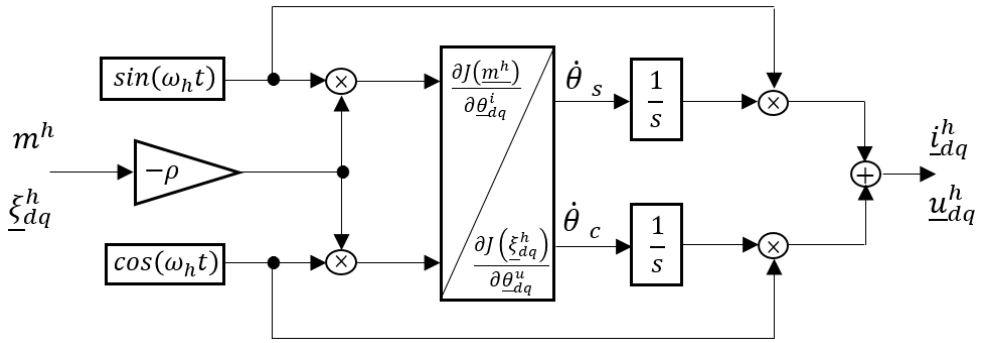

Figure 3.13: Harmonic compensation gradient-based for the update of the sine and cosine coefficients.

3.3.3. Experimental Validation

For the digital implementation of the controller the field oriented control is composed of a standard PI controller for the $d-q$ axis. The linear PI controller gains have been assigned respectively as follow: $K_p^{PI,d} = 65$, $K_i^{PI,d} = 6300$, $K_p^{PI,q} = 45$, $K_i^{PI,q} = 5800$. The harmonic controller is designed on the basis of the BEMF frequency spectrum of the PMSM, therefore the selective gradient-based algorithms are constructed incorporating respectively the 6^{th} and the 12^{th} harmonic orders. Similar to the procedure used for the experimental validation of the LQ-Observer, both the gradient-based algorithms resumed in Fig. 3.13, have been parametrized efficiently, reducing the computational effort to elementary calculations. The position is gathered through an incremental encoder and before it is processed within the controller a single-step delay compensation is performed in order to reduce the position uncertainty for the harmonic control blocks. Finally, the convergence tuning factors ρ_i and ρ_u have been chosen respectively as $1e{-}3$ and $1e{-}5$.

Hereafter, the steady-state performances of the proposed cancellation algorithm are analyzed. The selected current set-point lies on the MTPA of the motor and the $d-q$ currents are respectively $-1.7\ A$ and $3\ A$. The measurement is repeated loading the machine at 100 rpm and 200 rpm. The results are presented in Fig. 3.14 and Fig. 3.15. The figures are organized as follow: at the top and the center the measured torque at the shaft and the 3-phase currents are displayed together with its frequency spectrum decomposition; at the bottom the $d-q$ currents and voltages are reported. All the magnitudes are shown related to the fundamental electrical period.

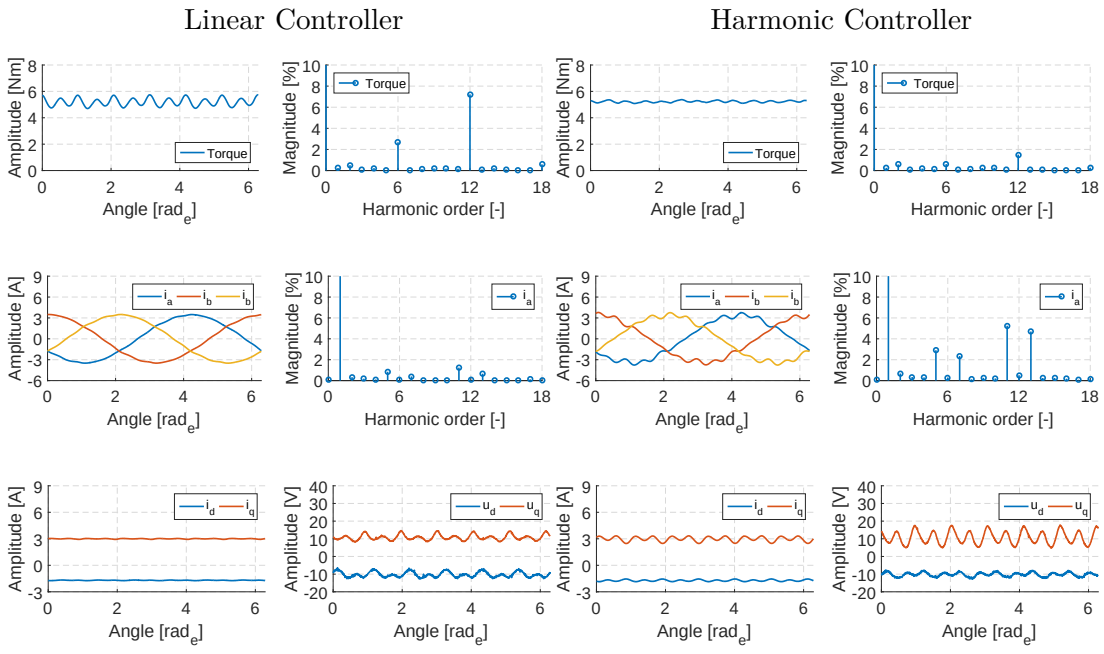

(a) (b)

Figure 3.14: Steady-state performances of the linear and harmonic controller at 100 rpm.

In Fig. 3.14a the machine is controlled for tracking the constant reference currents, therefore the PI controller tends to reject the voltage disturbance $\underline{\theta}^{d}_{dq}$, driving into the machine almost sinusoidal currents and the torque clearly shows an inherent 6^{th} and 12^{th} order pulsating harmonics. The latter are produced by the non ideal flux distribution at the air-gap described in Sec. 1.3.2.

Fig. 3.14b at the contrary shows the steady-state behavior after the harmonic injection algorithm has been activated. As result, torque harmonics have been mostly corrected through the gradient-based re-shaping of the currents. A substantial increment of the 5^{th}, 7^{th}, 11^{th}, 13^{th} harmonic orders in the current is necessary for achieving the compensation of the torque harmonics. As a consequence, it follows a strong harmonic effort for the commanded voltage which scales with ω_h. The latter is due to the fact that the transfer function of a PMSM behaves as an integrator, therefore the harmonics in the commanded voltage are proportional to the derivative of the harmonics in the current. This is directly understandable from the measurement set obtained at 200 *rpm*. In Fig. 3.15a a similar situation of Fig. 3.14a si reported.

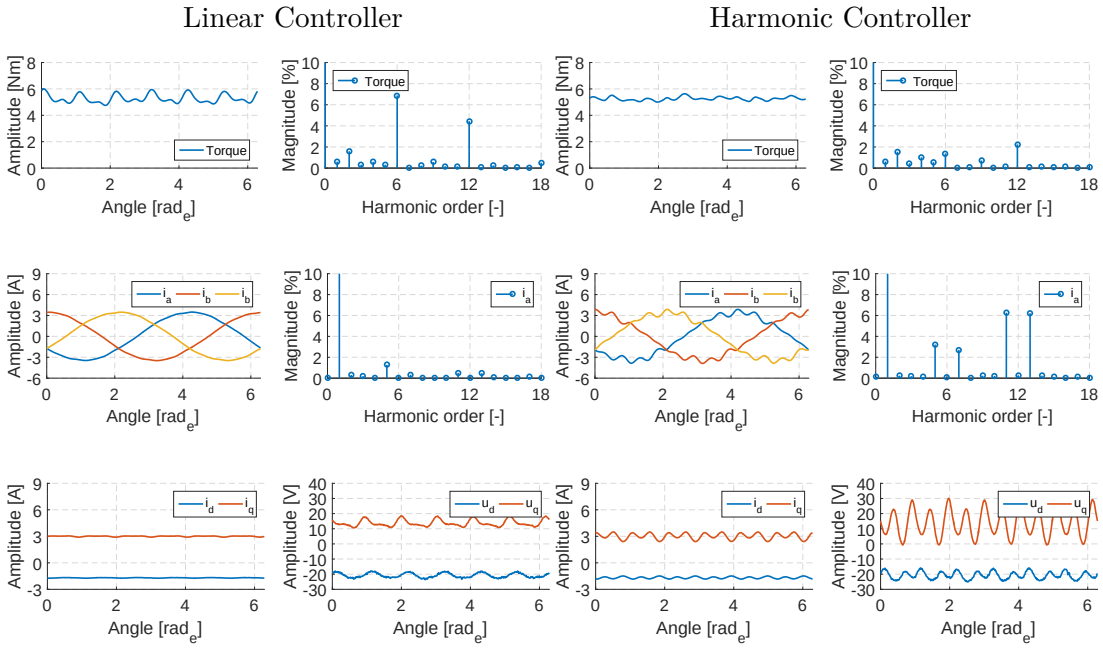

(a) (b)

Figure 3.15: Steady-state performances of the linear and harmonic controller at 200 *rpm*.

Even if the trend of the measured torque over the electrical period appears quite different, this is due to the fact that (*i*) as the speed is closer to zero, the cogging effect appears stronger and (*ii*) the low bandwidth of the torque sensor leads to eventual distortion in the measurements. However, from Fig. 3.15b we see that the level of torque harmonic suppression achieved is close to the one at lower speed and the current spectrum after the injection is very similar. At confirmation of the previous consideration on the voltage, although the current solution of the torque ripple minimization problem is almost identical, the bottom-right picture of Fig. 3.15b shows how

the rotating voltage vector overlapped to the nominal commanded voltage is strongly increased. The latter can be further analyzed in Fig. 3.16 where the currents and voltages are displayed in the $\alpha - \beta$ plane. Although appears a slight variation in the rotation of the injection for the currents, the amplitude is identical either at 100 rpm and 200 rpm. At the contrary, the rotating voltage vector increases in its amplitude.

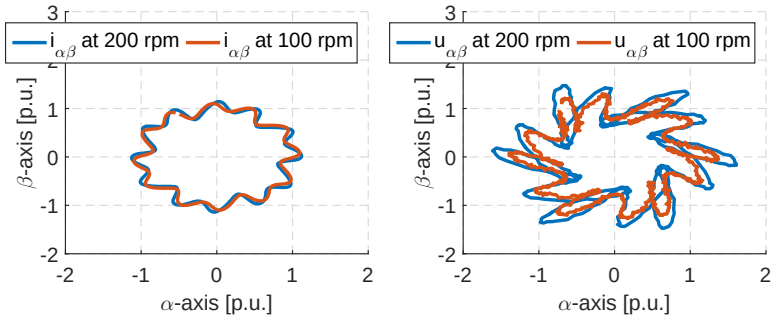

Figure 3.16: Comparison of the current trajectory and voltage trajectory in the $\alpha - \beta$ plane after the injection, respectively at 100 rpm and 200 rpm.

In Fig. 3.17 and Fig. 3.18 other two steady-state experiments follow. In particular, in Fig. 3.17 the current is driven exclusively on the $q - axis$, while in Fig. 3.18 a preponderant component of the $d - axis$ is imposed with the main controller. It is interesting to notice the solution of the currents determined by the algorithm after the injection: in the first case, due to the fact that the current is driven only in quadrature (i.e. negligible reluctance torque component), it needs to fully counteract the harmonic produced by the rotor flux, so that their combination leads to a smooth torque development over the electrical period. Therefore, the current harmonics are empathized by this particular load operation of the motor. In the second case, instead, the PMSM is operated with a consistent amount of the reluctance torque (around 30% of the total torque). Therefore the current harmonic injection is produced such that the combination of both the reluctance and the synchronous torque lead to a minimum pulsation of the resulting electromagnetic moment. The fact that a certain amount of reluctance torque is present, induces us to observe that the current harmonic effort is notably reduced (see Fig 3.18b) . The latter can be intuitively derived considering that the reluctance torque depends directly from the product of the $d - q$ currents (1.47) and sinusoidal currents will let this torque component to be constant over an electrical period.
Thus, it is legitimate to consider that the harmonic controller applies a reduced amount of current harmonics as a solution for the torque harmonic compensation. Later in the thesis, this concept will be further leveraged and validated.
Nevertheless, position dependency of the stator inductances, namely $\frac{d}{d\vartheta_e}\tilde{L}_s(\vartheta_e)$ and the cross-magnetization effect contributes to a small residual ripple even if the machine would be driven with a perfectly constant $d - axis$ current.

As further experimental test, the convergence performances of the algorithm are tested. In Fig. 3.19 it is shown the transient behavior of the torque harmonic compensation related to the experiment shown in Fig. 3.15. The algorithm is activated at $t = 0$ and it takes around ~ 600 ms to asymptotically settle in steady-state, which

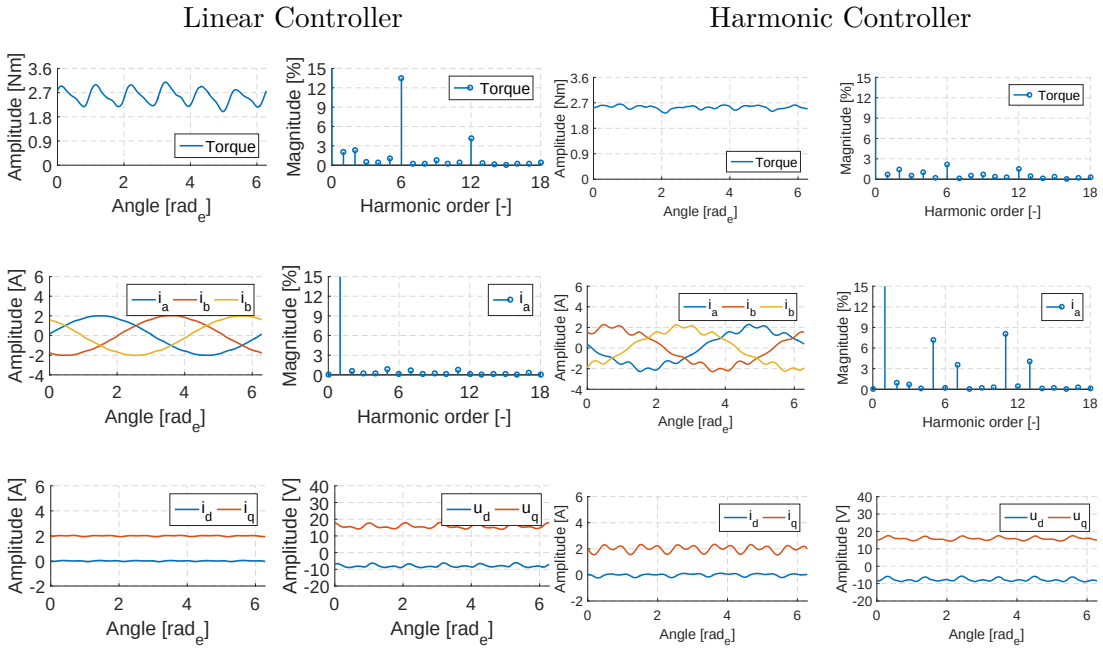

(a) (b)

Figure 3.17: Steady-state performances of the linear and harmonic controller at 100 rpm, with $i_d = 0\ A$ and $i_q = 2\ A$.

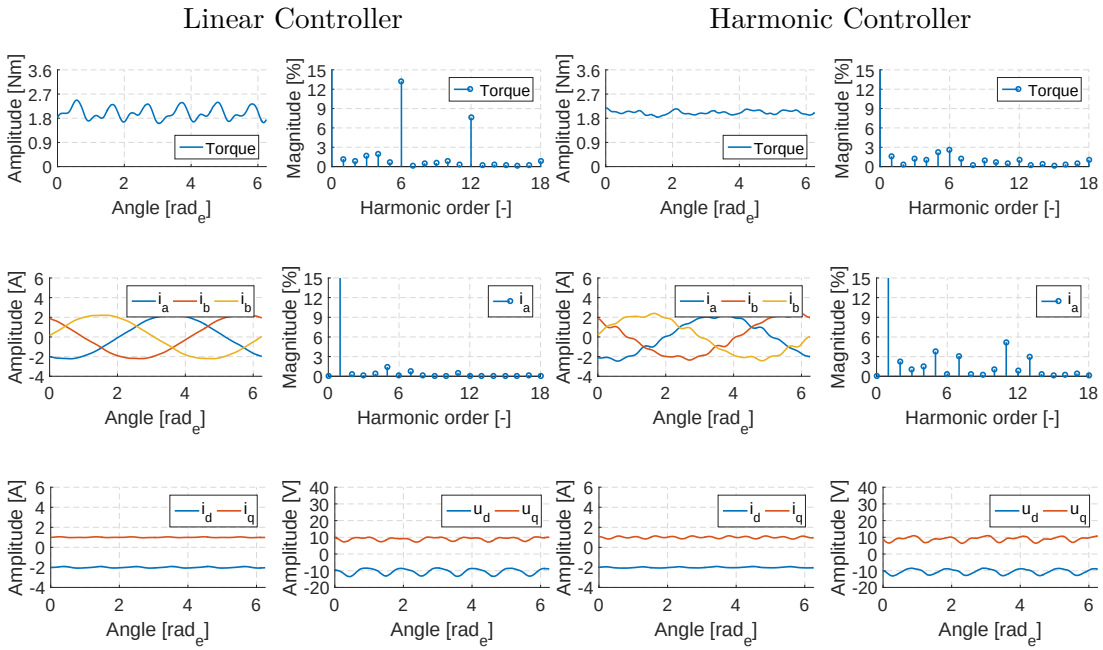

(a) (b)

Figure 3.18: Steady-state performances of the linear and harmonic controller at 100 rpm, with $i_d = -2\ A$ and $i_q = 1\ A$.

seems a satisfactory time. In particular, in order to validate the capability of the first

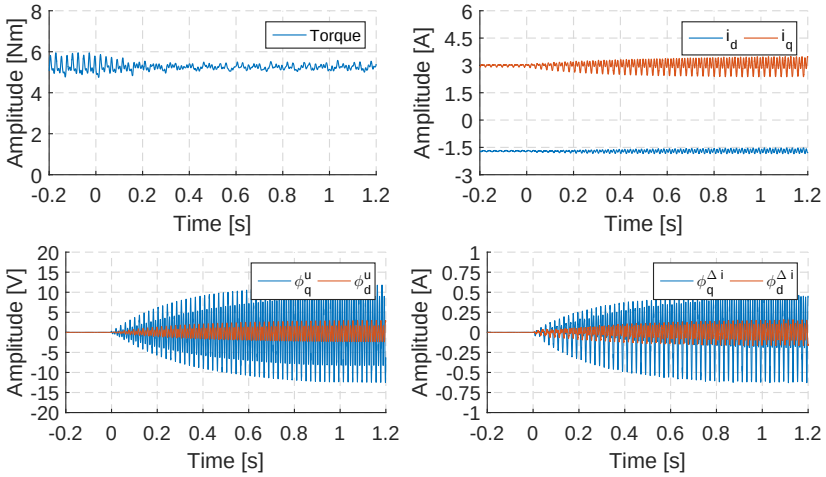

Figure 3.19: Test bed measurement for the transient behavior with the compensation of the 6^{th} and the 12^{th} order at 200 rpm. Compensation algorithm activated at $t = 0$.

minimization algorithm (3.39) to control the injection on the $d-q$ axis, producing different set of $d-q$ harmonic reference currents, the regularization weights of matrix R are designed both symmetrical and asymmetrical. The motor is run at 100 rpm and the $d-q$ current set-points are respectively -1 A and 2.6 A. The results are presented in Fig. 3.20. The penalization weights of matrix R are equally chosen for the 6^{th} and 12^{th} harmonic and varied respectively for the $d-q$ axis; in particular in Fig. 3.20a they are set to 1 for both axis, while in Fig. 3.20b and Fig. 3.20c they are displaced in a ration 1 to 20 respectively for the d-axis and for the q-axis. As expected, the injection is achieved exciting both or only a single axis. Consequently, the harmonic voltage follows a similar behavior and therefore this fact gives the opportunity to direct the injection for coping with eventual current or voltage constraints.

Finally, in Fig. 3.21 the update of the coefficients for the test case of Fig. 3.20a are reported during activation and transient of the algorithms. They are composed of sine and cosine magnitudes of the 6^{th} and 12^{th} harmonic for the $d-q$ axis currents. After an initial overshoot they settle down asymptotically to their optimal values. The coefficients are fed to the inner current harmonic algorithms for forcing the current to track the resulting references obtained by the outer loop.

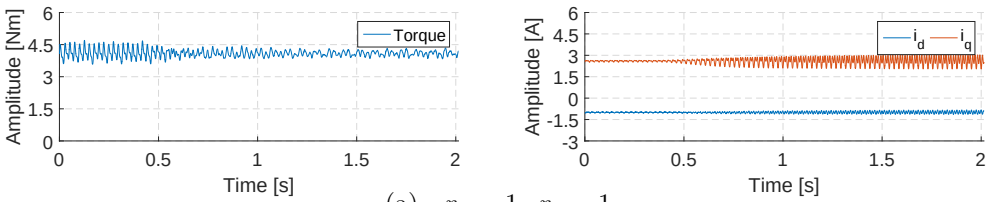

(a) - $r_d = 1,\ r_q = 1$

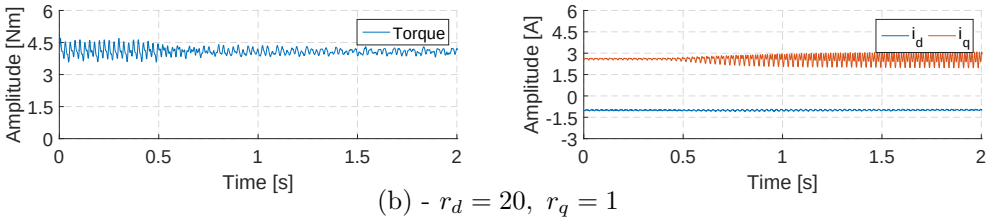

(b) - $r_d = 20,\ r_q = 1$

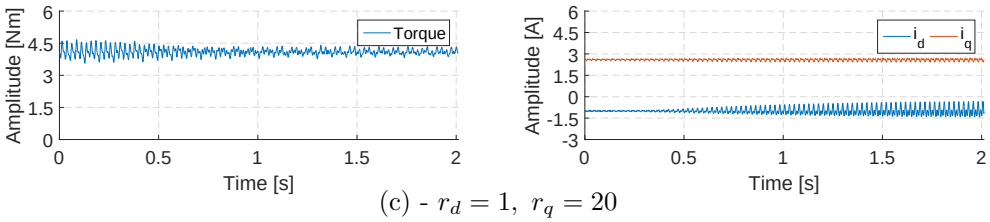

(c) - $r_d = 1,\ r_q = 20$

Figure 3.20: Transient behavior of the proposed algorithm, with symmetric and asymmetric regularization of the the sine and cosine components respectively for the $d-q$ axis.

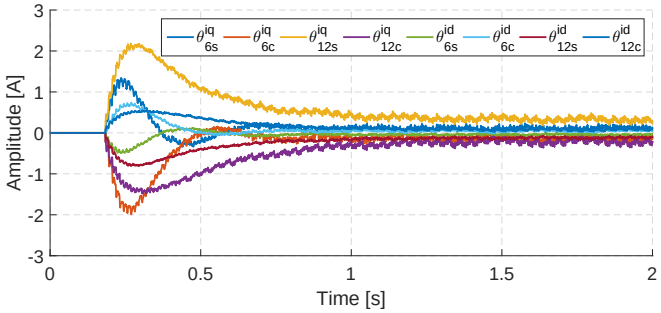

Figure 3.21: Convergence of the sine and cosine current harmonic coefficients during injection activation respectively of the $d-q$ axis.

3.4. Feedforward Harmonic Injection

In this section, differently from what has been shown in the previous argumentation on the feedback method, it will be introduced a technique for fulfilling the same objective of harmonic disturbance compensation. The whole reasoning is developed off-line and the information obtained are implemented on-line in the form of LookUp-Tables (LUTs). As it has briefly introduced in the introduction of Cap. 3, the feed-forward disturbance compensation methods are developed around direct observation of the quantities of interest, therefore the periodic disturbance is defined and known, so that a compensating action can be directly synthesized. The methodology proposed hereafter has been motivated by few fact observed during the experimentations of the feed-back algorithms proposed in Sec. 3.3. In particular, among the various position-dependent terms contributing to the torque periodic ripple, the major contribution is offered by the rotor magnets flux. The latter is notable from the experiment of Fig. 3.17, for which it was recorded the highest current harmonic injection. As far as the machine is driven with higher reluctance torque contribution compared to the synchronous one, the required currents tend to be more sinusoidal. This considerations stresses out two facts:

- Considering an SPMSM, when the machine is loaded on the q-axis, focusing on the compensation of the synchronous torque disturbance component, namely $\hat{\underline{i}}_{dq}^{s\top}(t)\frac{d}{d\vartheta_e}\tilde{\underline{\psi}}_{dq}^{s}(\vartheta_e)$, leads to a substantial improvement of the undesired position-dependency of the electromagnetic torque.
- Considering an IPMSM, when the machine is driven aside the q-axis, fulfilling the compensation of the torque disturbance components translates in less harmonic effort, in fact the term $\hat{\underline{i}}_{dq}^{s\top}(t)\mathbf{J}\underline{\lambda}_{dq}^{s}(\vartheta_e, \underline{i}_{dq}^{sr})$ gains relevance and it requires itself more sinusoidal currents in order to compensate its motional component, as it has been observed from Fig. 3.18.

The issue with the feed-back method is that the estimated periodic disturbance of the torque, associated respectively with the synchronous and reluctance components, is represented by the combination of both the effects, therefore distinction is lost and the current harmonics are shaped on-line in accordance with the load condition of the machine. But the two phenomenons can be also threated separately allowing generalization on the basis of few machine informations and since superposition of effects holds true, combining the resulting compensation obtained either for the synchronous torque and the reluctance torque, the very same torque disturbance correction is obtained. This analysis is what has motivated the design of the methodology presented hereafter.

3.4.1. Sin^2 - Cos^2 Method

Let consider an SPMSM, that is a machine which has negligible reluctance effect and $L_{sd} \equiv L_{sq}$. This type of machine is typically driven on the q-axis, in fact in order to obtain the maximum torque per ampere the phase currents and the magnetic field produced by the rotor magnets are at $\frac{\pi}{2}$. From the power expression involved in the electromagnetic torque production (3.22) neglecting periodic disturbance terms related to the self-inductance, namely $\tilde{L}_{sd} \equiv \tilde{L}_{sq} = 0$ and to the mutual inductance, namely $\tilde{L}_{sd,sq} \equiv \tilde{L}_{sq,sd} = 0$, it is possible to write

$$P_{me}(\vartheta_e, \underline{i}^{sr}_{dq}) = \frac{3}{2}\left(\omega_e\, \hat{\underline{i}}^{s\top}_{dq}(t)\mathbf{J}\underline{\psi}^{s}_{dq} + \omega_e\, \hat{\underline{i}}^{s\top}_{dq}(t)\frac{d}{d\vartheta_e}\tilde{\underline{\psi}}^{s}_{dq}(\vartheta_e)\right) \tag{3.58}$$

Eq. (3.58) is expressed in the $d-q$ domain, thus it is not determined by real physical quantities, but rather transformed one. In order to gather clarity in the reasoning, the equation can be equivalently expressed in stator coordinates, applying the inverse Park transformation as follow

$$P_{me}(\vartheta_e, \underline{i}^{sr}_{dq}) = \frac{3}{2}\left(\omega_e\, \hat{\underline{i}}^{s\top}_{dq}(t)\,[\mathrm{T}]_{dq}\,\mathbf{J}\,[\mathrm{T}]^{\top}_{dq}\,\underline{\psi}^{s}_{dq} + \omega_e\, \hat{\underline{i}}^{s\top}_{dq}(t)\,[\mathrm{T}]_{dq}\,\frac{d}{d\vartheta_e}\tilde{\underline{\psi}}^{s}_{dq}(\vartheta_e)\right) \tag{3.59}$$

Knowing that $\omega_e \frac{d}{d\vartheta_e}\underline{\psi}^{s}_{dq}(\vartheta_e) = \frac{d}{dt}\underline{\psi}^{s}_{dq}(t)$, equation 3.59 can be further developed as

$$\begin{aligned} P_{me}(\vartheta_e, \underline{i}^{sr}_{dq}) &= \frac{3}{2}\left(\omega_e\, \hat{\underline{i}}^{s\top}_{dq}(t)\,[\mathrm{T}]_{dq}\,\mathbf{J}\,[\mathrm{T}]^{\top}_{dq}\,\underline{\psi}^{s}_{dq} + \hat{\underline{i}}^{s\top}_{dq}(t)\,[\mathrm{T}]_{dq}\,\frac{d}{dt}\underline{\psi}^{s}_{dq}(t)\right) \\ &= \frac{3}{2}\left(\omega_e\, \hat{\underline{i}}^{s\top}_{dq}(t)\,[\mathrm{T}]_{dq}\,\mathbf{J}\,[\mathrm{T}]^{\top}_{dq}\,\underline{\psi}^{s}_{dq} + \hat{\underline{i}}^{s\top}_{dq}(t)\,[\mathrm{T}]_{dq}\,\frac{d}{dt}\,[\mathrm{T}]^{\top}_{dq}\,\underline{\psi}^{s}_{dq}(t)\right) \end{aligned} \tag{3.60}$$

Transforming the current to the $\alpha-\beta$ system and re-arranging, it is possible to write

$$P_{me}(t) = \frac{3}{2}\underline{i}^{\top}_{\alpha\beta}(t)\,[\mathrm{T}]^{\top}_{dq}\left(\omega_e\mathbf{J}\underline{\psi}^{s}_{dq} + \frac{d}{dt}\underline{\psi}^{s}_{dq}(t)\right) \tag{3.61}$$

Definition 3.4.1. *Let $\underline{\psi}^{s}_{dq}(t)$ be the stator flux contribution due to the rotor magnets in the synchronous rotating reference frame and $\underline{\psi}_{\alpha\beta}(t)$ its counterpart in the stationary reference frame. It holds that*

$$\frac{d}{dt}\underline{\psi}_{\alpha\beta}(t) = [\mathrm{T}]^{\top}_{dq}\left(\omega_e\mathbf{J}\underline{\psi}^{s}_{dq} + \frac{d}{dt}\underline{\psi}^{s}_{dq}(\vartheta_e)\right) \tag{3.62}$$

Proof. The $d-q$ transformation itself is time-variant, this yields to the following

$$\begin{aligned} \frac{d}{dt}\underline{\psi}_{\alpha\beta}(t) &= \frac{d}{dt}\left([\mathrm{T}]^{\top}_{dq}\,\underline{\psi}^{s}_{dq}(t)\right) \\ &= [\mathrm{T}]^{\top}_{dq}\,\frac{d}{dt}\underline{\psi}^{s}_{dq}(t) + \underline{\psi}^{s}_{dq}(t)\frac{d}{dt}\,[\mathrm{T}]^{-1}_{dq} \end{aligned} \tag{3.63}$$

The derivation of the transformation $[\mathrm{T}]^{\top}_{dq}$ is

$$\begin{aligned} \frac{d}{dt}\,[\mathrm{T}]^{-1}_{dq} &= [\mathrm{T}]^{\top}_{dq}\begin{bmatrix} 0 & -1 \\ 1 & 0 \end{bmatrix}\frac{d}{dt}\vartheta_e \\ &= [\mathrm{T}]^{\top}_{dq}\,\mathbf{J}\omega_e \end{aligned} \tag{3.64}$$

Combining (3.63) and (3.64), the full relationship for the derivative becomes

$$\frac{d}{dt}\underline{\psi}_{\alpha\beta}(t) = [\mathrm{T}]_{dq}^{\top}\left(\omega_e \mathbf{J}\underline{\psi}^s_{dq} + \frac{d}{dt}\underline{\psi}^s_{dq}(\vartheta_e)\right) \tag{3.65}$$

And reciprocally for the forward derivative yields

$$\frac{d}{dt}\underline{\psi}_{dq}(t) = [\mathrm{T}]_{dq}\left(\omega_e \mathbf{J}\underline{\psi}^s_{\alpha\beta} - \frac{d}{dt}\underline{\psi}^s_{\alpha\beta}(\vartheta_e)\right) \tag{3.66}$$

□

Therefore the term on the right in (3.61) represents the time derivative of the rotor flux in the $\alpha-\beta$ coordinates system such that 3.61 can be written as

$$P_{me}(t) = \frac{3}{2}\,\underline{i}^{\top}_{\alpha\beta}(t)\frac{d}{dt}\underline{\psi}_{\alpha\beta}(t) \tag{3.67}$$

where $\underline{\psi}_{\alpha\beta}(t) = \begin{bmatrix}\psi_\alpha(t) & \psi_\beta(t)\end{bmatrix}^{\top}$ is the rotor permanent magnet flux contribution transformed in the $\alpha-\beta$ reference frame.
Finally, in accordance with (1.19) and the magnet flux defined in $d-q$ as per (1.31), the time-derivative of the flux in $\alpha-\beta$ is associated to the BEMF of the machine, therefore it holds

$$P_{me}(t) = \frac{3}{2}\,\underline{i}^{\top}_{\alpha\beta}(t)\underline{e}_{\alpha\beta}(t) \tag{3.68}$$

where $\underline{e}_{\alpha\beta}(t) = \begin{bmatrix}e_\alpha(t) & e_\beta(t)\end{bmatrix}^{\top}$ is the induced voltage produced by the rotational movement of the rotor permanent magnets.
Equation (3.68) tells that, under the simplification claimed with (3.58) the power involved in the production of the electromagnetic torque of an SPMSM driven on the q-axis can be computed by the measured current and the observed BEMF in the transformed two coordinate system. Further, since the equation computes the instantaneous electromagnetic power, it does not depend from the nature of the signals, therefore it holds true either for sinusoidal and non-sinusoidal quantities. The superscript s has been dropped since for definition the $\alpha-\beta$ system refers to stator quantities.
As it has been already shown during the no load experimentation of the LQ-Observer, the induced voltage is ideally expected to be a sinusoid, over the electrical period, but this is never the case in reality and (3.68) helps us to investigate on the residual harmonic quantities, when the BEMF is apart from a sinusoid and further consideration can be obtained on the required current shape for compensating the non-idealities. Let first consider as a reference an ideal SPMSM, as it was defined by proposition. 1.2.1, driven only by the q-axis current, with purely sinusoidal BEMF.
In the two coordinates stator reference frame it holds that the amplitudes of the $\alpha-\beta$ quantities are equal, therefore we address hereafter the peak of the fundamental value of the BEMF and the current, respectively as $\hat{e}$ and $\hat{i}$, such that

$$\hat{e}_\alpha \equiv \hat{e}_\beta = \hat{e} \qquad\qquad \hat{i}_\alpha \equiv \hat{i}_\beta = \hat{i} \tag{3.69}$$

From (3.68), the normalized instantaneous electromagnetic power is computed as

$$P_{me} = \frac{3}{2}\left[\frac{e_\alpha i_\alpha + e_\beta i_\beta}{\hat{e}\hat{i}}\right] \tag{3.70}$$

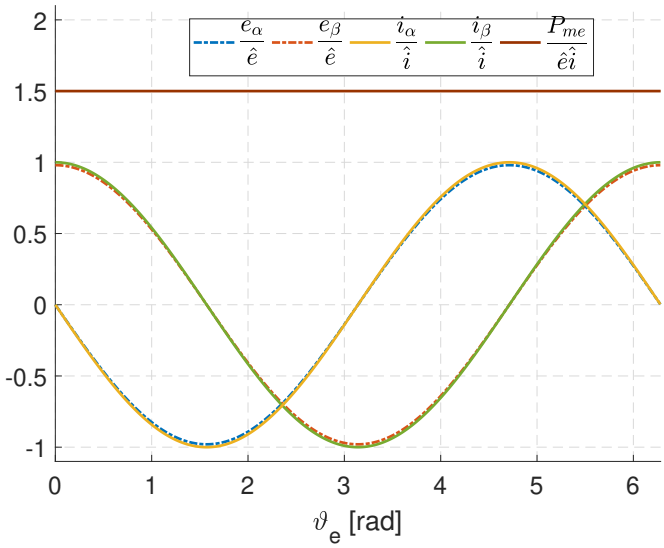

Figure 3.22: Constant electromagnetic power produced by an ideal SPMSM with sinusoidal BEMF- and current waveforms.

where e_α, e_β represent the machine BEMF in $\alpha - \beta$ coordinates. Fig. 3.22 shows the normalized waveforms of BEMF and currents in the $\alpha - \beta$ coordinate system and the resulting power waveform, which is absolutely constant. In this case, the required normalized current waveforms have a purely sinusoidal angle dependency analogous to the BEMF waveforms, namely

$$\frac{i_\alpha}{\hat{i}} = -sin\vartheta_e = \frac{e_\alpha}{\hat{e}} \qquad \frac{i_\beta}{\hat{i}} = cos\vartheta_e = \frac{e_\beta}{\hat{e}} \tag{3.71}$$

At the contrary, when the case of a trapezoidal BEMF is considered in combination with sinusoidal current waveforms, the computed instantaneous electromagnetic power results in a DC-value with a superposed oscillating AC-component, as it has already been extensively explained in Sec. 1.3.2. It appears clear from Fig. 3.23, where again the normalized BEMF and currents are plotted in the $\alpha - \beta$ reference frame. The harmonic content of the power displayed in Fig. 3.23 is directly proportional to the one within the torque, therefore aiming to a smooth electromagnetic power waveform by shaping opportunely the currents leads to an elimination of these unwanted AC-components in the machine torque. In the ideal case with the sinusoidal BEMF, from (3.70) can be deduced the following fact:

$$P_{me} \propto sin(\vartheta_e)^2 + cos(\vartheta_e)^2 \tag{3.72}$$

Since the induced voltage and the current are aligned for producing the maximum torque per ampere and they evolve sinusoidally over position, the latter proportion (3.72) holds true. As a consequence, in case of the trapezoidal BEMF, the $\alpha - \beta$ current magnitudes can be shaped opportunely to force a smooth power function, introducing

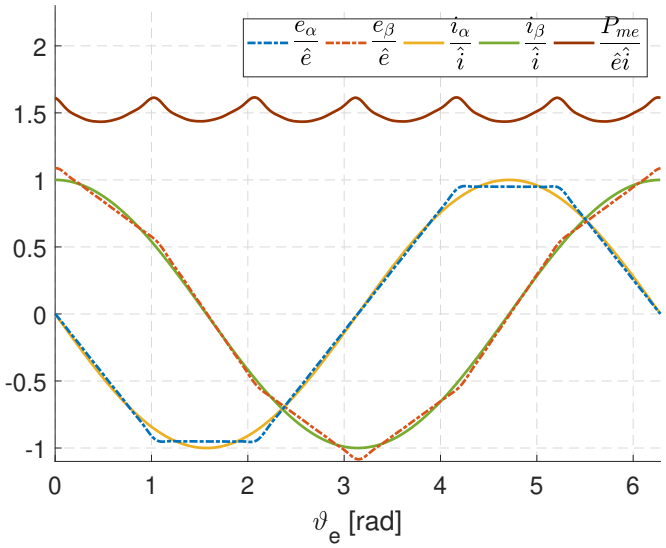

Figure 3.23: Pulsating electromagnetic power caused by trapezoidal BEMF- in combination with sinusoidal current waveforms.

a not sinusoidal position dependency according to:

$$\frac{i_\alpha}{\hat{i}} = \hat{e}\frac{sin(\vartheta_e)^2}{e_\alpha} = f^i_{\alpha,q}(\vartheta_e) \tag{3.73a}$$

$$\frac{i_\beta}{\hat{i}} = \hat{e}\frac{cos(\vartheta_e)^2}{e_\beta} = f^i_{\beta,q}(\vartheta_e) \tag{3.73b}$$

$f^i_{\alpha,q}$ and $f^i_{\beta,q}$ identify the normalized q-current waveforms in the $\alpha-\beta$ reference frame, which are the synchronous torque producer in this case. In Fig. 3.24 the resulting currents and power are shown. The pulsating power is clearly mitigated; a remaining imperfection is due to the fact that from (3.73) the current harmonics above the 13^{th} order were filtered out for reasons of practical implementations. Thus a perfect analytical compensation cannot be reached. Once the currents are computed according to (3.73), in a second step it is necessary to derive the d-axis voltage waveforms required to impress that specific q-axis current waveform to the machine. This can be done exploiting the fundamental voltage equations of the ideal synchronous permanent magnet machine (Sec. 1.2.3). For simplicity we decide to neglect the resistance voltage drop term Ri and consider only the cross-coupling of the flux between the rotating $d-q$ axis. Physically, the voltage on the d-axis has to be controlled in order to keep the q-axis component of the flux linkage constant considering the rotation of the d-q reference frame relative to the $\alpha-\beta$ reference frame with the angular velocity ω_e. In the stator reference frame this objective leads to the subsequent equations:

$$u_{\alpha,d}(t) = \frac{d}{dt}\lambda_{\alpha,q}(t) = L_{sq}\frac{d}{dt}i_{\alpha,q}(t) \tag{3.74a}$$

$$u_{\beta,d}(t) = \frac{d}{dt}\lambda_{\beta,q}(t) = L_{sq}\frac{d}{dt}i_{\beta,q}(t) \tag{3.74b}$$

Considering the fundamental $d-q$ voltage equation 1.26 in steady-state, together with the associated $d-q$ flux 1.30, which define the d-axis voltage as $u_d = -\omega_e L_{sq} i_q$,

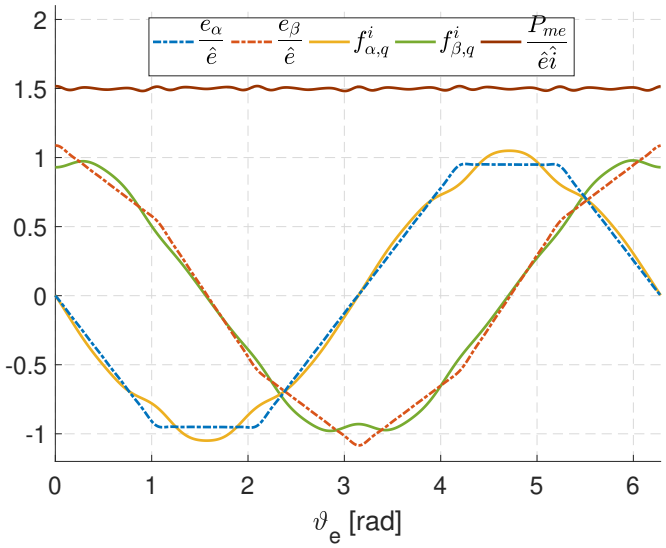

Figure 3.24: The normalized trapezoidal BEMF waveforms and the corresponding current waveforms, appropriate to generate almost constant electromechanical power P_{me} and torque in an SPMSM.

and using the equations (3.73), which define the q-axis current waveforms, the equations (3.74), can be written in the form:

$$u_{\alpha,d}(t) = u_d \left(-\frac{d}{d\vartheta} f^i_{\alpha,q}(\vartheta_e) \right) \tag{3.75a}$$

$$u_{\beta,d}(t) = u_d \left(-\frac{d}{d\vartheta} f^i_{\beta,q}(\vartheta_e) \right) \tag{3.75b}$$

Now, analogous to (3.73) the normalized d-voltage waveforms and in the $\alpha-\beta$ reference frame are defined as:

$$\frac{u_{\alpha,d}(\vartheta_e)}{u_d} = -\frac{d}{d\vartheta} f^i_{\alpha,q}(\vartheta_e) = f^u_{\alpha,d}(\vartheta_e) \tag{3.76a}$$

$$\frac{u_{\beta,d}(\vartheta_e)}{u_d} = -\frac{d}{d\vartheta} f^i_{\beta,q}(\vartheta_e) = f^u_{\beta,d}(\vartheta_e) \tag{3.76b}$$

$$\tag{3.76c}$$

In an ideal SPMSM, with sinusoidal BEMF this simply describes the classical $\alpha\beta/dq$ Park-transformation shown in (1.9), where $u_d = -\omega_e L_{sq} i_q$ is the required d-axis voltage component in the rotor reference frame and $-\frac{d}{d\vartheta} f^i_{\alpha,q}(\vartheta_e)$ and $-\frac{d}{d\vartheta} f^i_{\beta,q}(\vartheta_e)$ are nothing else that the transformation terms $cos(\vartheta_e)$ and $sin(\vartheta_e)$ associated to it. The resulting normalized d-axis voltage waveforms in the case of a trapezoidal BEMF are shown in Fig. 3.25. It is interesting to notice that the price to pay for driving the machine with a reduced torque ripple is an increased harmonic content of the stator voltages, which could potentially increase the stress on the DC side of the drive and the iron-losses in the machine. Careful considerations on the voltage limitation of the power electronics should be carried out and will be done in Sec. 3.4.5.

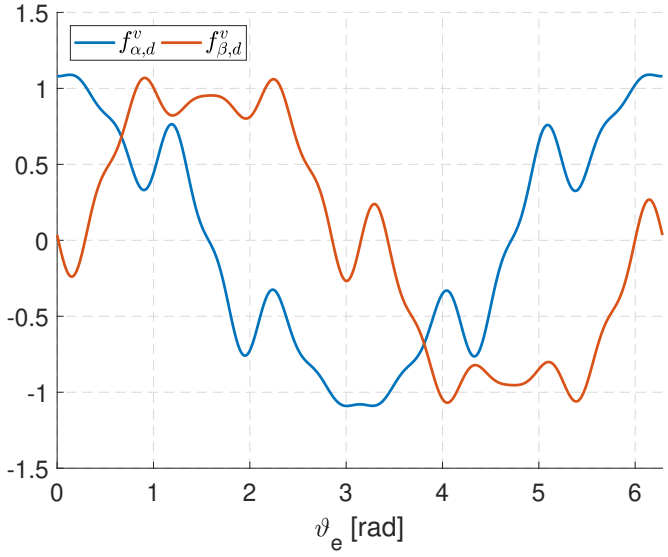

Figure 3.25: Required normalized d-axis voltage waveforms to impress q-axis current waveforms according to $f^i_{\alpha,q}$ and $f^i_{\beta,q}$.

3.4.2. D-axis current and flux weakening

As far we derived the conditions to guarantee the compensation of BEMF harmonics for producing smooth electromagnetic power and torque, in an exemplary case of a trapezoidal shape. However, the treatment of the d-axis current also has to be considered, in case the same machine is operating in the flux weakening range. In the latter condition, a negative d-axis current is injected. This happens either at higher speed in order to counteract the effect of the rotor flux and reduce the amplitudes of the q-axis voltages compared to the BEMF, thus keeping the machine operating within the power electronic's voltage limitation. Or the objective is to generate an additional reluctance component of the torque also at low speed in IPMSMs. Qualitatively, in this situation, it should be able to guarantee that the d-axis flux contribution of the stator excitation, does not modify the harmonic content of the complete d-axis flux. Through the knowledge of the BEMF waveform and considering that the d-axis current directly interacts with the permanent magnet flux, this behavior can be mathematically described by the subsequent rotor/stator reference frame equation:

$$\lambda^d_\alpha(\vartheta_e) = \frac{1}{\omega_e}\int e_\alpha d\vartheta + L_{sd} i_d \cdot f^i_{\alpha,d}(\vartheta_e) \tag{3.77a}$$

$$\lambda^d_\beta(\vartheta_e) = \frac{1}{\omega_e}\int e_\beta d\vartheta + L_{sd} i_d \cdot f^i_{\beta,d}(\vartheta_e) \tag{3.77b}$$

It appears clear that from (3.77)), if we have a non sinusoidal BEMF with a corresponding not purely sinusoidal rotor flux, the normalized d-axis current waveforms $f^i_{\alpha,d}(\vartheta_e)$ and $f^i_{\beta,d}(\vartheta_e)$ have to match the rotor flux waveforms in order not to change the shape of the total flux.

Therefore, according with (3.77) it follows

$$f^i_{\alpha,d}(\vartheta_e) = \frac{1}{\hat{e}} \int e_\alpha d\vartheta \tag{3.78a}$$

$$f^i_{\beta,d}(\vartheta_e) = \frac{1}{\hat{e}} \int e_\beta d\vartheta \tag{3.78b}$$

In Fig. 3.26 the normalized d-axis currents for a trapezoidal BEMF are shown. Due to the integration effect their harmonic content is reduced compared to the BEMF-waveforms and they tend to be almost sinusoidal.

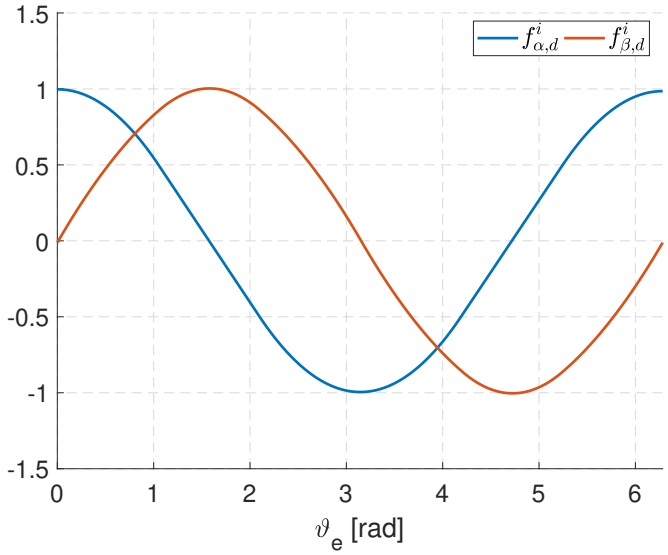

Figure 3.26: Required current shape in order to, for the d-axis current, do not modify the harmonic content of the rotor flux.

The normalized q-axis voltage waveforms necessary to impress these d-axis current waveforms to the machine can now be deduced following a reasoning analogous to the one explained in the equations (3.74) to (3.76) for the d-axis voltage waveforms. However, it is evident that if the normalized d-axis current waveforms are equal to the normalized rotor flux waveforms, the corresponding normalized q-axis voltage waveforms have to be equal to the normalized BEMF-waveforms. Consequently it is obvious that the normalized q-axis voltage waveforms have to be defined as

$$f^u_{\alpha,q}(\vartheta_e) = \frac{e_\alpha(\vartheta_e)}{\hat{e}} \tag{3.79a}$$

$$f^u_{\beta,q}(\vartheta_e) = \frac{e_\beta(\vartheta_e)}{\hat{e}} \tag{3.79b}$$

In Fig. 3.27 these normalized q-axis voltage waveforms for SPMSMs with trapezoidal BEMF are shown.

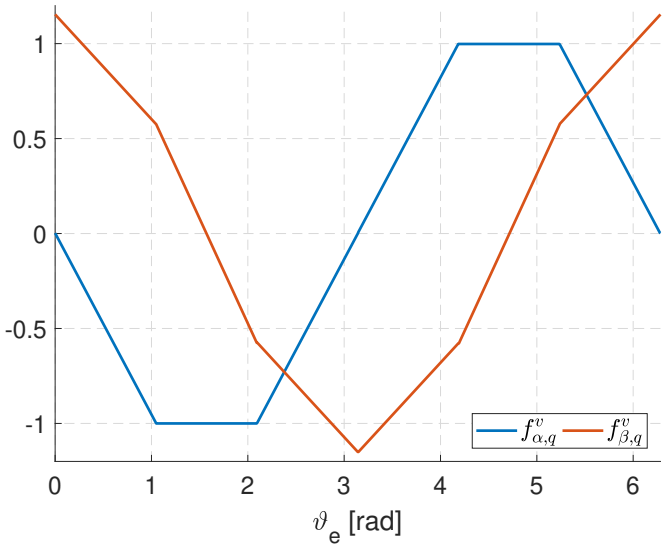

Figure 3.27: Normalized waveforms of the q-axis voltages in the $\alpha - \beta$ reference frame.

3.4.3. Overall control strategy

In the previous section a detailed analysis of the current and voltage waveforms required to avoid or at least to strongly reduce torque oscillations in SPMSMs with non-sinusoidal BEMF has been carried out and the algorithms for calculating these waveforms were introduced. If the target is the compensation of the BEMF harmonics for having a reduced torque ripple, it is necessary to apply a voltage from the controller, which is a linear combination of the solutions found respectively in (3.76) and (3.79). The latter comes in a natural way if the calculated voltage functions, respectively $f^u_{\alpha,d}(\vartheta_e)$, $f^u_{\beta,d}(\vartheta_e)$, $f^u_{\alpha,q}(\vartheta_e)$, $f^u_{\beta,q}(\vartheta_e)$, are embedded within the $dq/\alpha\beta$ backward transformation (1.9), replacing the usual $sin((\vartheta_e))$ and $cos((\vartheta_e))$ functions of the classical Inverse Park transformation. This means that, instead of using the classical Inverse Park transformation (1.9), the new one will take the form of

$$\underline{i}_{\alpha\beta} = [\mathrm{T}]^{-1}_{u,syn} \cdot \underline{i}_{dq} \tag{3.80}$$

with

$$[\mathrm{T}]^{-1}_{u,syn} = \begin{bmatrix} f^u_{\alpha,d} & f^u_{\alpha,q} \\ f^u_{\beta,d} & f^u_{\beta,q} \end{bmatrix}$$

where the super- or subscript u associates the transformation of the voltage-vector and the subscript syn indicates that the derived transformation is suitable for a pure synchronous engine like an SPMSM respectively for the synchronous component of the total torque of an IPMSM. Furthermore, as the current waveforms that have to be impressed to the machine in case of constant field-oriented i_d and i_q values are well-known, the Forward Park transformation can be adapted in a way, that no longer sinusoidal but the requested current waveforms lead to constant current values in the $d-q$ reference frame. These are then provided as controlled quantities within the main field oriented controller. Analogous to (3.80), a backward current transformation from the $d-q$ to the $\alpha - \beta$ reference frame would obey:

$$\underline{i}_{\alpha\beta} = [\mathrm{T}]^{-1}_{i,syn} \cdot \underline{i}_{dq} \tag{3.81}$$

with

$$[\mathrm{T}]^{-1}_{i,syn} = \begin{bmatrix} f^i_{\alpha,d} & f^i_{\alpha,q} \\ f^i_{\beta,d} & f^i_{\beta,q} \end{bmatrix}$$

The latter transformation can then be inverted, leading to

$$\underline{i}_{dq} = [\mathrm{T}]_{i,syn} \cdot \underline{i}_{\alpha\beta} \tag{3.82}$$

with

$$[\mathrm{T}]_{i,syn} = \frac{1}{N} \begin{bmatrix} f^i_{\beta,q} & -f^i_{\alpha,q} \\ -f^i_{\beta,d} & f^i_{\alpha,d} \end{bmatrix}$$

and

$$N = f^i_{\alpha,d} \cdot f^i_{\beta,q} - f^i_{\alpha,q} \cdot f^i_{\beta,d}$$

where the super- or subscript i associates the transformation to the current.
With transformations (3.80) and (3.82), it is now possible to portrait the overall control strategy as it is visualized in Fig. 3.28. Here we see clearly one of the remarkable benefits of the proposed method: The required non-sinusoidal current- and voltage waveforms are generated by simple changes of the transformation-matrices without any impact to the field-oriented controller itself, which both in steady and in transient state behaves completely as before. Particularly it is not at all necessary to adapt the controller in order to deal with velocity-dependent high-frequency AC-components in the set- and real values of the field oriented currents, as it is the case in many other approaches to this problem. As we have now completely discussed the proposed method for SPMSMs, which only exhibit a synchronous torque component, in the next section will be analyzed how the transformations need to be modified in case of IPMSMs, which additionally exhibit a reluctance torque component.

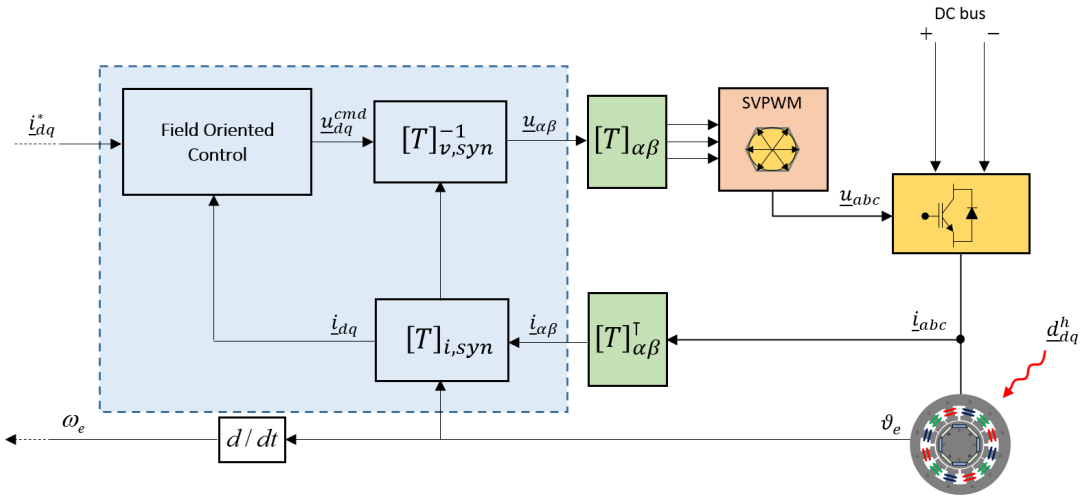

Figure 3.28: Proposed control strategy with the new transformation blocks.

3.4.4. IPMSM and the reluctance torque component

In an IPMSM the buried magnets cause a not-uniform effective air-gap along the circumference of the rotor. The reason for this that both the permanent magnets themselves as well as the corresponding recesses in the rotor sheets exhibit a permeability of μ_0, which is negligibly small compared to the permeability of the surrounding ferromagnetic iron sheets. In the rotor reference frame this is expressed by an anisotropy of the inductance matrix, which in an IPMSM is given by $\mathrm{L}_s = \begin{bmatrix} L_{sd} & 0 \\ 0 & L_{sq} \end{bmatrix}$ with $L_{sq} > L_{sd}$ (see 1.28), whereas in an SPMSM it is isotrope, namely $\mathrm{L}_s = L \cdot \begin{bmatrix} 1 & 0 \\ 0 & 1 \end{bmatrix}$. In consequence and according to equation (1.47) a reluctance torque component

$$m_R = \frac{3}{2} z_p (L_{sd} - L_{sq}) i_{d,rel} i_{q,rel} \tag{3.83}$$

arises as soon as the stator current vector comprises both a length and a quadrature component unequal to zero. The necessity of the additional subscript rel in this equation is explained subsequently: The reluctance torque component is not caused by the interaction of the stator currents with the permanent magnets'flux but by the sharing of the stator current vector and the part of the flux linkage vector excited by the stator currents. Hence, m_R is not linked to the non-sinusoidal rotor flux distribution and BEMF. In consequence, the field oriented current components $i_{d,rel}$ and $i_{q,rel}$, responsible for m_R, are gained from the stator current vector $\alpha - \beta$ not by using the modified transformation matrix $[\mathrm{T}]_{i,syn}$, which is optimized for gaining a smooth synchronous torque component, but by using the standard Park-Transformation matrix $[\mathrm{T}]_{foc}$. Using the control system for SPMSMs according to Fig. 3.28 the field oriented current vector $\underline{i}_{dq,rel}$, which generates the reluctant torque component, can be gained from the current vector $\underline{i}_{dq}$, used by the control system according to:

$$\underline{i}_{dq,rel} = [\mathrm{T}]_{foc} \cdot \underline{i}_{\alpha\beta} = [\mathrm{T}]_{foc} \cdot [\mathrm{T}]^{-1}_{i,syn} \cdot \underline{i}_{dq} \tag{3.84}$$

The result of (3.83) and (3.84) at an arbitrary angle of $\frac{\pi}{6}$ rad between the q-axis and the current space vector is shown in Fig. 9. The reluctance torque component m_r is normalized to its DC component M_R. Clearly, using the current transformation matrices optimized for the synchronous torque component according to equations (3.80) to (3.82), the reluctance torque component will exhibit significant oscillations as expected. In order to achieve a smooth reluctance torque component it would be necessary to use the standard Park-transformation matrices according to (1.9). However, even in an IPMSM it makes sense to maintain it, so that the d-axis currents have the same waveforms as the rotor flux and consequently the normalized q-voltages waveforms are always equal to the one of the BEMF. On one hand this avoids a detuning of the $d-q$ voltage waveforms dependent on the machines operating point and on the other hand we saw that the d-current waveforms are almost sinusoidal even for a trapezoidal BEMF, so that the negative effect of these non-sinusoidal d-currents on the reluctance torque component's oscillations is almost negligible. Hence, in order to obtain an almost smooth reluctance torque component we would have to use the

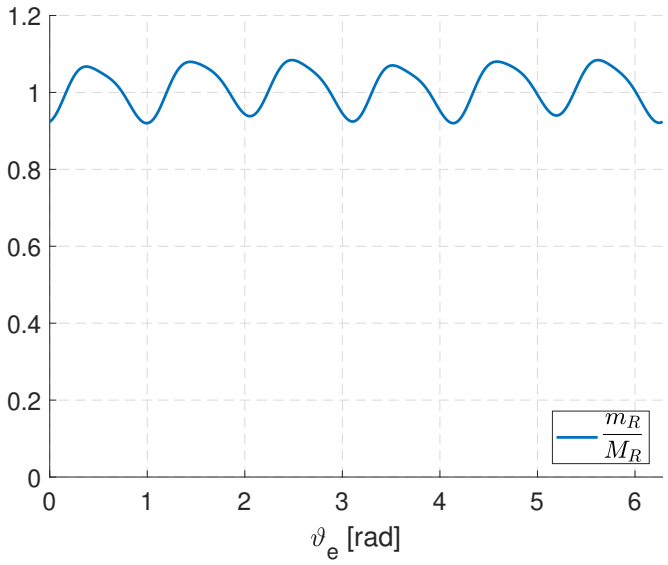

Figure 3.29: Reluctance torque component waveform applying the transformation developed for the SPMSM.

transformation matrices

$$[\mathrm{T}]_{i,rel} = \frac{1}{N}\begin{bmatrix} cos\vartheta_e & sin\vartheta_e \\ -f^i_{\beta,d} & f^i_{\alpha,d} \end{bmatrix} \tag{3.85}$$

with

$$N = f^i_{\alpha,d} \cdot cos\vartheta_e + f^i_{\beta,d} \cdot sin\vartheta_e$$

and accordingly

$$[\mathrm{T}]^{-1}_{v,rel} = \begin{bmatrix} cos\vartheta_e & f^v_{\alpha,q} \\ sin\vartheta_e & f^v_{\beta,q} \end{bmatrix} \tag{3.86}$$

Instead of $[\mathrm{T}]_{i,syn}$ and $[\mathrm{T}]^{-1}_{v,syn}$.
If we do so, the field oriented current vector $i_{dq,r}$ which generates the reluctant torque component is no longer obeying equation (3.84), but

$$\underline{i}_{dq,rel} = [\mathrm{T}]_{foc} \cdot i_{\alpha\beta} = [\mathrm{T}]_{foc} \cdot [\mathrm{T}]^{-1}_{i,rel} \cdot \underline{i}_{dq} \tag{3.87}$$

Applying (3.87) to equation (3.83) we achieve a reluctant torque component as it is displayed in Fig. 3.30. It is clearly visible that now the reluctant torque oscillations shown in Fig. 3.30 have almost disappeared. On the other hand, unilaterally optimizing the torque oscillation on the reluctant torque component only, would immediately leads to oscillations of the synchronous torque component almost equal to the one illustrated in Fig. 3.23. Mathematically this can be described by the fact that now the field oriented current vector $\underline{i}_{dq,syn}$ which is responsible for the synchronous torque can be gained from the constant vector $\underline{i}_{dq}$ according to:

$$\underline{i}_{dq,syn} = [\mathrm{T}]_{i,syn} \cdot \underline{i}_{\alpha\beta} = [\mathrm{T}]_{i,syn} \cdot [\mathrm{T}]^{-1}_{i,rel} \cdot \underline{i}_{dq} \tag{3.88}$$

As far we derived the optimized voltage and current transformation matrices for the synchronous (m_S) and the reluctance (m_R) torque components separately. However in

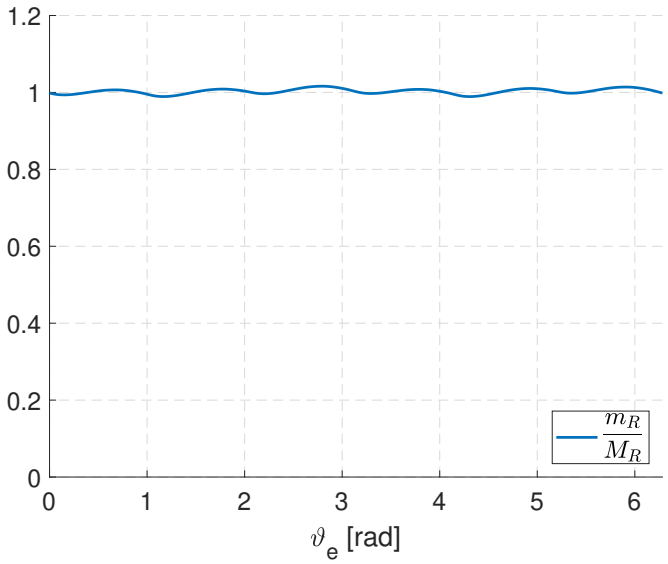

Figure 3.30: Reluctance torque component behavior applying the transformation matrices (3.85) and (3.86).

the IPMSM the two components are superposed to a complete torque $m = m_S + m_R$ and our objective is not to eliminate the torque oscillations of only one component not regarding the other, but to effectively reduce the overall torque oscillations. Observing Fig. 3.30 and Fig. 3.23 closer, we see that the torque oscillations of the synchronous torque component with the Park-transformation an the ones of the reluctance torque component with the transformation (3.80) and (3.82) optimized for the synchronous torque are mainly in counter phase to each other and their amplitude is similar compared to the DC-part of each torque component. Consequently we can postulate that the overall torque oscillations in an IPMSM can be effectively diminished if we linearly shift between the transformation matrices optimized for the synchronous torque component ((3.80), (3.82)) and the ones optimized for the reluctance torque component ((3.85), (3.86)) depending on the relative contributions of m_S and m_R to the overall torque m. So now, considering eq. (1.47), we define the relative contribution factors

$$\gamma_S = \frac{M_S}{M} = \frac{\lambda_{pm}}{\lambda_{pm} + (L_{sd} - L_{sq})i_d} \tag{3.89a}$$

$$\gamma_R = \frac{M_R}{M} = \frac{(L_d - L_q)i_d}{\lambda_{pm} + (L_{sd} - L_{sq})i_d} \tag{3.89b}$$

where M indicates the DC-component of the complete electromagnetic torque (1.47). Finally we generate the - now operation point dependent - transformation matrices $[\mathrm{T}]_i$ and $[\mathrm{T}]_u^{-1}$ by applying the linear weighting factors γ_s and γ_r to the transformation matrices optimized for the synchronous and the reluctance torque component according to:

$$[\mathrm{T}]_u^{-1} = \gamma_S \cdot [\mathrm{T}]_{u,syn}^{-1} + \gamma_R \cdot [\mathrm{T}]_{u,rel}^{-1} \tag{3.90a}$$

$$[\mathrm{T}]_i = \gamma_S \cdot [\mathrm{T}]_{i,syn} + \gamma_R \cdot [\mathrm{T}]_{i,rel} \tag{3.90b}$$

Even though in this way we still achieve pulsating synchronous and reluctance torque components, the oscillations of these torque components largely cancel each other out.

Thus, weighting on-line the two pairs of transformation matrices according to (3.90), depending on the present operation point of the machine and using these transformation matrices in a field oriented control system according to Fig. 3.28 allows to minimize effectively oscillations of the total electromagnetic torque m, enabling a smooth drive at the shaft.

3.4.5. Voltage limitation

As a last theoretical issue, in this section the problem of the voltage constraint is accounted. Due to the limitation of the stator phase voltage to the inverter's input voltage U_{DC}, stator star voltage amplitudes are limited to a value U_{max}. The voltage constraint in the $\alpha - \beta$ reference frame can be expressed by

$$u_\alpha^2 + u_\beta^2 \leqslant U_{max} \tag{3.91}$$

In general, considering the SVPWM (Space Vector Pulse-Width Modulation) as a switching technique $U_{max} = 0.57 \cdot U_{dc}$, being U_{dc}.
From Fig. 3.27 and 3.25 it is obvious that the optimization of the current waveforms for the proper torque oscillation reduction leads to an unavoidable increment of the peak-to-peak voltage compared to an operation with sinusoidal current and voltage waveforms. This can be also seen plotting the SPMSM torque compensating solution of the voltage derived according to (3.76) and (3.79).
The $\alpha - \beta$ trajectory are reported in Figure 3.31. The peak value of the voltage vector

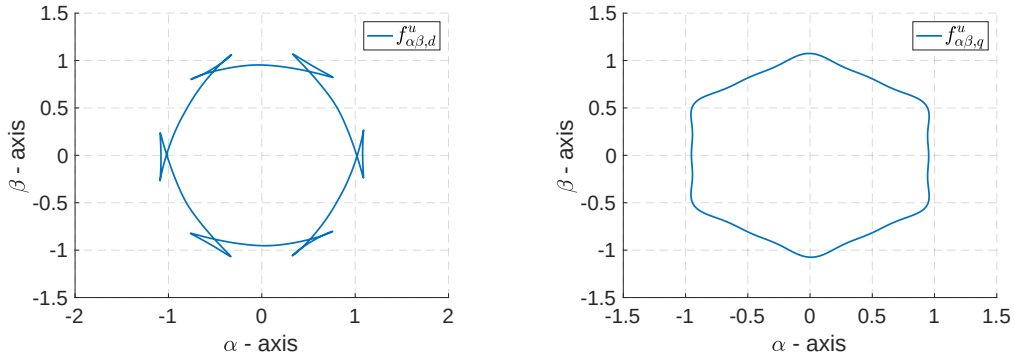

(a) (b)

Figure 3.31: Transformation representation in the $\alpha - \beta$ plane: a) trajectory of the voltage vector for compensating the electromagnetic power oscillations; b) trajectory of the voltage vector required for the direct flux component.

can be computed as

$$\begin{aligned} \max\left(\|f^u_{\alpha\beta,d}\|_2\right) &= 1.134 \\ \max\left(\|f^u_{\alpha\beta,q}\|_2\right) &= 1.078 \end{aligned} \tag{3.92}$$

Therefore impressing the voltage shape from eq. (3.76) and (3.79), the resulting voltage would increase respectively of about $\sim 13.5\%$ and $\sim 7.8\%$, which could easily overshoot the maximum voltage achievable by the hardware when the drive is in a situation of

a relative saturated DC bus (e.g. high speed, low battery level). More in detail the real voltage feed to the inverter is a linear combination of both the voltage solutions, in accordance with the magnitude of the commanded $d-q$ voltages.
As a consequence of the latter fact, an active limitation for the harmonic injection need to be integrated in order to avoid stability problems and damages while machine operation. Since the proposed transformations are designed off-line, it is possible to predict a-priori which will be the maximum value of the resulting voltage once the required - linearly weighted - transformation has been applied, accounting for the actual $d-q$ voltage values. In general the peak of the voltage required by the controller can be computed at any time through

$$\hat{u}(\vartheta_e) = \|\underline{u}_{\alpha\beta}\|_2 = \sqrt{u_\alpha^2 + u_\beta^2} \tag{3.93}$$

In accordance with the transformation developed as far, equation (3.93) can be further expanded in two different ways, assuming two feasible operation of the machine, that is

- the modified transformation for the synchronous torque $[\mathrm{T}]^{-1}_{u,syn}$;
- the modified transformation for the reluctance torque $[\mathrm{T}]^{-1}_{v,rel}$.

Respectively, from (3.93), the two operations can be described as

$$\hat{u}_S(\vartheta_e) = \sqrt{(u_d f^v_{\alpha,d} + u_q f^u_{\alpha,q})^2 + (u_d f^u_{\beta,d} + u_q f^u_{\beta,q})^2} \tag{3.94}$$

$$\hat{u}_R(\vartheta_e) = \sqrt{(u_d cos\vartheta_e + u_q f^u_{\alpha,q})^2 + (u_d sin\vartheta_e + u_q f^u_{\beta,q})^2} \tag{3.95}$$

Where the indexes S and R are respectively associated with the synchronous and reluctance transformation and u_d, u_q are the actual voltages required by the controller. For each of them, considering $u_d = 1$ and $u_q = 1$, it is possible to evaluate four coefficients which predicts the increase of the total voltage applied. The field-oriented operation, with the classical transformations (1.10), is taken as a reference, since the sinusoidal Park transformation leaves unaltered for definition the commanded voltage from the controller. The procedure for calculating the corresponding coefficients of the two modified transformations is described as follow:

1. Evaluate $\hat{u}(\vartheta_e)$ for $[\mathrm{T}]^{-1}_{u,syn}$ and $[\mathrm{T}]^{-1}_{u,rel}$ setting u_d and u_q to 1;
2. Find the $\hat{\vartheta}_e$ which corresponds to the maximum of $\underline{u}_{\alpha\beta}(\vartheta_e)$;
3. Obtain the coefficients of the transformation functions evaluating each one of them in correspondence of $\hat{\vartheta}_e$.

The idea is represented in Fig. 3.32 and Fig. 3.33 respectively for the synchronous (3.80) and reluctance torque transformation (3.86). Once the coefficients have been evaluated from the functions $f^u_{\alpha,d}(\hat{\vartheta}_e)$, $f^u_{\beta,d}(\hat{\vartheta}_e)$, $f^u_{\alpha,q}(\hat{\vartheta}_e)$, $f^u_{\beta,q}(\hat{\vartheta}_e)$, $sin\hat{\vartheta}_e$, $cos\hat{\vartheta}_e$, the equations (3.94), (3.95) can be rewritten as

$$\hat{u}_S(\hat{\vartheta}_e) = \sqrt{(u_d k_1 + u_q k_2)^2 + (u_d k_3 + u_q k_4)^2} \tag{3.96}$$

$$\hat{u}_R(\hat{\vartheta}_e) = \sqrt{(u_d k_1 + u_q k_2)^2 + (u_d k_3 + u_q k_4)^2} \tag{3.97}$$

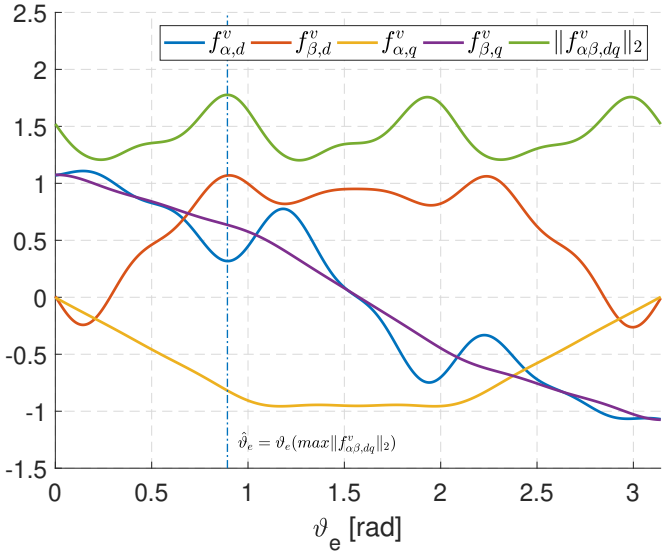

Figure 3.32: Effective oscillation of the resulting voltage vector applying the transformation for the synchronous component $[\mathrm{T}]^{-1}_{u,syn}$.

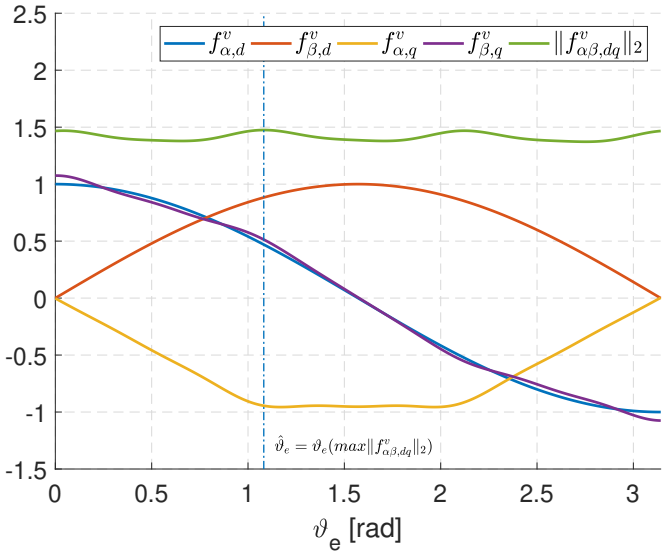

Figure 3.33: Effective oscillation of the resulting voltage vector applying the transformation for the reluctance component $[\mathrm{T}]^{-1}_{u,rel}$.

where the coefficients k_1, k_2, k_3, k_4 for the respective transformations are reported in Tab. 3.2.

Table 3.2: Coefficients for the trapezoidal BEMF

	k_1	k_2	k_3	k_4
$\hat{u}_S$	0.27	1.09	0.82	0.68
$\hat{u}_R$	0.48	0.88	-0.94	0.51

For the sake of completeness, the peak of the voltage for the reference Park transformation (1.10) is defined as

$$\hat{u}_F = \sqrt{u_d^2 + u_q^2} \tag{3.98}$$

Let further consider that an IPMSM is operated through equations (3.90) with a general value of the weights γ_S and γ_R and for instance, the voltage required by the controller $\hat{u}$ exceeds the maximum voltage available at the power electronics. It becomes necessary to adjust the weights in order to reduce the maximum peak voltage and obtain a drive operation which is feasible with the hardware constraint.
The solution of this problem can be formalized with the following optimization

$$\begin{aligned}
\underset{\gamma_F,\gamma_S,\gamma_R}{\text{minimize}} \quad & (\gamma_F^* - \gamma_F)^2 + (\gamma_S^* - \gamma_S)^2 + (\gamma_R^* - \gamma_R)^2 && \text{(3.99a)}\\
\text{subject to} \quad & \gamma_F + \gamma_S + \gamma_R = 1\,, && \text{(3.99b)}\\
& \gamma_F \cdot \hat{u}_F + \gamma_S \cdot \hat{u}_S + \gamma_R \cdot \hat{u}_R = U_{max}\,. && \text{(3.99c)}
\end{aligned}$$

where γ_F expresses a certain weight for the sinusoidal Park transformation. The latter is included, in order to eventually drive the machine without impressing any particular harmonic voltage waveform, but sinusoidal. Solving problem (3.99) translates to maximize the torque harmonic compensation while fulfilling the voltage limitation constraint. This is achieved through a linear combination of the overall three voltage inverse transformation matrices available, respectively $[\mathrm{T}]_{foc}^{-1}$, $[\mathrm{T}]_{u,syn}^{-1}$, $[\mathrm{T}]_{u,rel}^{-1}$, with their corresponding forward transformation matrices $[\mathrm{T}]_{foc}$, $[\mathrm{T}]_{i,syn}$, $[\mathrm{T}]_{i,rel}$.

Problem (3.99) can be solved via the augmented Lagrangian function, where the two equality constraints, namely (3.99b) and (3.99c) can be integrated in the original cost-function via direct penalization.
Defining the cost function and the equality constraints as

$$\begin{aligned}
J &= (\gamma_F^* - \gamma_F)^2 + (\gamma_S^* - \gamma_S)^2 + (\gamma_R^* - \gamma_R)^2 && \text{(3.100a)}\\
q_1 &= 1 - \gamma_F - \gamma_S - \gamma_R && \text{(3.100b)}\\
q_2 &= U_{lim} - \gamma_F \cdot \hat{v}_F - \gamma_S \cdot \hat{v}_S - \gamma_R \cdot \hat{v}_R && \text{(3.100c)}
\end{aligned}$$

where U_{lim} expresses a generic voltage limit value.
The original constrained problem (3.99) can be transformed in its unconstrained version, that is

$$\underset{\gamma_F,\gamma_S,\gamma_R}{\text{minimize}} \quad J + \lambda_1 \cdot q_1 + \lambda_2 \cdot q_2 \tag{3.101}$$

Further, problem (3.101) can be compactly represented in a matrix form as

$$\begin{bmatrix} 2 & 0 & 0 & -1 & -\hat{u}_F \\ 2 & 0 & 0 & -1 & -\hat{u}_S \\ 2 & 0 & 0 & -1 & -\hat{u}_R \\ 1 & 1 & 1 & 0 & 0 \\ \hat{u}_F & \hat{u}_S & \hat{u}_R & 0 & 0 \end{bmatrix} \cdot \begin{pmatrix} \gamma_F \\ \gamma_S \\ \gamma_R \\ \lambda_1 \\ \lambda_2 \end{pmatrix} = \begin{bmatrix} 2\gamma_F \\ 2\gamma_S \\ 2\gamma_R \\ 1 \\ U_{lim} \end{bmatrix} \tag{3.102}$$

Solution of system (3.102) is found analytically and it is expressed by the following result:

$$\lambda_2 = \frac{U_{lim} - \frac{1}{3}a_1 + \frac{1}{3}\gamma_F^* a_2 + \frac{1}{3}\gamma_S^* a_3 + \frac{1}{3}\gamma_R^* a_4}{\frac{1}{2}\left(\hat{u}_F^2 + \hat{u}_S^2 + \hat{u}_R^2\right) - \frac{1}{6}a_1^2} \tag{3.103a}$$

$$\lambda_1 = \frac{2}{3}\left(1 - \gamma_F^* - \gamma_S^* - \gamma_R^*\right) - \frac{1}{3}\lambda_2 a_1 \tag{3.103b}$$

$$\gamma_F = \gamma_F^* + \frac{1}{2}\lambda_1 + \frac{1}{2}\hat{u}_F\lambda_2 \tag{3.103c}$$

$$\gamma_S = \gamma_S^* + \frac{1}{2}\lambda_1 + \frac{1}{2}\hat{u}_S\lambda_2 \tag{3.103d}$$

$$\gamma_R = \gamma_R^* + \frac{1}{2}\lambda_1 + \frac{1}{2}\hat{u}_R\lambda_2 \tag{3.103e}$$

where

$$\begin{aligned} a_1 &= \hat{u}_F + \hat{u}_S + \hat{u}_R \\ a_2 &= \hat{u}_S + \hat{u}_R - 2\hat{u}_F \\ a_3 &= \hat{u}_F + \hat{u}_R - 2\hat{u}_S \\ a_4 &= \hat{u}_F + \hat{u}_S - 2\hat{u}_R \end{aligned} \tag{3.104}$$

The resulting optimal factors in (3.103) can be efficiently computed in real-time. The computation of the optimal weights for the transformations is embedded within the controller and computed on-line in case the following condition is not matched for the specific operation of the machine:

$$\gamma_F \cdot \hat{u}_F + \gamma_S \cdot \hat{u}_S + \gamma_R \cdot \hat{u}_R \leq U_{lim} \tag{3.105}$$

For a practical implementation, u_d and u_q are passed through a low-pass filter in order to consider only the effective value and get rid of eventual ripple.

3.4.6. Application on an IPMSM

For the validation of the method, it is proposed a steady-state harmonic analysis at a fixed speed of 200 *rpm*. The latter has been selected in order to cope with the limited bandwidth of the torque sensor.
It is worth to remark that the algorithm in principle has no limitation for working at high speed operation. However, further aspects must be considered. From one side, the sampling theorem puts an hard limit to the capabilty of the controller, to inject specific harmonic orders within the machine as the electrical speed increases (see assumption 1.4.3).
Further, in the praxis it would be not convenient to inject harmonics for compensating the torque pulsation at higher speed due to the risk of compromising the efficiency of the machine and moreover, the mechanical inertia of the motor acts as a natural filter for the tangential vibrations at high frequency, which tends to disappear at the shaft.
For the above mentioned reasons, the author believes that this technique finds its natural application in a low speed range, where the benefits are maximized.
In particular two cases are compared, where the torque behavior of the machine is examined:

- $A-$ the motor runs on the q-axis;
- $B-$ the motor runs on the MTPA (Maximum Torque per Ampere) characteristics.

The two tests are shown in the $d-q$ axis plane of the current in Fig. 3.34 and respectively the set-points for the currents are $\underline{i}_{dq} \in A : [0,\ 4]$ and $\underline{i}_{dq} \in B : [-2.1,\ 3.8]$. The

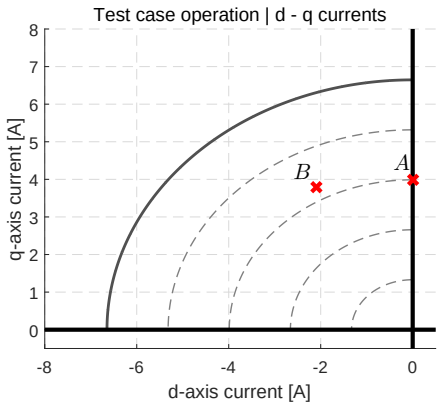

Figure 3.34: Current load points implemented at the test bed.

transformations are obtained processing the BEMF of the motor and they are directly embedded within the controller; the detail of the configuration is presented in Fig. 3.36. It should be here mentioned that for allowing efficient real-time computation, the transformations are stored in the frequency domain, therefore it is only needed the harmonic order and the magnitude for each harmonic, in this case the $5^{th} - 7^{th}$ and the $11^{th} - 13^{th}$. The classical Park transformation performs in less then 2 μs, exploting the efficient evaluation method for the fundamental $sin(\vartheta_e)$ and $cos(\vartheta_e)$, which increases to around 7 μs including the higher harmonic orders for the non-sinusoidal transformation.
The scheme allows to modify the voltage and current profile in real-time very easily by changing the weighting factors. From Fig. 3.36 it is implied that the standard FOC is operated with $\gamma_F = 1,\ \gamma_S = 0$ and $\gamma_R = 0$.

The results for test A and B are shown in Fig. 3.37-3.38 and Fig. 3.39-3.40.
For the measurements on the q-axis the weights for the synchronous and reluctance torque transformations have been set respectively $\gamma_S = 1$ and $\gamma_R = 0$; while for the operation on the MTPA, since a certain reluctance contribution is present, they have been set to $\gamma_S = 0.65$ and $\gamma_R = 0.35$.
Clearly, in both the cases a strong harmonic disturbance is observed on the measured torque.
On the other side, the imposed voltages and currents to the machine via the modified transformations are able to strongly reduce the torque ripple, to a value below the 2%, at the price of a highly distortion of the current and the voltage applied. In both the test A and B when the sinusoidal Park transformation is applied on the left, there is no distinction between the $d-q$ currents seen by the controller and by the electrical machine, that is $i_d = i_d^{em} = i_d^{ctrl}$ and $i_q = i_q^{em} = i_q^{ctrl}$. They are almost constants, leading

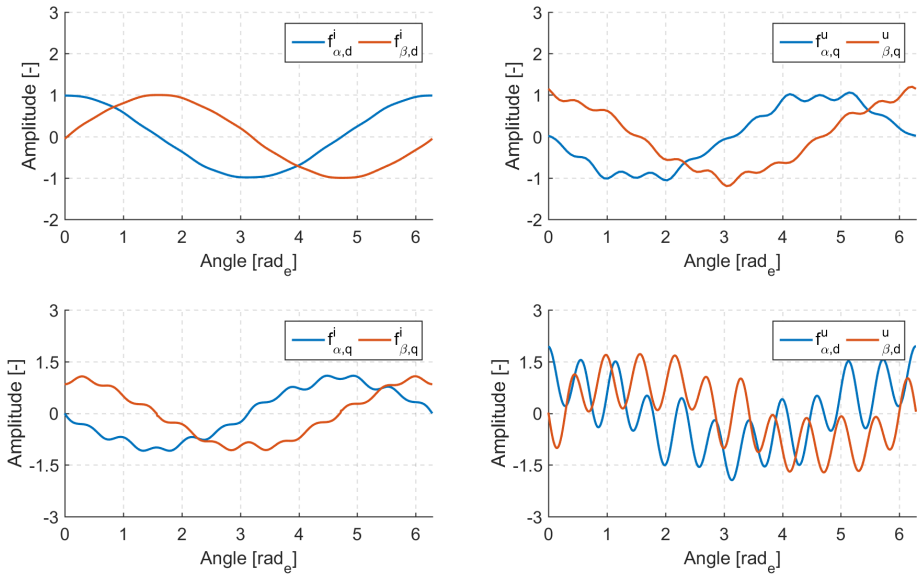

Figure 3.35: Computed functions from the induced voltage of the machine under test.

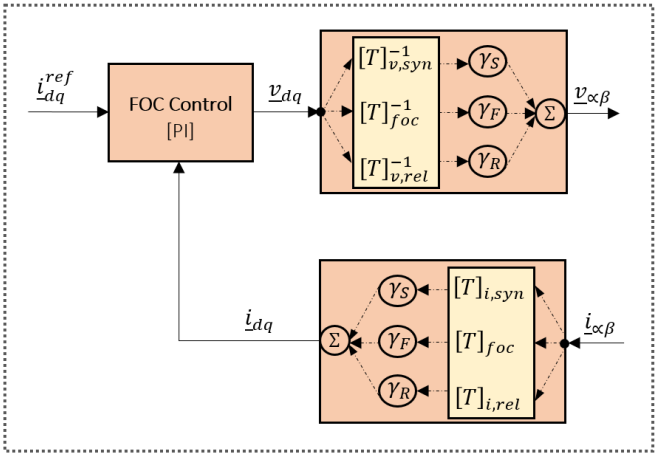

Figure 3.36: Embedded transformations with their weighting factors.

to a non ideal machine electromagnetic power behavior, thus the modified transformation is required.
In the second case, applying the shaped non sinusoidal functions both at the control voltage and at the feedback current level, a strong discrepancy arises between the magnitudes seen by the controller and the PMSM. The latter is due to the fact that, in order to correct the machine non idealities and force it to behave as an ideal PMSM in the $d-q$ reference frame, the transformation is not anymore sinusoidal and brings harmonics within the machine.
This results in the correction of the disturbances, while the control performances remains un-mutated during the harmonic injection. The torque harmonic compensation

comes in general at the expense of the average torque produced, in fact the rotor flux harmonics combines synchronously with the respective orders of the current harmonics and they contribute to the average torque production. In this sense, compensating the harmonic disturbance, the total electromagnetic torque is reduced. In Tab. 3.3 the average torque reduction for the test case A and B is reported, where respectively the first column denote the torque with sinusoidal transformations and the second column with not sinusoidal transformations. Further, in Fig. 3.42-3.43, the voltage and the current in the stator reference frame are reported, respectively for the test A and B and in Tab. 3.4 is reported the current total harmonic distortion (THD). This shows the impressed $\alpha - \beta$ voltage and current waveforms necessary for compensating the pulsating power and torque.

Table 3.3: Average torque reduction

	Sin. Transf.	**Non-Sin. Transf.**	
	$m_{avg}\ [Nm]$	$m_{avg}\ [Nm]$	Reduction [%]
Test A	5.19	5.05	-2.73
Test B	6.52	6.33	-2.91

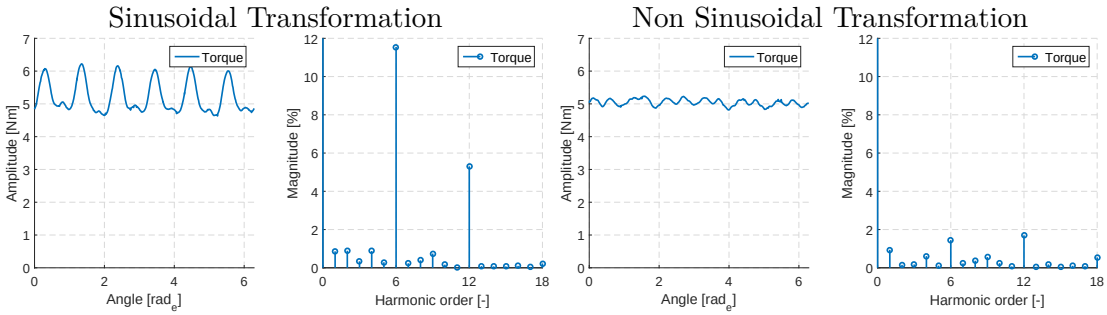

Figure 3.37: Test case A: the measured torque and its harmonic spectrum with the sinusoidal transformation [*left*] and with the proposed non sinusoidal functions [*right*].

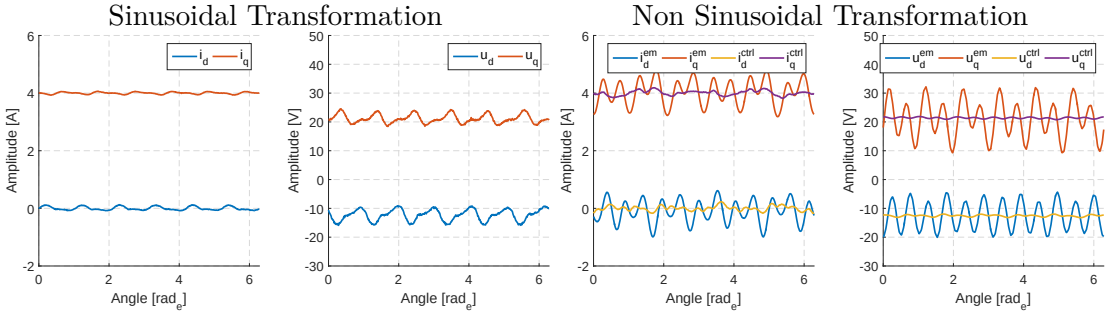

Figure 3.38: Test case A: the measured $d-q$ axis currents and commanded voltages with the sinusoidal transformation [*left*] and with the proposed non sinusoidal functions [*right*]; where *em* stands for electrical machine and *ctrl* stands for the $d-q$ axis main controller.

Finally, in order to validate the capability of our controller to monitor the total

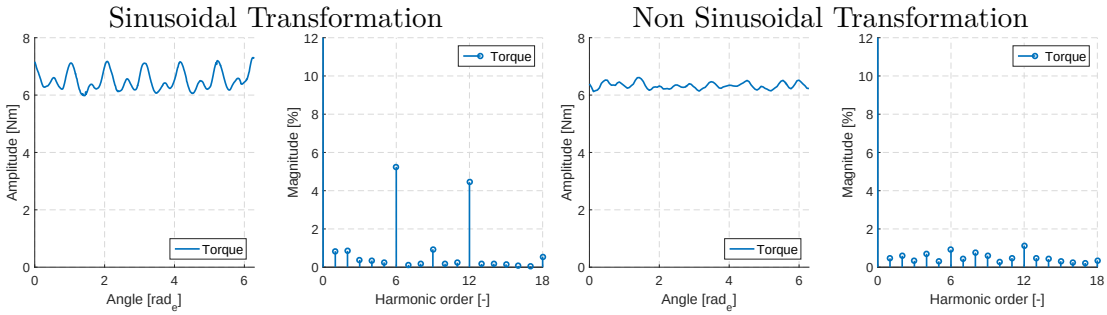

Figure 3.39: Test case B: the measured torque and its harmonic spectrum with the sinusoidal transformation [*left*] and with the proposed non sinusoidal functions [*right*].

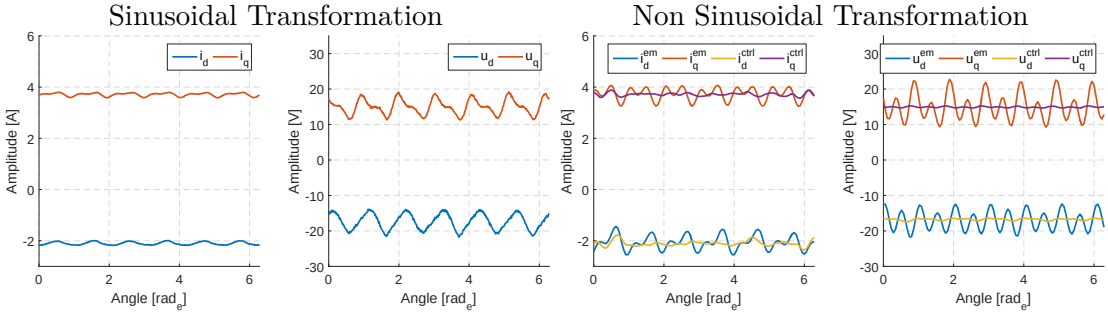

Figure 3.40: Test case B: the measured $d-q$ axis currents and commanded voltages with the sinusoidal transformation [*left*] and with the proposed non sinusoidal functions [*right*], where *em* stands for electrical machine and *ctrl* stands for the $d-q$ axis main controller.

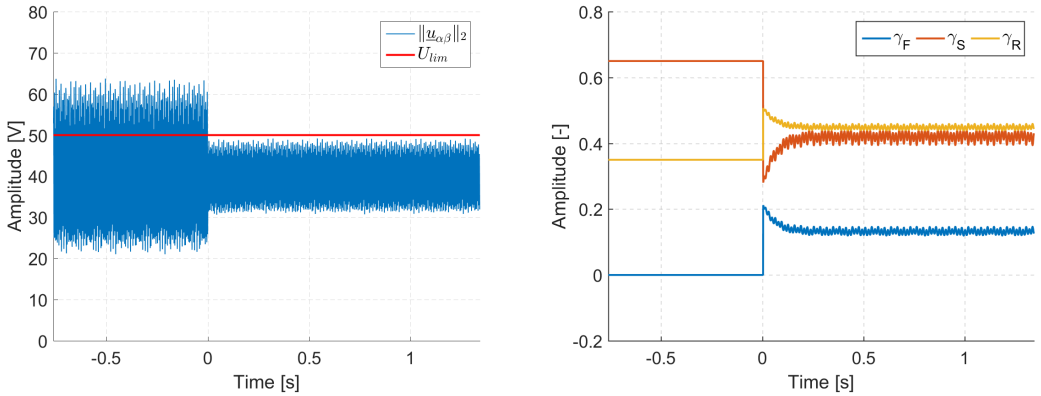

Figure 3.41: Harmonic injection under voltage constraint with a constant speed drive. The voltage limit is enable at $t = 0$.

voltage increment and eventually reduce the harmonic injection in order to fulfill a voltage limitation, two test have been conduced. The voltage limitation has been set at 50 V and the machine is run at the operation of case B. The first test at a fixed

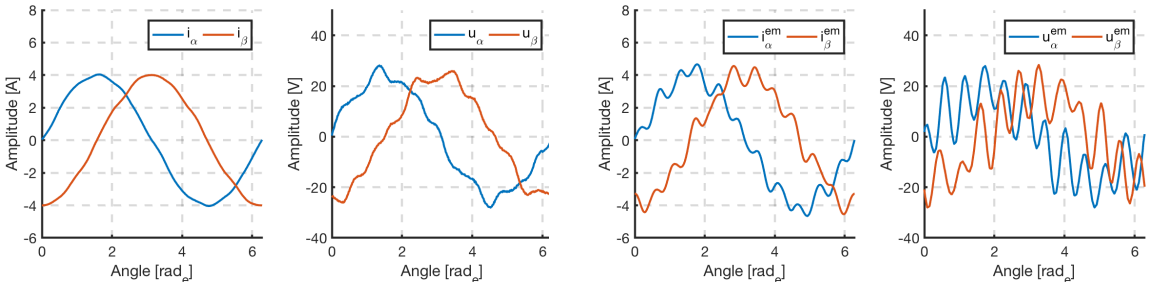

Figure 3.42: Test case A: the measured $\alpha - \beta$ axis currents and commanded voltages with the sinusoidal transformation [*left*] and with the proposed non sinusoidal functions [*right*].

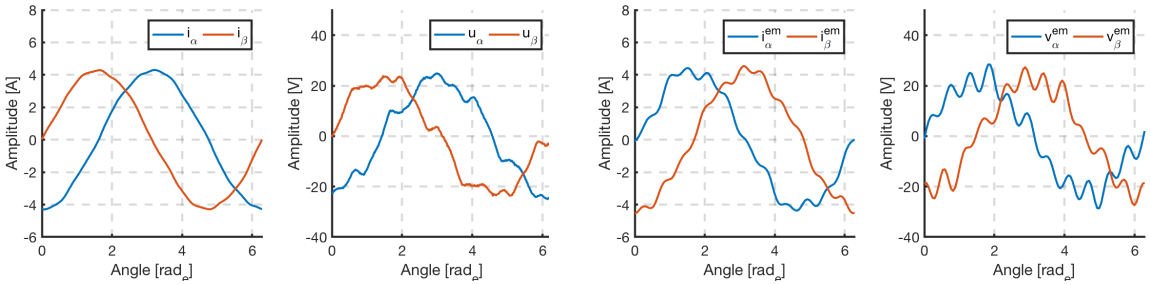

Figure 3.43: Test case B: the measured $\alpha - \beta$ axis currents and commanded voltages with the sinusoidal transformation [*left*] and with the proposed non sinusoidal functions [*right*].

speed of 300 *rpm* is presented in Fig. 3.41, where the injection is performed with $\gamma_F = 0$, $\gamma_S = 0.65$ and $\gamma_R = 0.35$. At $t = 0$ the voltage constraint is enabled and the algorithm adapts the injection in order to drive the motor with a peak voltage below U_{lim}. The resulting weighting factors after the re-calculation respectively are $\gamma_F = 0.12$, $\gamma_S = 0.46$ and $\gamma_R = 0.42$. Clearly, in order to avoid the violation of the boundary, the optimality for the harmonic compensation is lost. A second test has been carried, where in this case the speed has been increased with 3 steps from 300 *rpm* till 360 *rpm*, therefore the voltage required by the inverter slightly increases over time. The experiment is shown in Fig. 3.44. Once again, the algorithm is capable to reduce the voltage injection gradually, while keeping the drive in safe conditions.

Table 3.4: Phase current harmonic content

	Sin. Transf. THD [%]	**Non-Sin. Transf.** THD [%]
Test A	1.51	9.8
Test B	1.53	7.3

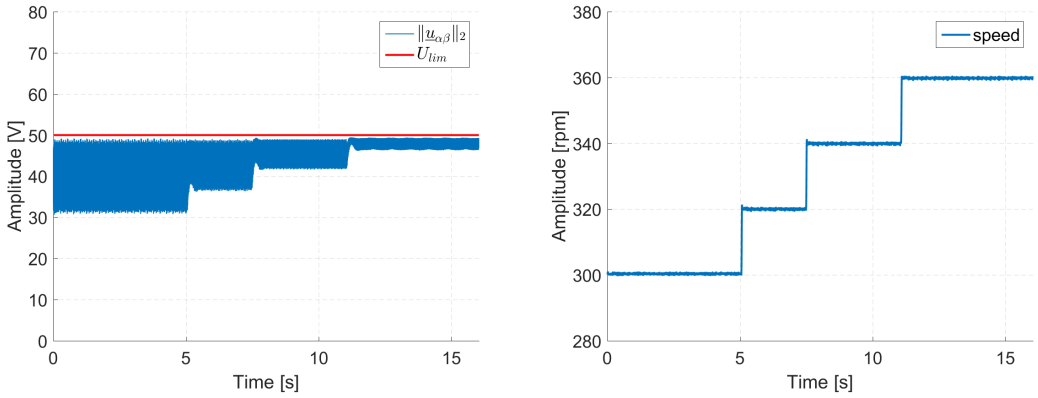

Figure 3.44: Harmonic injection under voltage constraint with stair-increasing speed drive.

3.5. Final Considerations

In this chapter it has been deeply investigated the harmonic behavior of the machine and in particular different approaches have been developed in order to properly control the harmonics. Starting from the principle of active noise cancellation in the acoustic field, the issue has been transferred on the rotational synchronous machines. The problem has been tackled either from an on-line feed-back perspective and from a more general feed-forward technique based on some simplifications.
The first method involves high on-line effort in order to estimate the quantity of interest and to build-up consequently a counteraction for mitigating the disturbance. Although, it is capable to adapt in real-time on varying machine behavior, it suffers from a calibration point of view, since it generates transient effects during activation. However, it has been shown that it is possible to accurately estimate the torque disturbance and robustly suppress it, independently from the operative condition. One of the limitation encountered during the design and validation of the feed-back method is that it requires a pre-knowledge of the magnetic characteristic of the machine and this could be a limitation for certain applications.
The latter, together with other phenomenons observed during experimentations, led to focus on a different approach, which helped to overcome the limitations encountered with the first method. It has been possible to derive current harmonics necessary to produce a smooth electromagnetic torque with the only knowledge of the BEMF shape, and further, through model-base considerations, the required voltage harmonic functions have been computed.

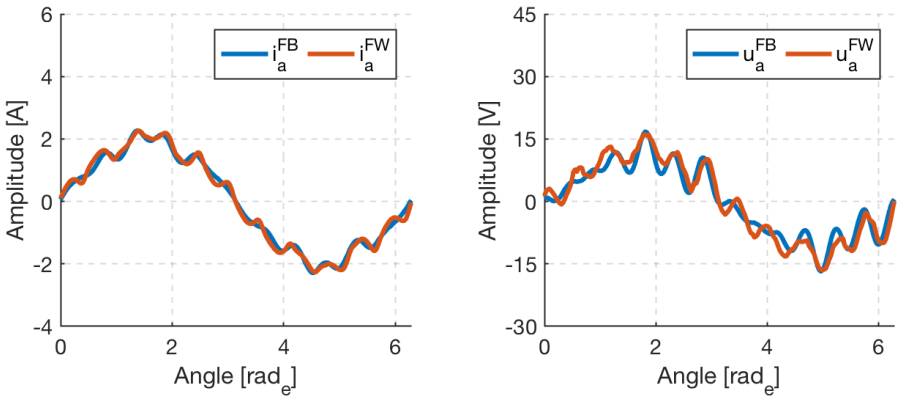

Figure 3.45: Comparison between the feed-back (FB) and the feed-forward injection (FW) methods at respectively $i_d = 0\ A$, $i_q = 2\ A$ and $n = 100\ rpm$.

This led to the benefit of reducing the on-line computational effort and to get rid of eventual stability problems during transient events. Further, the methodology is based on position-dependent normalized functions, therefore its behavior is not influenced by machine parameter uncertainties. At the contrary, it is less flexible in terms of adaptability and therefore could produce lower performances over time, if adaptive routine are not integrated in the controller.

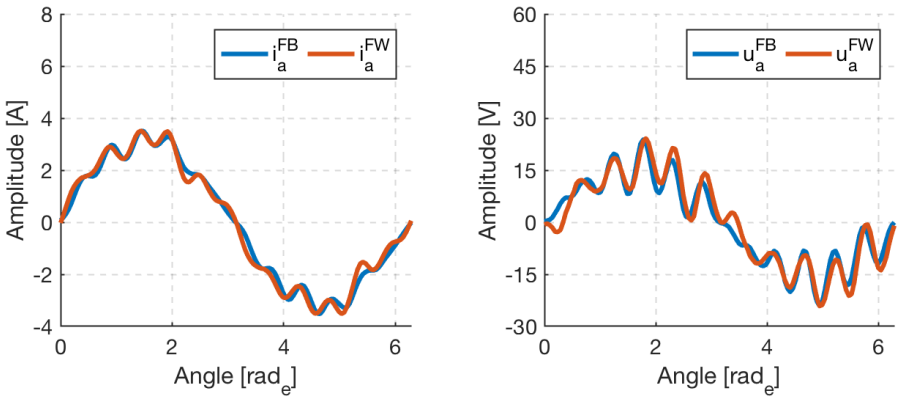

Figure 3.46: Comparison between the feed-back (FB) and the feed-forward (FW) injection methods at respectively $i_d = -1\ A$, $i_q = 3\ A$ and $n = 100\ rpm$.

Never the less, even though both approaches start from different theoretical perspectives, they lead to the same result, that is the desired correction of the electromagnetic torque harmonics. The final solution obtained in terms of current and voltage harmonics injected into the machine, qualitatively corresponds. Finally, this fact is reported in the results of Fig. 3.45 - 3.46 where the phase currents and voltages are compared in steady-state condition after the injection is enabled for both the method developed in Sec. 3. In general, it is possible to note an high correlation between the two methods, however the feed-forward method shows a consistent stronger harmonic quantity in both the operation. This can be explained by the fact that the feed-forward method is designed off-line through the precise processing of the BEMF, while the feed-back method relies on the on-line estimation of the overall voltage harmonic disturbance and the quality of its injection directly depends from the tuning of the LQO, in terms of estimation's regularization. The latter makes more sensitive the controller to the higher estimated frequencies.

Conclusions

The work of this PhD focuses on the investigation of advanced control algorithms for the control of constant and periodic disturbances in PMSM, with the discussion of different methods for improving their negative influence on the machine current and the torque produced at the shaft.

In the first part of this work some fundamentals on the electrical drives consisting of a PMSM and a power module have been given. In particular the electrical machine is first introduced in an ideal system and after it is proposed an extended model which includes the harmonics and position-dependent effects. The discussion of the disturbances from a control perspective has been presented starting from simpler concept to more complex one.

In the second part constant disturbance effects are considered on the dynamical performances of the current control and after the detailed analysis in frequency domain, simple methods for improving the state-of-art decoupling network are given and validated on the test-bench. Thanks to the feature of the introduced estimator, the transient behavior of the proposed strategy results in a consistent fast and precise performance. The control scheme allows to avoid the implementation of anti-windup mechanisms in the current control, making the overall controller less sensitive to parameter mismatch. Further, due to the low computational burden, the algorithm is suitable for low cost hardware.

In the third part, the more complex influence of periodic disturbances has been deeply investigated. The theoretical model proposed in the first part is validated comparing the real measured torque with an estimation based on the recovered disturbance affecting the observed voltages and currents. The results are clearly acceptable and further, the experimental validation stressed out the fact that few terms have a predominant role in producing the harmonic disturbances, compared to the other. These considerations let us develop two strategies for suppressing the different harmonic orders visible within the torque at low speed operation. One strategy relies on on-line adaptive policies, where the estimated informations are passed through a series of optimization algorithms with different objectives. The other strategy, based on some simplification, generates off-line some pre-determined functions, limiting the on-line burden to the computation of LUTs. Both methods brought satisfactory results during the experi-

mental validation, confirming the validity of our approximation made on the original complex model. Although the hardware devices limited the opportunity to validate the methodologies at low speed, this represents a realistic scenario, in fact at higher speed the artificial injection of harmonics within the machine current brings more negative effects, in terms of losses and audible noise, than benefits on the shaft stress, in fact the machine inertia acts as a natural filter for the high frequencies harmonics.

Finally, as a future and natural extension, it could be investigated the possibility to shape the currents and the voltages for influencing the radiated noise and vibrations. In fact, the scope of the thesis was limited to the suppression of tangential forces, which act at the torque level, but the non-sinusoidal distribution of the flux at the air-gap is responsible also for the production of high frequency radial forces, translating in audible noise. Therefore, studying the cause-effect transfer function, which relates the current harmonic components to the acceleration of the stator yoke for different frequencies, would enable the opportunity to attenuate these undesired effects in specific frequency ranges by mean of the developed algorithms.

Bibliography

[1] M. S. Sarma, *Electric Machines: Steady-State Theory and Dynamic Performance*. CL Engineering, 1997.

[2] R. J. Strahan, "Energy conversion by nonlinear permanent magnet machines," *IEE Proceedings - Electric Power Applications*, vol. 145, no. 3, pp. 193–198, May 1998.

[3] P. Pellerey, G. Favennec, V. Lanfranchi, and G. Friedrich, "Active reduction of electrical machines magnetic noise by the control of low frequency current harmonics," in *IECON 2012 - 38th Annual Conference on IEEE Industrial Electronics Society*, Oct 2012, pp. 1654–1659.

[4] J. Jose, G. N. Goyal, and M. V. Aware, "Improved inverter utilisation using third harmonic injection," in *2010 Joint International Conference on Power Electronics, Drives and Energy Systems 2010 Power India*, Dec 2010, pp. 1–6.

[5] R. Kalman, "On the general theory of control systems," *IRE Transactions on Automatic Control*, vol. 4, no. 3, pp. 110–110, Dec 1959.

[6] D. G. Luenberger, "Observing the state of a linear system," *IEEE Transactions on Military Electronics*, vol. 8, no. 2, pp. 74–80, April 1964.

[7] G. Welch and G. Bishop, "An introduction to the kalman filter." Tech. rep., ACM SIGGRAPH, Tech. Rep., 2001.

[8] L.-L. Xie and L. Guo, "How much uncertainty can be dealt with by feedback?" *IEEE Transactions on Automatic Control*, vol. 45, no. 12, pp. 2203–2217, Dec 2000.

[9] W. H. Chen, J. Yang, L. Guo, and S. Li, "Disturbance-observer-based control and related methods 2014;an overview," *IEEE Transactions on Industrial Electronics*, vol. 63, no. 2, pp. 1083–1095, Feb 2016.

[10] Y. Laatra, H. Lotfi, and B. Abdelhani, "Speed sensorless vector control of induction machine with luenberger observer and kalman filter," in *2017 4th International Conference on Control, Decision and Information Technologies (CoDIT)*, April 2017, pp. 0714–0720.

[11] A. Sellami and N. Zanzouri, "Fault diagnosis of a vehicular active suspension system by luenberger observer using bond graph approach," in *2017 International Conference on Green Energy Conversion Systems (GECS)*, March 2017, pp. 1–8.

[12] M. Messaoudi and L. Sbita, "Sensorless direct torque and flux control of induction motor based on mras and luenberger observer," in *2017 International Conference on Green Energy Conversion Systems (GECS)*, March 2017, pp. 1–7.

[13] D. Wang, Y. Wang, Q. Li, X. Chen, F. Gao, M. Tian, X. Mu, and T. Zang, "Low frequency voltage fluctuations in electrical vehicle-grid system based on luenberger-observer's multivariable control," in *2017 IEEE Conference on Energy Internet and Energy System Integration (EI2)*, Nov 2017, pp. 1–6.

[14] J. Yin, R. Tiwari, and M. Johnston, "Robust gps carrier tracking model using unscented kalman filter for a dynamic vehicular communication channel," *IEEE Access*, pp. 1–1, 2018.

[15] C. Huang, Z. Wang, Z. Zhao, L. Wang, C. S. Lai, and D. Wang, "Robustness evaluation of extended and unscented kalman filter for battery state of charge estimation," *IEEE Access*, pp. 1–1, 2018.

[16] E. M. Solodkiy, D. A. Dadenkov, and A. M. Kostygov, "Sensorless vector control of asynchronous machine based on reduced order kalman filter," in *2018 17th International Ural Conference on AC Electric Drives (ACED)*, March 2018, pp. 1–5.

[17] M. Schimmack, P. Mercorelli, and M. Maiwald, "Combining kalman filter and rls-algorithm to improve a textile based sensor system in the presence of linear time-varying parameters," in *2015 17th International Conference on E-health Networking, Application Services (HealthCom)*, Oct 2015, pp. 507–510.

[18] A. A. Mane, M. N. Parihar, S. P. Jadhav, and B. B. Digey, "Robotics based simultaneous localization and mapping of an unknown environment using kalman filtering," in *2015 5th Nirma University International Conference on Engineering (NUiCONE)*, Nov 2015, pp. 1–6.

[19] C. Mengnan, Q. Yingning, F. Yanhui, W. Hao, and D. Infield, "Wind turbine fault diagnosis based on unscented kalman filter," in *International Conference on Renewable Power Generation (RPG 2015)*, Oct 2015, pp. 1–5.

[20] J. O. Orozco-Lopez, C. E. Castaneda, A. RodrÃguez-Herrero, G. Garcia-Saez, and E. Hernando, "Linear time-varying luenberger observer applied to diabetes," *IEEE Access*, vol. 6, pp. 23 612–23 625, 2018.

[21] Y. Kim, K. S. Kim, and S. Kim, "A novel disturbance observer based robust current-control for a pmsm drive system," in *2015 54th IEEE Conference on Decision and Control (CDC)*, Dec 2015, pp. 6043–6046.

[22] H. Chen, J. Qu, B. Liu, and H. Xu, "A robust predictive current control for pmsm based on extended state observer," in *2015 IEEE International Conference on Cyber Technology in Automation, Control, and Intelligent Systems (CYBER)*, June 2015, pp. 1698–1703.

[23] S. Kwon and W. K. Chung, "A discrete-time design and analysis of perturbation observer for motion control applications," *IEEE Transactions on Control Systems Technology*, vol. 11, no. 3, pp. 399–407, May 2003.

[24] W.-H. Chen, D. J. Ballance, P. J. Gawthrop, and J. O'Reilly, "A nonlinear disturbance observer for robotic manipulators," *IEEE Transactions on Industrial Electronics*, vol. 47, no. 4, pp. 932–938, Aug 2000.

[25] Y. Huang, J. Wang, and D. Shi, "On convergence of extended state observers for discrete-time nonlinear systems," in *2015 34th Chinese Control Conference (CCC)*, July 2015, pp. 551–556.

[26] J. J. Vasquez-Sanjuan, J. L. Flores, E. Y. Mendoza, F. H. R. Leyva, and L. I. O. Perez, "Comparison between the algebraic and the reduced-order extended state observer approaches for on-line load torque estimation in a speed control for pmsm system," in *2016 13th International Conference on Power Electronics (CIEP)*, June 2016, pp. 18–22.

[27] G. Xingye, L. Chuang, Z. Yuefei, and W. Kai, "Analysis and dynamic decoupling control schemes for pmsm current loop," in *2016 IEEE International Conference on Aircraft Utility Systems (AUS)*, Oct 2016, pp. 570–574.

[28] S. Huang, L. Kong, T. Wei, and G. Zhang, "Comparative analysis of pi decoupling control strategies with or without feed-forward in srf for three-phase power supply," in *2008 International Conference on Electrical Machines and Systems*, Oct 2008, pp. 2372–2377.

[29] Y. I. Son, I. H. Kim, D. S. Choi, and H. Shim, "Robust cascade control of electric motor drives using dual reduced-order pi observer," *IEEE Transactions on Industrial Electronics*, vol. 62, no. 6, pp. 3672–3682, June 2015.

[30] A. Radke and Z. Gao, "A survey of state and disturbance observers for practitioners," in *2006 American Control Conference*, June 2006, pp. 6 pp.–.

[31] J. Han, "From pid to active disturbance rejection control," *IEEE Transactions on Industrial Electronics*, vol. 56, no. 3, pp. 900–906, March 2009.

[32] Z. Gao, S. Hu, and F. Jiang, "A novel motion control design approach based on active disturbance rejection," in *Decision and Control, 2001. Proceedings of the 40th IEEE Conference on*, vol. 5, 2001, pp. 4877–4882 vol.5.

[33] H. Liu and S. Li, "Speed control for pmsm servo system using predictive functional control and extended state observer," *IEEE Transactions on Industrial Electronics*, vol. 59, no. 2, pp. 1171–1183, Feb 2012.

[34] S. Li and Z. Liu, "Adaptive speed control for permanent-magnet synchronous motor system with variations of load inertia," *IEEE Transactions on Industrial Electronics*, vol. 56, no. 8, pp. 3050–3059, Aug 2009.

[35] R. Errouissi, A. Al-Durra, and S. M. Muyeen, "Experimental validation of a novel pi speed controller for ac motor drives with improved transient performances," *IEEE Transactions on Control Systems Technology*, vol. PP, no. 99, pp. 1–8, 2017.

[36] Y. A. R. I. Mohamed and E. F. El-Saadany, "Robust high bandwidth discrete-time predictive current control with predictive internal model x2014;a unified approach for voltage-source pwm converters," *IEEE Transactions on Power Electronics*, vol. 23, no. 1, pp. 126–136, Jan 2008.

[37] M. Yang, X. Lang, J. Long, and D. Xu, "Flux immunity robust predictive current control with incremental model and extended state observer for pmsm drive," *IEEE Transactions on Power Electronics*, vol. 32, no. 12, pp. 9267–9279, Dec 2017.

[38] J. Yang, W. H. Chen, S. Li, L. Guo, and Y. Yan, "Disturbance/uncertainty estimation and attenuation techniques in pmsm drives ;a survey," *IEEE Transactions on Industrial Electronics*, vol. 64, no. 4, pp. 3273–3285, April 2017.

[39] A. A. Prasov and H. K. Khalil, "A nonlinear high-gain observer for systems with measurement noise in a feedback control framework," *IEEE Transactions on Automatic Control*, vol. 58, no. 3, pp. 569–580, March 2013.

[40] B. Wojciechowski, "Analysis and synthesis of proportional-integral observers for single-input single-output time-invariant continuos systems." Ph.D. dissertation, Gliwice, Poland, 1978.

[41] B. Shafai and R. Carroll., "Design of proportional-integral observer for linear time-varying multivariable systems." *Proceedings of the 24th IEEE Conference on Decision and Control.*, 1985.

[42] T. Kaczorek, *Proportional-Integral Observers for Linear Multivariable Time Varying Systems.* Regelungstechnik 27., 1979, ch. 27, pp. 359–362.

[43] Y. Liu and D. Soeffker, "Improvement of optimal high-gain pi-observer design," in *2009 European Control Conference (ECC)*, Aug 2009, pp. 4564–4569.

[44] P. Muller, "Control of nonlinear systems by applying disturbance rejection control techniques." in *International Conference on Control 88. Institution of Electrical Engineers,*, 1988.

[45] D. Soffker and P. Muller., Eds., *Control of Dynamic Systems with Nonlinearities and Time Varying Parameters.*, 1993.

[46] S. D., J. Bajkowski, and P. Muller., "Detection of cracks in turbo rotors - a new observer based method." *ASME Journal of Dynamic Systems, Measurement, and Control 3*, 1993.

[47] S. Kirchenkamp, "Pi-observer techniques applied to mechanical systems," Ph.D. dissertation, University of Duisburg-Essen: Shaker Verlag, Aachen„ 2010.

[48] A. M. Alvarez and R. R. Leitch, "Active attenuation of acoustic noise using adaptive algorithms," in *1988., IEEE International Symposium on Circuits and Systems*, June 1988, pp. 511–514 vol.1.

[49] D. R. Morgan and D. A. Quinlan, "Local silencing of room acoustic noise using broadband active noise control," in *Proceedings of IEEE Workshop on Applications of Signal Processing to Audio and Acoustics*, Oct 1993, pp. 23–25.

[50] M. M. Dewasthale and R. D. Kharadkar, "Acoustic noise cancellation using adaptive filters: A survey," in *2014 International Conference on Electronic Systems, Signal Processing and Computing Technologies*, Jan 2014, pp. 12–16.

[51] M. Bari and M. M. Dewasthale, "Performance comparison of lms algorithms for acoustic noise cancellation," in *2016 Conference on Advances in Signal Processing (CASP)*, June 2016, pp. 139–143.

[52] J. D. L. Ree and N. Boules, "Torque production in permanent-magnet synchronous motors," *IEEE Transactions on Industry Applications*, vol. 25, no. 1, pp. 107–112, Jan 1989.

[53] N. Boules, "Prediction of no-load flux density distribution in permanent magnet machines," *IEEE Transactions on Industry Applications*, vol. IA-21, no. 3, pp. 633–643, May 1985.

[54] J. Holtz and L. Springob, "Identification and compensation of torque ripple in high-precision permanent magnet motor drives," *IEEE Transactions on Industrial Electronics*, vol. 43, no. 2, pp. 309–320, Apr 1996.

[55] N. Nakao and K. Akatsu, "Suppressing pulsating torques: Torque ripple control for synchronous motors," *IEEE Industry Applications Magazine*, vol. 20, no. 6, pp. 33–44, Nov 2014.

[56] H. F. Olson and E. G. May, "Electronic sound absorber," vol. Vol. 25, No. 6, pp. 1130-1136, Nov. 1953.

[57] S. Maier, J. Bals, and M. Bodson, "Periodic disturbance rejection of a pmsm with adaptive control algorithms," in *2011 IEEE International Electric Machines Drives Conference (IEMDC)*, May 2011, pp. 1070–1075.

[58] C. Xia, B. Ji, and Y. Yan, "Smooth speed control for low-speed high-torque permanent-magnet synchronous motor using proportional 2013;integral 2013;resonant controller," *IEEE Transactions on Industrial Electronics*, vol. 62, no. 4, pp. 2123–2134, April 2015.

[59] C. Lai, G. Feng, K. Mukherjee, V. Loukanov, and N. C. Kar, "Torque ripple minimization for interior pmsm with consideration of magnetic saturation incorporating online parameter identification," *IEEE Transactions on Magnetics*, vol. 53, no. 6, pp. 1–4, June 2017.

[60] J. Liu, H. Li, and Y. Deng, "Torque ripple minimization of pmsm based on robust ilc via adaptive sliding mode control," *IEEE Transactions on Power Electronics*, vol. PP, no. 99, pp. 1–1, 2017.

[61] L. Springob and J. Holtz, "High-bandwidth current control for torque-ripple compensation in pm synchronous machines," *IEEE Transactions on Industrial Electronics*, vol. 45, no. 5, pp. 713–721, Oct 1998.

[62] A. A. de Oliveira, J. R. B. de A. Monteiro, M. L. Aguiar, and D. P. Gonzaga, "Extended dq transformation for vectorial control applications of non-sinusoidal permanent magnet ac machines," in *2005 IEEE 36th Power Electronics Specialists Conference*, June 2005, pp. 1807–1812.

[63] P. Kshirsagar and R. Krishnan, "High-efficiency current excitation strategy for variable-speed nonsinusoidal back-emf pmsm machines," *IEEE Transactions on Industry Applications*, vol. 48, no. 6, pp. 1875–1889, Nov 2012.

[64] M. Bodson, J. S. Jensen, and S. C. Douglas, "Active noise control for periodic disturbances," *IEEE Transactions on Control Systems Technology*, vol. 9, no. 1, pp. 200–205, Jan 2001.

[65] G. Heins, M. Thiele, and T. Brown, "Accurate torque ripple measurement for pmsm," *IEEE Transactions on Instrumentation and Measurement*, vol. 60, no. 12, pp. 3868–3874, Dec 2011.

[66] W. Qian, S. K. Panda, and J. X. Xu, "Speed ripple minimization in pm synchronous motor using iterative learning control," *IEEE Transactions on Energy Conversion*, vol. 20, no. 1, pp. 53–61, March 2005.

[67] G. Feng, C. Lai, and N. C. Kar, "A closed-loop fuzzy-logic-based current controller for pmsm torque ripple minimization using the magnitude of speed harmonic as the feedback control signal," *IEEE Transactions on Industrial Electronics*, vol. 64, no. 4, pp. 2642–2653, April 2017.

[68] M. N. Uddin and M. M. Rahman, "Online torque-flux estimation based nonlinear torque and flux control scheme of ipmsm drive for reduced torque ripples," *IEEE Transactions on Power Electronics*, pp. 1–1, 2018.

[69] N. Nakao and K. Akatsu, "Torque ripple control for synchronous motors using instantaneous torque estimation," in *2011 IEEE Energy Conversion Congress and Exposition*, Sept 2011, pp. 2452–2459.

[70] K. C. Yeo, G. Heins, and F. D. Boer, "Comparison of torque estimators for pmsm," in *2008 Australasian Universities Power Engineering Conference*, Dec 2008, pp. 1–6.

[71] K. R. Muske, J. B. Rawlings, and J. H. Lee, "Receding horizon recursive state estimation," in *1993 American Control Conference*, June 1993, pp. 900–904.

[72] I. Tabatabaei Ardekani and W. Abdulla, "Fxlms-based active noise control: A quick review," 01 2011.

[73] B. Widrow, J. R. Glover, J. M. McCool, J. Kaunitz, C. S. Williams, R. H. Hearn, J. R. Zeidler, J. E. Dong, and R. C. Goodlin, "Adaptive noise cancelling: Principles and applications," *Proceedings of the IEEE*, vol. 63, no. 12, pp. 1692–1716, Dec 1975.

[74] E. W. Ziegler, "Selective active cancellation system for repetitive phenomena„" U.S. Patent Patent No. 4,878,188, Oct. 1989.

[75] S. Sastry and M. Bodson, *Adaptive Control - Stability, Convergence and Robustness*. Prentice Hall, 1989.

[76] J. Chandrasekar, L. Liu, D. Patt, P. P. Friedmann, and D. S. Bernstein, "Adaptive harmonic steady-state control for disturbance rejection," *IEEE Transactions on Control Systems Technology*, vol. 14, no. 6, pp. 993–1007, Nov 2006.

[77] S. Pigg and M. Bodson, "Adaptive rejection of sinusoidal disturbances of known frequency acting on unknown systems," in *2006 American Control Conference*, June 2006, pp. 5 pp.–.

[78] X. Guo and M. Bodson, "Adaptive rejection of multiple sinusoids of unknown frequency," in *2007 European Control Conference (ECC)*, July 2007, pp. 121–128.

[79] B. Wu and M. Bodson, "Multi-channel active noise control for periodic disturbances," in *Proceedings of the 38th IEEE Conference on Decision and Control (Cat. No.99CH36304)*, vol. 5, 1999, pp. 4971–4975 vol.5.

[80] ——, "Direct adaptive cancellation of periodic disturbances for multivariable plants," *IEEE Transactions on Speech and Audio Processing*, vol. 11, no. 6, pp. 538–548, Nov 2003.

List of Symbols

Sets, Matrices, Vectors

$\mathbb{R}(\mathbb{R}_+)$	Set of real numbers (non-negative real numbers)
$\mathbb{N}(\mathbb{N}_+)$	Set of integers (non-negative integers)
$\mathbb{R}^n$	Set of real vectors with n elements
$\mathbb{R}^{n\times m}$	Set of real matrices with n rows and m columns
$[\mathrm{T}]_{\alpha\beta}$	Forward Clarke transformation
$[\mathrm{T}]_{dq}$	Forward Park transformation
$\mathbf{I}$	Identity matrix of appropriate dimension
$\mathbf{J}$	Rotation matrix $\mathbf{J} = [[0,-1],[1,0]]^\top$
$\mathbf{0}$	Zero matrix of appropriate dimension

Algebraic Operators

A	Matrix A
$\mathrm{A}^\top$	Transpose of matrix A
A^{-1}	Inverse of matrix A
A_i	i-th row and i-th column of matrix A
$\underline{x}$	Vector $\underline{x}$ of dimension $n \times 1$
$\underline{x}^\top$	Transpose of Vector $\underline{x}$
$\underline{x}_i$	i-th element of vector $\underline{x}$
$\|\underline{x}\|$	Euclidean norm of vector $\underline{x}$; $\|\underline{x}\| = \sqrt{\underline{x}^\top \underline{x}}$
$\|\underline{x}\|^2$	Squared euclidean norm of vector $\underline{x}$; $\|\underline{x}\|^2 = \underline{x}^\top \underline{x}$
$\|\underline{x}\|_R^2$	Squared weighted euclidean norm of vector $\underline{x}$; $\|\underline{x}\|_R^2 = \underline{x}^\top \mathrm{R} \underline{x}$

Acronyms

ANC	Active Noise Cancellation
BEMF	Back Electromagnetic Force
BJT	Bipolar Junction Transistor
DOB	Disturbance Observer Based
EM	Electric Machine
EV	Electrical Vehicle
FE	Finite Element
FF	Feedforward
FOC	Field Oriented Control
HPF	High Pass Filter
KF	Kalman Filter
IGBT	Insulated Gate Bipolar Transistor
IPMSM	Interior Permanent Magnet Synchronous Machine
LMS	Least Mean Square
LO	Luenberger Observer
LQO	Linear Quadratic Observer
LTI	Linear Time Invariant
LTV	Linear Time Variant
MIMO	Multi-Input Multi-Output
MMF	Magnetomotive Force
MOSFET	Metal Oxide Semiconductor Field Effect Transistor
MTPA	Maximum Torque Per Ampere
PHEV	Plug-in-Hybrid Electrical Vehicle
PIO	Proportional-Integral Observer
PMSM	Permanent Magnet Synchronous Machine
PWM	Pulse Width Modulation
QP	Quadratic Problem
SISO	Single-Input Single-Output
SPMSM	Surface Permanent Magnet Synchronous Machine
SPWM	Sinusoidal Pulse Width Modulation
SVPWM	Space Vector Pulse Width Modulation